

OPTIMISATION OF OCTAHEDRAL METAL COMPLEXES
THROUGH SPIN-CROSSOVER MODULATION FOR
HARVESTING THERMOELECTROCHEMICAL ENERGY

MEGAT MUHAMMAD IKHSAN BIN MEGAT HASNAN

FACULTY OF ENGINEERING
UNIVERSITY OF MALAYA
KUALA LUMPUR

2019

**OPTIMISATION OF OCTAHEDRAL METAL
COMPLEXES THROUGH SPIN-CROSSOVER
MODULATION FOR HARVESTING
THERMOELECTROCHEMICAL ENERGY**

MEGAT MUHAMMAD IKHSAN BIN MEGAT HASNAN

**THESIS SUBMITTED IN FULFILMENT OF THE
REQUIREMENTS FOR THE DEGREE OF DOCTOR OF
PHILOSOPHY**

**FACULTY OF ENGINEERING
UNIVERSITY OF MALAYA
KUALA LUMPUR**

2019

UNIVERSITY OF MALAYA
ORIGINAL LITERARY WORK DECLARATION

Name of Candidate: Megat Muhammad Ikhsan Bin Megat Hasnan

Matric No: KHA150083

Name of Degree: Degree of Doctor of Philosophy

Title of Dissertation: OPTIMISATION OF OCTAHEDRAL METAL COMPLEXES
THROUGH SPIN-CROSSOVER MODULATION FOR
HARVESTING THERMOELECTROCHEMICAL ENERGY

Field of Study: RENEWABLE ENERGY

I do solemnly and sincerely declare that:

- (1) I am the sole author/writer of this Work;
- (2) This Work is original;
- (3) Any use of any work in which copyright exists was done by way of fair dealing and for permitted purposes and any excerpt or extract from, or reference to or reproduction of any copyright work has been disclosed expressly and sufficiently and the title of the Work and its authorship have been acknowledged in this Work;
- (4) I do not have any actual knowledge nor do I ought reasonably to know that the making of this work constitutes an infringement of any copyright work;
- (5) I hereby assign all and every rights in the copyright to this Work to the University of Malaya ("UM"), who henceforth shall be owner of the copyright in this Work and that any reproduction or use in any form or by any means whatsoever is prohibited without the written consent of UM having been first had and obtained;
- (6) I am fully aware that if in the course of making this Work I have infringed any copyright whether intentionally or otherwise, I may be subject to legal action or any other action as may be determined by UM.

Candidate's Signature

Date:

Subscribed and solemnly declared before,

Witness's Signature

Date:

Name:

Designation:

ABSTRACT

Thermo-electrochemical cell (TEC) technology allows the conversion of a thermal gradient into electricity due to the Seebeck effect using inert electrodes and active redox electrolyte. TEC require a high entropy difference for high power density. This study proposes the use of a family of spin crossover (SCO) metal complexes as the TEC material. The change of spin states from high spin (HS) to low spin (LS) or vice versa, is utilized as the key mechanism in enhancing the entropy difference, and hence Seebeck coefficient of the system. The scope of this study is divided into three: (1) molecular modeling of the SCO complexes, (2) SCO composite optimisation and (3) proposing micro-TEC device design and fabrication process for future work. The SCO materials used in this work are based on an octahedral structure of transition metals (Iron, Cobalt and Manganese). Density Functional Theory (DFT) is used to correlate between molecular conformation and electrochemical HOMO-LUMO gap that provides a fundamental understanding of the SCO molecule as a function of its spin states. The SCO complexes synthesised is analysed using electrochemical impedance spectroscopy and cyclic voltammetry to provide a comprehensive picture of the thermoelectric performance of these SCO composite. The lower electrochemical HOMO-LUMO gap energy of a high in stable LS Fe in MPN obtained from molecular modeling and CV analysis explained the basis high ionic conductivity of Fe in MPN by three orders magnitude higher compared to Fe, Mn and Co in DMSO. Interestingly, the agglomeration of the Fe complex in MPN, in the form of spherical micelles (diameter ~200 nm,) provided an explanation its high Seebeck coefficient, as the high entropy of such an agglomeration resulted in a high Seebeck coefficient. The optimised micelle stability of Fe complex through 1% wt of PMMA additive to form gel TEC material shows power output of one order of magnitude higher ($60\mu\text{Wm}^{-2}$ at $\Delta T=60^\circ\text{C}$) than power output of the conventional KI-KI₃ redox couple and complexes in solution ($3-5\mu\text{Wm}^{-2}$). As a final study, module of

TEC generators was fabricated using MEMS technology to provide a realistic platform for waste heat energy harvesting. Then, this work provide a systematic study of optimization of SCO metal complexes for energy harvesting from fundamental molecular design to SCO material synthesis and analysis to device fabrication. The gel Fe complex was the best SCO material compared to Mn and Co due to high SCO molecular stability and stable micelles formation capability thus enhance TEC performance through enhancement of both Seebeck coefficient and conductivity simultaneously.

Keywords: Thermoelectrochemical cells, Seebeck, spin crossover, redox, MEMS

University of Malaysia

ABSTRAK

Teknologi termoelektrik (TE) membolehkan penukaran kecerunan haba kepada tenaga elektrik disebabkan oleh kesan Seebeck menggunakan elektrod lengai dan bahan aktif redoks. TEC memerlukan pekali Seebeck yang tinggi, kealiran ion-ion yang tinggi dan kealiran haba yang rendah. Dalam penyelidikan ini, penggunaan keluarga kompleks-kompleks logam dengan kelakuan pindahan spin (SCO) sebagai bahan termoelektrokimia (TEC) telah dicadangkan. Perubahan keadaan spin daripada spin tinggi kepada spin rendah atau sebaliknya, adalah digunakan sebagai kunci mekanisma dalam merangsangkan perbezaan entropi dan seterusnya pekali Seebeck dalam system. Skop dalam penyelidikan ini terbahagi kepada tiga bahagian: (1) model molekul dalam kompleks-kompleks SCO, (2) optimumkan SCO komposit dan (3) cadangan rekaan dan kaedah penghasilan peranti mikro-TEC bagi kerja masa hadapan. Bahan-bahan SCO digunakan dalam kerja ini berdasarkan struktur oktahedron dalam logam peralihan (Ferum, Kobalt, Mangan). Teori Fungsi Ketumpatan (DFT) adalah digunakan untuk reka bentuk dan model ciri-ciri elektronik untuk kompleks-kompleks ini. Menggunakan peralatan Simulasi Material Studio Biovia, hubungan kait antara pengesahan molekul dan jurang elektrokimia HOMO-LUMO untuk menyediakan pemahaman asas dalam molekul SCO sebagai fungsi keadaan spin. Kompleks-kompleks SCO yang telah dihasilkan telah dianalisis secara mendalam menggunakan spektroskopi impedans elektrokimia (EIS) dan voltametri siklik bagi menyediakan satu gambaran yang menyeluruh dalam prestasi larutan-larutan komposit SCO ini. Jangkaan peralihan keadaan spin dalam kompleks ini daripada permodelan molekul menunjukkan persetujuan yang baik dengan analisis bereksperimen di mana kompleks Fe menunjukkan keadaan spin rendah yang lebih stabil berbanding spin tinggi herotan yang tak stabil untuk kompleks-kompleks Mn and Co, yang dihasilkan daripada analisis kelonggaran dielektrik menggunakan EIS. Tenaga jurang jalur elektrokimia yang rendah berkeadaan kestabilan yang tinggi dalam spin

rendah Fe dalam larutan n-methoxypropionitrile (MPN) yang didapati daripada permodelan molekul dan analisis voltametri siklik yang menerangkan asas kealiran ion-ion yang tinggi untuk Fe dalam larutan MPN dengan tiga susunan magnitud yang lebih tinggi berbanding dengan Fe, Mn, dan Co dalam larutan dimethyl sulfoxide (DMSO). Menariknya, pergumpalan kompleks Fe dalam larutan MPN, dalam bentuk misel bersfera (diameter ~ 200 nm), menyediakan satu penjelasan pekali Seebeck yang tinggi, kerana entropi yang tinggi seperti aglomerasi menghasilkan pekali Seebeck yang tinggi. Kestabilan optimum pembentukan misel Fe telah di tambah baik dengan pembangunan satu bahan gel TEC menggunakan 1% berat poly(methyl methacrylate) (PMMA) sebagai agen penggelan dalam larutan MPN menunjukkan hasil kuasa yang mana satu susunan magnitud yang lebih tinggi berbanding dalam bentuk larutan ($60 \mu\text{Wm}^{-2}$ at $\Delta T=60^\circ\text{C}$) telah ditingkatkan oleh satu susunan magnitud berbanding hasil kuasa dalam pasangan redoks KI-KI₃ yang konvensional dan kompleks-kompleks dalam larutan ($3-5 \mu\text{Wm}^{-2}$). Sebagai penyelidikan terakhir, modul penjana TEC telah direka menggunakan teknologi MEMS to menyediakan satu platform yang realistik untuk penuaian tenaga haba yang terbuang. Seterusnya, kerja ini menyediakan satu penyelidikan yang sistematik dalam menambah baik kompleks-kompleks logam untuk penuaian tenaga daripada rekabentuk asas molekul kepada penyediaan bahan SCO dan analisis pembuatan alat. Gel kompleks Fe adalah bahan SCO terbaik berbanding Mn and Co kerana kestabilan SCO yang tinggi dan keupayaan untuk membentuk misel yang stabil maka meningkatkan performan TEC melalui peningkatan kedua-dua Seebeck dan konduktiviti.

Keywords: Sel termoelektrokimia, Seebeck, kelakuan pindahan spin, redoks, MEMS

ACKNOWLEDGEMENTS

All praise is only for Allah SWT, who has bestowed me a precious and wonderful life in this world.

My sincere thanks go to my supervisors, Assoc. Prof. Ir. Dr. Suhana Mohd Said, for her guidance, inspiration, patience, and invaluable assistance during all the time of research. Thanks are also to my co-supervisors Dr. Mohd Faiz Bin Mohd Salleh and Dr. Noraisyah Mohd Shah. The provision by Assoc. Prof. Ir. Dr. Faizul Mohd Sabri of laboratory facilities in Nano Lab. Special thanks to Assoc. Prof. Dr. Norbani Abdullah and Siti Amira Mat Hussin from Department of Chemistry, Faculty of Science for collaboration and assistance in complex synthesis process and methodology.

I wish thanks to my mother Norehan binti Alang Abdul Shuker, my father Megat Hasnan bin Megat Din, my lovely wife Jastina Binti Mohd Aminorashid and all lab members for their support and encouragement over the years. I would also like to highlight my lovely newborn son, Megat Nur Idzaanuddin who's made me stronger to complete my challenging PhD journey. Also special thanks to Dr Ikhwan Syafiq from UPM with his support on electrochemical impedance fundamental and analysis. Also, thanks to Mr Khairul Azly bin Rosli, Head of Engineer of Hospital Serdang for his help on Lab View self-custom data analyser build. Thanks also to all LCD and Nanolab family members.

Special thanks to Tohoku University and also to the all nano-micro engineering lab Ono-Inomata/Toda research team especially Professor Dr. Takahito Ono as main supervisor and Dr. Nguyen Van Toan as second supervisor during 4 month as special research student in Japan. Thanks to JASSO for the scholarship fund support along the 4 month process learning. All of the valuable experience gained will be further plan for the future collaboration between Tohoku University and University of Malaya.

TABLE OF CONTENTS

Abstract	iii
Abstrak	v
Acknowledgements	vii
Table of Contents	viii
List of Figures	xv
List of Tables	xxii
List of Abbreviations	xxiii
List of Symbols	xxv
List of Appendices	xxviii
CHAPTER 1: INTRODUCTION	1
1.1 Energy consumptions in Malaysia	1
1.2 Thermoelectric (TE) as sustainable renewable energy in Malaysia	2
1.3 General Problem Statement	3
1.4 Research Objectives	4
1.5 Overview	5
CHAPTER 2: LITERATURE REVIEW	6
2.1 Introduction to the thermo-electrochemical cells (TEC)	6
2.2 TEC working principles	8
2.2.1 Theory of TEC entropy reaction	8
2.2.1.1 Soret effect	10
2.2.2 Theory of TEC heat transfer in relation with entropy reaction	11
2.2.3 TEC output power	12
2.2.4 A modified figure of merit ZT for TEC	12

2.3	TEC capability	14
2.4	Recent Development of TEC	14
2.4.1	Redox couples	14
2.4.2	Electrolyte properties	16
2.4.2.1	Ionic liquid and molecular solvent	17
2.4.2.2	Electrolyte Additive	18
2.4.2.3	Quasi-solid-state electrolytes	18
2.4.3	Electrode materials	19
2.4.4	Cell design and optimization	20
2.4.4.1	Cell modeling	20
2.4.4.2	Cell orientation and electrode spacing	21
2.4.4.3	Separators and membrane	21
2.4.4.4	Series stacking of cell	22
2.5	Theory of Cyclic Voltammetry of TEC	23
2.5.1	Theoretical derivation of Seebeck coefficient using CV	25
2.6	Theoretical of Electrochemical Impedance Spectroscopy (EIS) of TEC	29
2.6.1	Electrical Circuit Elements	30
2.7	Potential of spin cross over material for TEC application	33
2.7.1	Jahn-Teller theorem	36
2.8	Practical Requirement of TEC for renewable energy	37

CHAPTER 3: THERMO-ELECTROCHEMICAL GENERATION OF PURE MN, FE AND CO WITH N-DONOR LIGANDS CARBON CHAIN 14 AND BENZOATE AS COUNTER ION WITHOUT KI-KI₃

3.1	Introduction	39
3.2	Methodology	40
3.2.1	Octahedral SCO ion complex design	40

3.2.2	Molecular modeling	42
3.2.2.1	Geometry Optimization.....	44
3.2.2.2	Dynamic NVT geometry optimizations	45
3.2.2.3	DMoL ³ density of states calculation	45
3.2.2.4	Electrochemical HUMO-LUMO Gap Energy Calculation at Room Temperature and dependent temperature (100-400 K) ..	46
3.2.2.5	DMoL ³ Time-dependent Density Functional Theory (TD-DFT) Optic Spectrum Analysis.....	46
3.2.3	Synthesis of SCO material	47
3.2.3.1	Synthesis of [Mn(cyclam)(L14) ₂](C ₆ H ₅ COO) ₂ .4H ₂ O.....	47
3.2.3.2	Synthesis of [Fe(cyclam)(L14) ₂](C ₆ H ₅ COO) ₂ .2H ₂ O	48
3.2.4	Synthesis of [Co(cyclam)(L14) ₂](C ₆ H ₅ COO) ₂ .3H ₂ O.....	48
3.2.5	Structural Analysis	50
3.2.6	Cyclic voltammetry analysis	50
3.2.7	Electrical conductivity measurement	52
3.2.8	Seebeck and power measurement of non-isothermal cell	53
3.3	Results and discussion	54
3.3.1	Molecular modeling	54
3.3.1.1	Geometry optimisation.....	54
3.3.1.2	Density of states (DOS) calculation	56
3.3.1.3	Electrochemical HUMO-LUMO gap energy.....	59
3.3.1.4	Optic Spectrum Analysis using DMOL ³	61
3.3.2	Structural analysis	64
3.3.3	Cyclic Voltammetry analysis	66
3.3.3.1	Diffusion ratio	68
3.3.3.2	Total Electrode Formal Potential	69

3.3.4	Ionic conductivity	71
3.3.5	Seebeck coefficient.....	72
3.3.6	Power density	73
3.4	Conclusions	74

**CHAPTER 4: ENHANCEMENT OF SEEBECK AND IONIC CONDUCTIVITY
SIMULTANEOUSLY OF KI-KI₃ REDOX ELECTROLYTE USING SCO
COMPLEXES MICELLES FORMATION**

4.1	Introduction.....	76
4.2	Methodology.....	78
4.2.1	Sample synthesis	78
4.2.2	Electrochemical Impedance Analysis	79
4.2.3	Cyclic Voltammetry	80
4.2.4	Ionic conductivity.....	80
4.2.5	Seebeck coefficient and power.....	80
4.3	Results and discussion	81
4.3.1	Agglomeration studies.....	81
4.3.1.1	OPM analysis	81
4.3.1.2	UV-vis analysis	82
4.3.1.3	Cryo-TEM analysis	83
4.3.2	EIS investigation of spin states	84
4.3.3	Cyclic voltammetry analysis	86
4.3.3.1	Redox reaction of Mn(II) solution under temperature gradient	87
4.3.3.2	Redox reaction of Co(II) solution under temperature gradient	88
4.3.3.3	Redox reaction of Fe(II) solution under temperature gradient	88
4.3.3.4	Diffusion coefficient analysis.....	90
4.3.4	Seebeck coefficient measurement of SCO complexes with KI-KI ₃	91

4.3.5	Ionic conductivity of SCO complexes with KI-KI ₃	92
4.3.6	Power output.....	94
4.4	Conclusions	94

CHAPTER 5: THERMO-ELECTROCHEMICAL GENERATION OF PURE MN, FE AND CO WITH N-DONOR LIGANDS CARBON CHAIN 16 AND BENZOATE AS COUNTER ION WITH KI-KI₃.....96

5.1	Introduction.....	96
5.2	Methodology.....	97
5.2.1	Ligand (L16) preparation(Hussin, 2016).....	97
5.2.2	SCO complexes preparation	97
5.2.3	Structural analyses.....	98
5.2.4	Thermal analysis.....	98
5.2.5	Magnetic analysis	99
5.2.6	UV-vis spectroscopy	99
5.2.7	Non-isothermal Seebeck measurement	100
5.3	Results and discussion	100
5.3.1	Ligand 16 characterisation	100
5.3.2	Fe, Mn and Co complexes preparation.....	101
5.3.3	Thermal properties	103
5.3.4	Magnetic properties	104
5.3.5	UV-vis properties	106
5.3.5.1	Molar absorption	107
5.3.6	Seebeck coefficient.....	108
5.4	Conclusion	110

**CHAPTER 6: ENHANCEMENT OF TEC PERFORMANCE USING SCO
LIGAND 14 WITH KI-KI₃ AND PMMA GEL ELECTROLYTE..... 111**

6.1	Introduction.....	111
6.2	Methodology.....	111
6.2.1	Gel electrolyte preparation	111
6.2.2	Electrochemical analysis	112
6.2.3	Power output density	112
6.3	Results and discussion	112
6.3.1	CV analysis of gel KI-KI ₃ and gel FeL14 complex with KI-KI ₃ at room temperature	112
6.3.1.1	Diffusion coefficient and electrochemical HOMO-LUMO gap	
	113	
6.3.2	Power output density	114
6.4	Conclusion	115

**CHAPTER 7: FABRICATION OF MICRO-TEC DEVICES FOR LOW GRADE
HEAT WASTE POWER GENERATION 116**

7.1	Introduction.....	116
7.2	Methodology.....	117
7.2.1	P-type and N-type TEC material preparation	117
7.2.2	Temperature dependent CV analysis.....	118
7.2.3	Single cell TEC device design and fabrication	118
7.2.4	TEC performance evaluation.....	127
7.2.5	P-N single junction TEC device design and fabrication	127
7.3	Results and discussion	128
7.3.1	Solution resistance.....	128
7.3.2	Cyclic voltammetry analysis	129

7.3.2.1 Numerical study for Seebeck sign prediction based on Cyclic voltammetry experimental analysis.....	129
7.3.3 TEC performance	131
7.4 Conclusion	133
7.5 Future work.....	134
CHAPTER 8: CONCLUSION.....	141
References	143
List of Publications	149
Appendix A: Lab View	151

University of Malaya

LIST OF FIGURES

Figure 1.1. Total energy consumption by sectors in Malaysia	1
Figure 1.2. Malaysia energy primary supply imports	2
Figure 2.1. TEC in steady state at no temperature gradient (Equilibrium State).....	7
Figure 2.2. TEC in steady at temperature gradient	7
Figure 2.3. TEC a) Non-isothermal b) Isothermal	8
Figure 2.4. Redox process in TEC at temperature gradient	9
Figure 2.5. Born's model of A as reduction and B as oxidation species	10
Figure 2.6. Sorret effect a) no temperature different b) at temperature different	10
Figure 2.7. Convection and diffusion in TEC(Quickenden & Mua, 1995b)	11
Figure 2.8. TEC power generation capability	14
Figure 2.9. Recent development of redox couple	16
Figure 2.10. Recent development of TEC electrolytes	16
Figure 2.11. Recent development of TEC electrode	19
Figure 2.12. Recent cell optimization development of TEC devices.....	20
Figure 2.13. TEC cell orientation natural convection investigation(Salazar, Kumar, et al., 2014)	21
Figure 2.14. Thermal distribution of inserted membrane TEC(Hasan et al., 2016)	22
Figure 2.15. Series stacking TEC a) same electrolyte b) p/n-type electrolyte c) Photograph of alternating n-type and p-type mediators for a thermocell array with 14 n-p cells d) Photograph of the sealed thermocell array for the redox couple array in (c), which shows the top plate that completes the electrical connections e) the voltage-time curves of different capacitors when charged by four series-connected thermocell arrays(Zhang et al., 2017).....	23
Figure 2.16. Cyclic Voltammogram of single redox reaction.....	24
Figure 2.17. Isothermal Cell of TEC having a)one working electrode b) two working electrode	26

Figure 2.18. TEC a)no temperature gradient and b) at temperature gradient	26
Figure 2.19. Example of TEC electrical equivalent circuit.....	30
Figure 2.20. Equivalent circuit of double layer formation.....	31
Figure 2.21. Nyquist plot of double layer impedance	31
Figure 2.22. Equivalent circuit for Faradaic reaction	32
Figure 2.23. Nyquist plot of Faradaic impedance using Gamry software	32
Figure 2.24. SCO effect of SCO material	35
Figure 2.25. Energy gap of HS/LS a)Fe b)Mn c)Co	35
Figure 2.26. Jahn-Teller distortion.....	37
Figure 3.1. SCO material design used for TEC material a) cyclam b) N-donor ligand c) and d) $M=[Mn]^{2+}$, $[Fe]^{2+}$, $[Co]^{2+}$ calculated molecular structure.....	14 41
Figure 3.2. d-orbital electronic configuration for HS/LS for Fe, Co and Mn	42
Figure 3.3. Simulation Steps	43
Figure 3.4. Metal to ligand interaction of octahedral structure.....	45
Figure 3.5. Schematic of metal complex synthesis process	49
Figure 3.6. Example of Mn complex synthesis steps.....	49
Figure 3.7.Redox potential determination using LAB VIEW	51
Figure 3.8. CV measurement setup	52
Figure 3.9. Conductivity measurement setup.....	53
Figure 3.10. Seebeck and power measurement setup	54
Figure 3.11. Molecular bond length of metal to ligand interaction induce high entropy different between spin state transition.....	55
Figure 3.12. Average of bond length between the metal center and the six nitrogen atom	56
Figure 3.13. Optimize geometry of Fe(II) complex at temperature dependent	56
Figure 3.14. Density state calculation of LS/HS state of SCO complexes	58

Figure 3.15. Energy different calculation of the complexes for spin state transition of a) Co^{2+} b) Fe^{2+} c) Mn^{2+} d) Co^{3+} e) Fe^{3+} and f) Mn^{3+}	59
Figure 3.16. Density of state of d-orbital for complexes $2+$	60
Figure 3.17. Electrochemical HOMO-LUMO gap calculation from DOS	60
Figure 3.18. HOMO-LUMO gap energy of complexes $2+$	61
Figure 3.19. Excitation energy calculation of ionic SCO complex ligand 14 at room temperature	62
Figure 3.20. Excitation energy trend of the complexes at dependent temperature a) $\text{Fe}(\text{DMSO})$ b) $\text{Mn}(\text{DMSO})$ c) $\text{Co}(\text{DMSO})$ and d) $\text{Fe}(\text{MPN})$	64
Figure 3.21. FTIR spectrum of a) Co b) Fe and c) Mn complexes	66
Figure 3.22. Cyclic voltammetry characteristic of TEC materials at room temperature for a) $\text{Fe}(\text{II})$ in DMSO b) $\text{Fe}(\text{II})$ in MPN c) $\text{Co}(\text{II})$ in DMSO and d) $\text{Mn}(\text{II})$ in DMSO	67
Figure 3.23. Diffusion ratio extraction from CV scan rate 5 mVs^{-1} as a function of temperature for $\text{Fe}(\text{II})$ in MPN $\text{Fe}(\text{II})$ in DMSO $\text{Mn}(\text{II})$ in DMSO and $\text{Co}(\text{II})$ in DMSO	69
Figure 3.24. Total electrode formal potential extraction from CV scan rate 5 mVs^{-1} as a function of temperature for $\text{Fe}(\text{II})$ in MPN $\text{Fe}(\text{II})$ in DMSO $\text{Mn}(\text{II})$ in DMSO and $\text{Co}(\text{II})$ in DMSO	71
Figure 3.25. Ionic conductivity of a) $\text{Fe}(\text{II})$ MPN b) $\text{Fe}(\text{II})$ DMSO c) $\text{Co}(\text{II})$ DMSO and d) $\text{Mn}(\text{II})$ DMSO	72
Figure 3.26. Seebeck coefficient of $\text{Fe}(\text{II})$ MPN , $\text{Fe}(\text{II})$ DMSO , $\text{Co}(\text{II})$ DMSO and $\text{Mn}(\text{II})$ DMSO	73
Figure 3.27. Power density of a) $\text{Fe}(\text{II})$ in DMSO and b) $\text{Fe}(\text{II})$ in MPN at different ΔT	74
Figure 4.1. Agglomeration formation effect to redox active material	78
Figure 4.2. Mixture of redox active material with SCO material preparation	79
Figure 4.3. Solution prepared a) $\text{Mn}(\text{II})$, b) $\text{Co}(\text{II})$, c) $\text{Fe}(\text{II})$	81
Figure 4.4. OPM analysis a) $\text{Fe}(\text{II})$ solution 10x magnification b) $\text{Fe}(\text{II})$ solution 50x magnification and c) $\text{Co}(\text{II})$ solution 50x magnification	82
Figure 4.5. Absorbance of Fe solution time dependent	83

Figure 4.6. Absorbance at 475 nm of Fe solution time dependent	83
Figure 4.7. Spherical Micelles and agglomeration formation observation using Cyro-TEM analysis	84
Figure 4.8. Plots of loss tangent peak versus frequency a)DMSO+KI-KI ₃) and MPN+KI-KI ₃ , b)III(Fe), c)II(Co) and d)I(Mn). The arrows indicate transition spin state of the complexes and the black dotted line indicates the frequency at the loss tangent peak...85	85
Figure 4.9. Plots of Cylic Voltammogram a) DMSO+KI-KI ₃ b) MPN+KI-KI ₃ c) Mn(II), d) Co(II) and e) Fe(II)	86
Figure 4.10. Plots of ΔV versus ΔT for solutions of Mn(II),green diamond;Fe(II), red square; and Co(II) blue circle.....	92
Figure 4.11. Plots of ionic conductivity versus temperature for samples (a)DMSO+KI-KI ₃ , blue circle; MPN+KI-KI ₃ , red square and (b) Mn(II), green diamond; Co(II), blue circle; and Fe(II), red square.	93
Figure 4.12. Plots of output power versus load voltage for samples Mn(II), green diamond; Co(II), blue circle; and Fe(II), red square	94
Figure 5.1. ¹ H-NMR spectrum of L16 at room temperature.....	100
Figure 5.2. FTIR analysis of L16 at room temperature.....	101
Figure 5.3. FTIR of SCO complexes L16 at room temperature	102
Figure 5.4. Thermogravimetry analysis (TGA) for the SCO complexes L16	103
Figure 5.5. DSC scans for a) heating b) cooling of the SCO complexes L16	104
Figure 5.6. ¹ H-NMR spectrum of Co, Fe and Mn complex with L16 at room temperature	105
Figure 5.7. Temperature dependent of SQUID magnetometer analysis for complexes L16	106
Figure 5.8. UV-Vis spectrum of complexes at room temperature	106
Figure 5.9. Temperature dependent molar absorption values of a) CoL16 b) FeL16 and c) MnL16 in solution.....	108
Figure 5.10. Seebeck measurement of a) FeL16 and FeL14 b) CoL16 and Co L14 and c) MnL16 and Mn L14	110
Figure 6.1. Gel redox electrolyte preparations using pure PMMA.....	112

Figure 6.2. CV analysis at room temperature for a) PMMA+KI-KI ₃ +MPN b) PMMA+Fe+KI-KI ₃ +MPN	113
Figure 6.3. TEC Output power of PMMA+KI-KI ₃ at different temperature difference	114
Figure 6.4. TEC Output power of PMMA+Fe+KI-KI ₃ at different temperature difference	115
Figure 7.1. Cyclic voltammetry analyses of isothermal cell setup at dependent temperature.....	118
Figure 7.2. Single cell TEC device design using conventional planar electrode.....	119
Figure 7.3. TEC device fabrication process flow.....	120
Figure 7.4. Si wafer dicing machine	121
Figure 7.5. Si wafer cleaning process	121
Figure 7.6. Photolithography process flow	122
Figure 7.7. Deep RIE dummy wafer bonding process flow.....	123
Figure 7.8. SPT-SRE Deep Reactive ion etching machine.....	123
Figure 7.9. Schematic of upper electrode a) positive resist develop mask design b) Deep RIE on process c) Si wafer after deep reactive ion etching	124
Figure 7.10. Post residue remover process flow after Deep RIE process	124
Figure 7.11. a) SHIBAURA sputter electrode deposition machine b) Si wafer mounted at sputter machine target c) Pt deposited on Si wafer	125
Figure 7.12. Glass substrate patterning process	126
Figure 7.13. a) SHINTO Sand blast machine b) Glass with hole patterned after sand blasting process	126
Figure 7.14. Wafer bonding of Si-Pt deposited with patterned glass substrate using SU-8 polymer	126
Figure 7.15. Finished single TEC device with cross section area 2 x 2 cm ² and 0.3 mm electrode separation.....	127
Figure 7.16 Seebeck and power measurement setup of TEC device	127
Figure 7.17. Single junction P-N TEC device.....	128

Figure 7.18. Solution resistance of iodide/triodide gel electrolyte at dependent temperature.....	128
Figure 7.19. Cyclic voltammetry analysis of a) iodide/triodide b) Fe ^{2+/3+} at various temperatures	129
Figure 7.20. Electrode formal extraction from CV analysis of a) iodide/triodide b) Fe ^{2+/3+} at various temperatures	130
Figure 7.21. Diffusion ratio extraction from CV analysis of a) iodide/triodide b) Fe ^{2+/3+} at various temperatures	130
Figure 7.22. Half-cell potential extraction from CV analysis of a) iodide/triodide b) Fe ^{2+/3+} at various temperatures	130
Figure 7.23. Seebeck extraction from CV analysis of a) iodide/triodide b) Fe ^{2+/3+} at various temperatures differences.....	131
Figure 7.24. Seebeck evaluation of single TEC devices of a) iodide/triodide b) Fe ^{2+/3+}	131
Figure 7.25. Power density evaluations of single TEC devices with various electrode separations a) 1 cm b) 1mm c) 0.3 mm and d) 0.2&0.25 mm	132
Figure 7.26. Single junction P-N TEC device and Seebeck evaluation.....	133
Figure 7.27. Power density evaluation.....	133
Figure 7.28. High density integrated cell microTEC device design	134
Figure 7.29. Electrolyte filling and sealing methodology of microTEC device	135
Figure 7.30. Mask design a) all layer overlap b) zoom and c) active area.....	136
Figure 7.31. Mask design a) intermediate layer with holes b) holes size and separation and c) inlet overlap with cell holes	136
Figure 7.32. Electrode mask patterning design a) upper electrode b) bottom electrode c) zoom upper electrode d) zoom bottom electrode and e) connector between electrodes	137
Figure 7.33. P-type and N-type inlet etching process	137
Figure 7.34. Photoresist layer on Si substrate after photolithography process	138
Figure 7.35. Inlet etching of Si wafer after deep RIE process	138
Figure 7.36. Electrode patterning process.....	138

Figure 7.37. Photo resist layer patterning overlap with inlet on Si-Ti-Pt substrate after photolithography and alignment process a) upper electrode and b) lower electrode..... 139

Figure 7.38. a) Photo resist layer patterning overlap with inlet after aligning b) inlet overlap with electrode pattern after photolithography and alignment process under microscope 139

Figure 7.39. a) Focus ion beam machine b) Si-Ti-Pt substrate attached on FIB target c) ion beam milling process 139

Figure 7.40. Electrode pattern under microscope after Ti-Pt etching using ion beam milling and after post residue removal process..... 140

Figure 8.1. Ideal SCO model for TEC energy harvesting..... 142

University of Malaya

LIST OF TABLES

Table 1 Circuit elements and current versus voltage relationship with impedance	30
Table 3.1. TEC material prepared	50
Table 3.2. Simulation results of molecular modeling studies	58
Table 3.3. Spectral (FTIR and UV-vis) and thermogravimetric data for metal complexes	66
Table 3.4. Reaction proposed	67
Table 3.5. CV analysis	67
Table 3.6. HOMO-LUMO gap and diffusion coefficient extracted from CV analysis ..	68
Table 4.1. TEC material prepared	79
Table 4.2. Cyclic Voltammetry Analysis where E_a =anodic potential; E_c =Cathodic potential; ΔE_p =Anodic-Cathodic potential separation	87
Table 4.3. Determined of diffusion coefficient, electrochemical HOMO-LUMO gap, molar conductivity, and Seebeck coefficient of samples	87
Table 5.1. Complexes formulae	102
Table 6.1. CV analysis	113
Table 6.2 Reversibility analysis	113
Table 6.3. Diffusion and HOMO-LUMO gap extraction from CV	114
Table 7.1. TEC material prepared	118
Table 7.2. Upper electrode Fabrication process	119
Table 7.3. Lower electrode Fabrication process	119
Table 7.4. Deep RIE Recipe	123
Table 7.5. Electrodeposition recipe	125
Table 7.6. I/I_3^- Seebeck generation with electrode separation 0.2 mm with different molarity and different PVA weight percentage	132

LIST OF ABBREVIATIONS

NAPIC	:	National Property Information Centre
LPG	:	Liquefied Petroleum Gas
LNG	:	Liquefied Natural Gas
AV GAS	:	Aviation gasoline
ATF	:	aviation turbine fuel
TE	:	Thermoelectric
TGE	:	Tawau Green Technology
GDP	:	Gross Domestic Product
TECs	:	Thermo-electrochemical cells
SCO	:	Spin crossover
HS	:	High spin
LS	:	Low spin
DFT	:	Density functional theory
Fe	:	Iron
Co	:	Cobalt
Mn	:	Manganese
MPN	:	3-methoxypropionitrile
DMSO	:	Dimethyl sulfoxide
PMMA	:	Poly(methyl methacrylate)
PVA	:	Polyvinyl alcohol
CV	:	Cyclic voltammetry
EIS	:	Electrochemical impedance analysis
TBATFB	:	Tetrabutylammonium tetrafluoroborate
OPM	:	Optical polarize microscopy

UV-Vis	:	Ultraviolet visible
Cryo-TEM	:	Cryogenic thermal electron microscopy
H ¹ -NMR	:	Nuclear magnetic resonance spectroscopy
MEMS	:	Micro-electro mechanicals
ILs	:	Ionic liquids
L	:	Ligand
TGA	:	Thermogravimetry analysis
FTIR	:	Fourier transform spectroscopy
DSC	:	Differential scanning calorimetry
DRIE	:	Deep Reactive Ion Etching
Pt	:	Platinum
Au	:	Gold
Si	:	Silicon
Wt%	:	Weight percentage

LIST OF SYMBOLS

S_e	:	Seebeck coefficient
ΔV	:	Electric potential different
ΔT	:	Temperature different
$S_{reaction}$:	Entropy reaction
n	:	Number of electron
F	:	Faraday constant
A	:	Product of reduction process
α	:	Moles of A
B	:	Reactant of oxidation
β	:	Moles of B
ε	:	Dielectric constant
Z_{ox}	:	Valence charges of the oxidant
Z_{red}	:	Valence charges of the reductant
E	:	Electronic charge
N	:	Avogadro's constant
S_A/ S_B	:	Partial molar entropy
S^*_A/ S^*_B	:	Eastman entropy of transport
S^{\ominus}_e	:	Transport entropy of electrons
P	:	Pressure
H	:	Enthalpy
$\Delta_r G$:	Gibbs free energy change per mole of reaction at electrode
$\Delta_r G^0$:	Gibbs free energy change per mole of reaction for bulk
K_{eq}	:	Equilibrium constant
R	:	Gas constant

Q_r	: Reaction quotient
K	: Thermal conductivity
W	: Electrical work
E^o	: Standard electrode potential
d	: Electrode separation
ZT	: Figure of merit
D_{lim}	: Limiting diffusion coefficient
c	: Concentration
CE	: Conversion efficiency
$[A]$: Concentration of the oxidised species
$[B]$: Concentration of the reduced species
γ_{ox}	: Activity coefficient of oxidized species
γ_{red}	: Activity coefficient of reduced species
E_f	: Electrode formal potential
v	: Scan rate
D_o	: Diffusion oxidation
D_R	: Diffusion reduction
σ	: Conductivity
Λ_m	: Molar conductance.
A_{abs}	: Absorbance
ϵ_{Abs}	: Molar absorptivity
χ_M^T	: Magnetic susceptibility
I_{fp}	: Oxidation limitation current peak
I_{rp}	: Reduction limitation current peak
E_a	: Anodic potential
E_c	: Cathodic potential

- D_{ox} : Diffusion coefficient oxidation
- D_{red} : Diffusion coefficient reduction
- I : Cell current
- P : Power

University of Malaya

LIST OF APPENDICES

Appendix A: Lab View.....	192
---------------------------	-----

University of Malaya

CHAPTER 1: INTRODUCTION

1.1 Energy consumptions in Malaysia

The Malaysia's total energy consumption grew rapidly from 1990 to 2015 with average annual growth rate of 7.9%. The transportation sector continues to be the country's largest consumer of energy with 45.2%, followed by the industry sector at 27% (Tenaga, 2015) as shown in Figure 1.1. Currently, the situation in Malaysia can be described as high demand of power consumption with increase of infrastructure and transportation technology in the urban areas, whilst increasingly high cost installment of infrastructure and maintenance of power plants in the rural area.

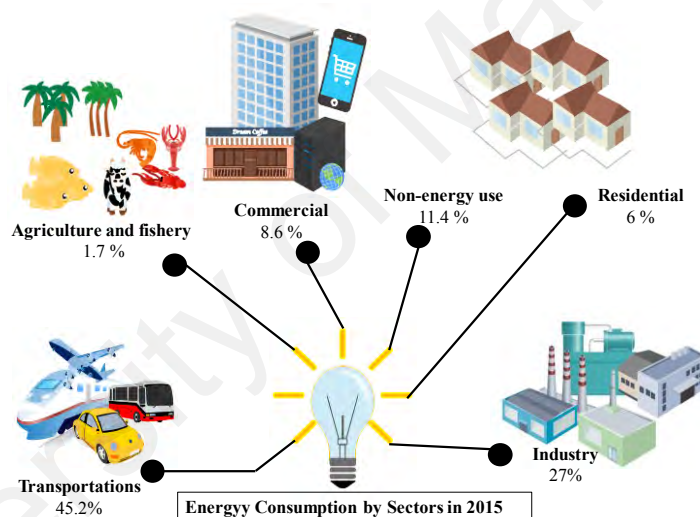


Figure 1.1. Total energy consumption by sectors in Malaysia

The energy consumption from the rail transport sector, increased with the development of Light Rail Transit (LRT) and Monorail system. The electricity consumption in the industry sector recorded an increase of 2.9%. Total electricity consumption of residential and commercial sectors increases with growth of 1.3% (Commission, 2015). These sectors are also highly dependable on liquefied petroleum gas (LPG), which is supplied to households, government buildings, hotels, hospitals and even airports as well as food courts and restaurants especially for cooking purpose. In peninsular Malaysia, electricity was accounted for more than 80% of energy consumption.

The Malaysia energy sector should consider the energy mix with new and renewable energy sources rather than relying only on fossil fuels. This is important because Malaysia indigenous energy resources are fast depleting and we are heavily dependent on energy imports as shown in Figure 1.2. Inevitably, this will expose Malaysia economy to international energy prices and security challenges.

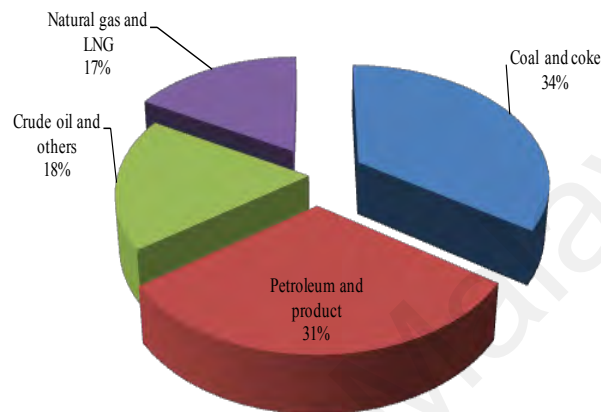


Figure 1.2. Malaysia energy primary supply imports

1.2 Thermoelectric (TE) as sustainable renewable energy in Malaysia

Malaysia is a tropical country characterized as warm and humid. The annual mean temperature is 26.4°C with average daily maximum temperature is 34°C and average daily minimum at 23°C (Jamaludin, Mohammed, Khamidi, & Wahab, 2015). Based on previous study (Jamaludin et al., 2015), the highest temperature difference in Kuala Lumpur and Bayan Lepas for indoor-outdoor temperature of residential building at urban area is around 2-5°C.

TE technology can offer sustainable renewable energy based on the temperature gradient conversion to electrical energy. When a thermal gradient is applied to the TE material, the mobile charge carriers in the material (electrons and holes) diffuse towards the cold side and this build-up of charge creates a potential difference which known as the Seebeck effect. The potential difference generated per unit temperature difference is

known as the Seebeck coefficient, (S_e). Low-grade waste heat (temperatures below 200 °C) examples produced by industrial or geothermal processes, is a particularly significant potential source of energy to be harvested for the production of electricity which suitable for Malaysia environment. Thermoelectric devices consist of stacking n-type and p-type material commonly semiconductor based material generally have limited efficiency at low temperatures, making them unsuitable for application in low-grade waste heat harvesting. Thermoelectric devices based on semiconductor materials generally produce potential differences in the order of μVK^{-1} and having limitations of their efficiency at near-ambient temperatures or low temperature gradient(Vining, 2009). Thermo-electrochemical cell (TEC) is alternative to TE for low grade heat waste in Malaysia.

Thermo-electrochemical cells, thermogalvanic cells or thermocells, are an alternative device design showing increasing promise for the conversion of low-grade thermal energy. As for thermoelectrics, thermocells can continuously generate electrical energy when a temperature gradient is present, without producing emissions or consuming any materials. When based on a redox-active electrolyte, such thermocells can generate potential differences in the order of mVK^{-1} which three order magnitude higher than semiconductor solid TE but the challenge is the conductivity is very low at μScm^{-1} hence the power density is also low at μWm^{-2} which still comparable with thin film solid TE(Dupont, MacFarlane, & Pringle, 2017). This makes them an interesting alternative to solid-state devices for low temperature thermal energy harvesting.

1.3 General Problem Statement

The power density of TEC is still low compared to the bulk solid TE even when possess high Seebeck coefficient at range of mVK^{-1} due to lower ionic conductivity at low temperature different(Yamada, Zou, Liang, & Kimizuka, 2018).

The incomplete understanding on the fundamental thermodynamic and electrochemical reaction of the TEC, results in difficulties on optimising the TEC. This can be done through understanding and optimising the fundamental thermodynamics as stated as follows:

1. Difficulties to find redox couples and electrolyte combinations **for high Seebeck coefficients and high ionic conductivity**.
2. The maximum possible cell operating temperature for aqueous **TEC limited at water boiling point** at 100 °C.
3. The **thermal gradient across TEC is also low** at less than 50 K temperature different which limits the application at high temperature.
4. Currently, the most significant factors limiting the application of TEC are their **low power output and conversion efficiency**. Most reported TEC devices have an energy conversion efficiency (relative to the Carnot engine) of <1
5. **High concentrated inorganic redox couple** can cause corrosion depending on the absolute potential of the redox couple.
6. For a TEC to generate energy continuously, it must contain both halves of the redox couple in solution and **preferably at high concentrations (0.5 mol dm⁻³ or higher) which is costly for certain good redox couple**.

1.4 Research Objectives

The objective of this thesis is as follows:

1. Design and synthesis new TEC composite material using **Spin Crossover (SCO)** material
2. Increase both Seebeck and conductivity using **low concentrations** of redox active material and **high boiling point** solvent.
3. Characterize new TEC composite material

4. **Change the physical state** of redox electrolyte in the same time **maintaining or enhance the TEC performance to prevent leakage** for TEC devices.
5. Propose microTEC device design and fabrication methodology

1.5 Overview

The dissertation work focuses on development of thermoelectrochemical energy power generation both at the fundamental and applied level. At the fundamental level, SCO material was proposed as potential for good TEC material that can enhance the properties ohmic conductivity, interfacial charge transfer resistance and lowering thermal conductivity thus have been improved for the based benchmark of electrolyte. While at the applied level, from the basic non-isothermal TEC cell (two compartments connected with salt bridge experimental setup to create temperature difference) investigated then converted to the basic isothermal TEC cell through microelectromechanicals (MEMS) fabrication technology process, thus highlighting the potential of this application to be implemented for end user applications.

CHAPTER 2: LITERATURE REVIEW

2.1 Introduction to the thermo-electrochemical cells (TEC)

Thermoelectric technology can offer sustainable renewable energy based on the temperature gradient conversion to electrical energy. When a thermal gradient is applied to the thermoelectric material, the mobile charge carriers in the material (electrons and holes) diffuse towards the cold side and this build-up of charge creates a potential difference which known as the Seebeck effect. The potential difference generated per unit temperature difference is known as the Seebeck coefficient(H. Zhou & Liu, 2018). Low-grade waste heat (temperatures below 200 °C) examples produced by industrial or geothermal processes, is a particularly significant source of energy that's the potential to be harvested for the production of electricity which suitable for Malaysia environment. Thermoelectric devices consist of stacking n-type and p-type material commonly semiconductor based material generally have limited efficiency at low temperatures, making them unsuitable for application in low-grade waste heat harvesting(Keppner et al., 2015). Thermoelectric devices based on semiconductor materials generally produce potential differences in the order of μVK^{-1} and having limitations of their efficiency at near-ambient temperatures or low temperature gradient.

Thermo-electrochemical cells, thermogalvanic cells or thermocells, are an alternative device configuration showing increasing promise for the conversion of low-grade thermal energy. As for thermoelectrics, thermocells can continuously generate electrical energy when a temperature gradient is present, without producing emissions or consuming any materials. When based on a redox-active electrolyte, such thermocells can generate potential differences in the order of mV K^{-1} which three order magnitude higher than semiconductor solid TE(Aldous, Black, Elias, Gelinas, & Rochefort, 2017; Chani, Karimov, Khan, & Asiri, 2015; Dupont et al., 2017). This makes them an interesting alternative to solid-state devices for low temperature thermal energy harvesting. TEC

have high potential for low grade heat energy harvesting, which the systems is capable in harnessing waste heat to provide power to energy conversion(Abraham, MacFarlane, & Pringle, 2011). As shown in Figure 2.1 and Figure 2.2, a potential arises in TEC is from diffusion layer and electrical double layer formation when the potential equilibrium between the electrolyte and electrode surface in a solution containing a redox couple is disturbed by the temperature gradient between the hot and cold electrodes(Abraham et al., 2011).

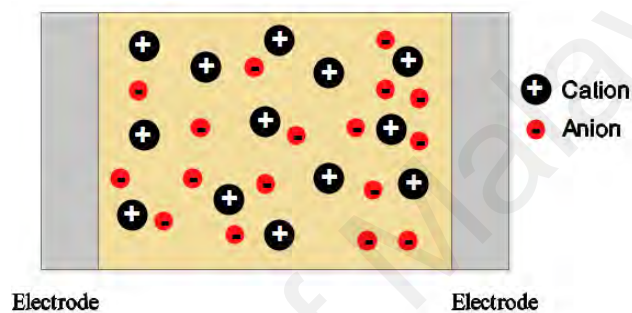


Figure 2.1. TEC in steady state at no temperature gradient (Equilibrium State)

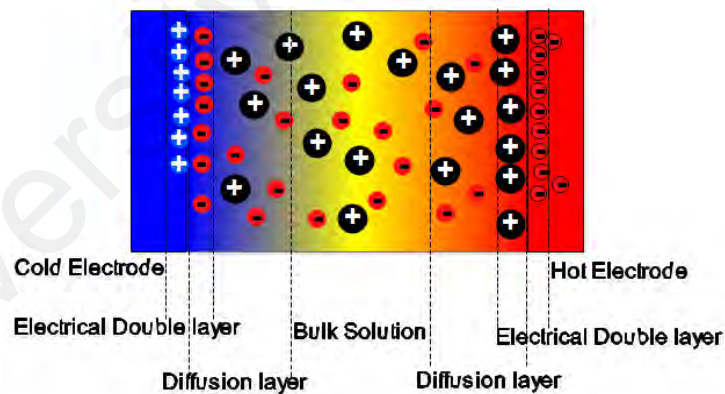


Figure 2.2. TEC in steady at temperature gradient

There have two types of TEC as shown in Figure 2.3 which a) non-isothermal TEC and b) isothermal TEC(Koerver, MacFarlane, & Pringle, 2015). The advantages of TEC system is there have no accumulation of reaction product which prevented by natural diffusion and convection which means no moving mechanical component needed for mass transport (Abraham et al., 2013). S_e is the important parameter for thermoelectric

power generation in TEC which define as the amount of thermoelectric voltage generated per temperature difference between hot side and cold side of the electrode. The TEC working principle will be explained in more detail in the following section.

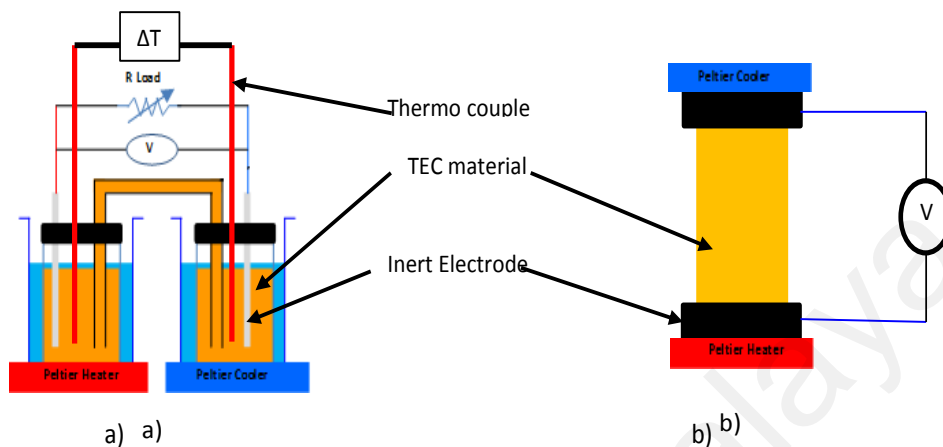


Figure 2.3. TEC a) Non-isothermal b) Isothermal

2.2 TEC working principles

2.2.1 Theory of TEC entropy reaction

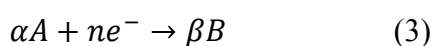
The Seebeck coefficient, (S_e) is an important thermo-electrochemical cell parameter where S_e is electric potential different, (ΔV) at temperature different, (ΔT) that related to the redox reaction entropy, ($S_{reaction}$) (Abraham et al., 2013)

$$S_e = \frac{\Delta V}{\Delta T} = \frac{\Delta S_{reaction}}{nF} \quad (1)$$

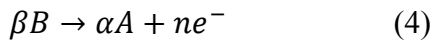
where n is number of electron involves in the redox reaction and F is faraday constant. For reversible redox reaction at working electrode, general chemical equilibrium can be described as equation (2-4)



Reduction



Oxidation



where B is product of reduction process and A is product of oxidation process, α is moles of A species and β is moles of B species. The redox process at hot anode and cold anode will lead to electron flow and travels through an external circuit and returns to the cell. The electrolyte composition is maintained by the balance of oxidized and reduced species.

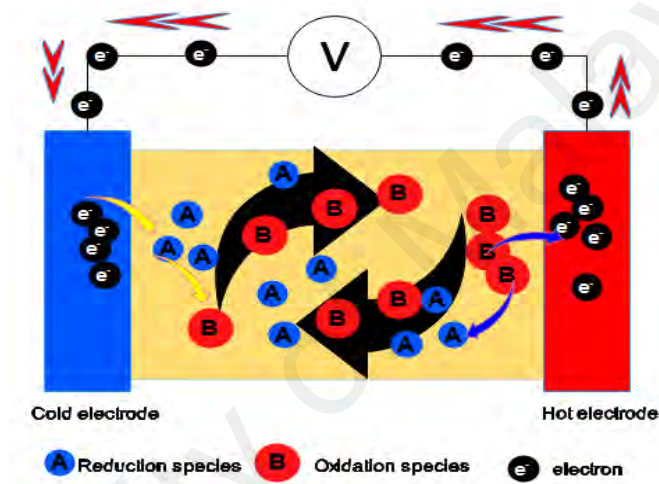


Figure 2.4. Redox process in TEC at temperature gradient

Based on Born's model as shown in Figure 2.5, $\Delta S_{reaction}$ is as expressed in equation (5) (Hupp & Weaver, 1984)

$$\Delta S_{reaction} = -\frac{e^2 N}{2\epsilon T} \left(\frac{d \ln \epsilon}{d \ln T} \right) \left(\frac{Z_{ox}^2}{r_{ox}} - \frac{Z_{red}^2}{r_{red}} \right) \quad (5)$$

Where ϵ is dielectric constant, Z_{ox} and Z_{red} are the valence charges of the oxidant and reductant, respectively, r_{ox} and r_{red} are the corresponding radius, e is the electronic charge and N is Avogadro's constant.

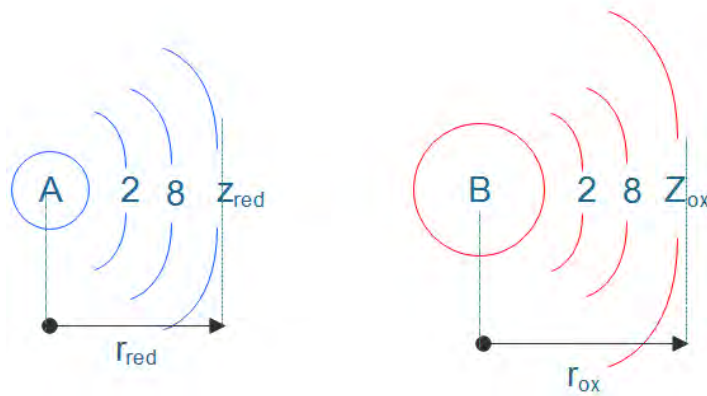


Figure 2.5. Born's model of A as reduction and B as oxidation species

2.2.1.1 Soret effect

The Soret effect or “thermophoresis” or thermo diffusion as shown in Figure 2.6 can affect the Seebeck coefficient by giving an initially higher value of Seebeck coefficient than the steady state value caused by the imbalance of velocities between ion molecules around the hot and cold electrode (Shindo, Arakawa, & Hirai, 2002). Due to the phenomenon of Soret effect, there will have concentration gradient in TEC across the hot side and cold side where the concentration of reactant at the cold side is higher than concentration of reactant at the hot side (Stefanie Uhl et al., 2014). However, Soret effect can be negligible for very high concentrations of electrolyte or very low electrode spacing due to no significance of species concentration gradient at both cold and hot electrodes (Ikeshoji, 1987).

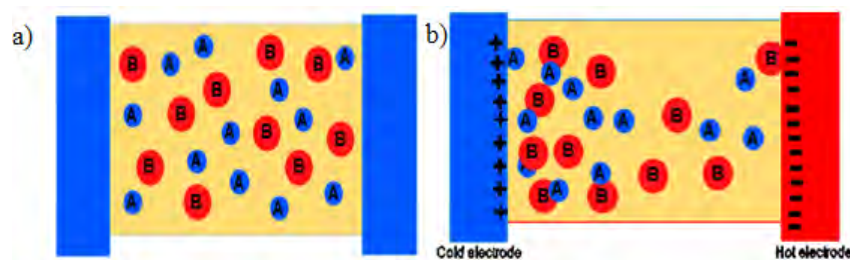


Figure 2.6. Soret effect a) no temperature different b) at temperature different

2.2.2 Theory of TEC heat transfer in relation with entropy reaction

In a liquid based TEC, ionic charge transfer is mediated by the electrolyte (fluid) flow. Thus the ionic charge transport discussed in the previous section is strongly coupled to thermally driven convection, and as a consequence this mass (fluid) flow also drive thermal flow in the TEC cell(Gunawan et al., 2014). Consequently, the imposed temperature gradient imposed at the respective TEC electrode terminal may be significantly diminished or heated, by the connection of the electrolyte. Generally, general strategies have been employed to mitigate this fluid thermal connection, either through gelation of the electrolyte or insertion of a membrane(Zhang et al., 2017).

Generally, the heat flow in TEC can be expressed by equation (4) where f_i is the heat flow rate induced by thermal conduction from hot electrode to the cold electrode and f_r is the rate of heat transfer induced by the reaction inside the TEC which can be in the forward or reverse heat direction depend on the enthalpy of the reaction, called thermal convection.

$$\frac{\partial Q}{\partial T} = f_i + f_r \quad (4)$$

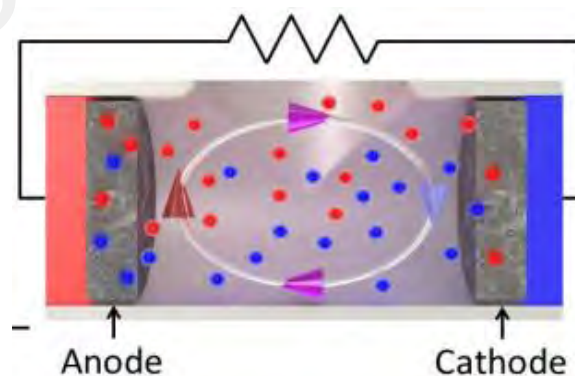


Figure 2.7. Convection and diffusion in TEC(Quickenden & Mua, 1995b)

Equation (20) can be expanded to be more detail by the given equation (21) where K is thermal conductivity of the TEC, A is the electrode area, and d is the distance between the two electrodes, and I is the cell current and ΔS is the entropy of cell reaction.

$$\frac{\partial Q}{\partial T} = KA \frac{\Delta T}{d} + \frac{IT\Delta S}{nF} \quad (5)$$

When no net consumption of the electrolytes in TEC caused by the natural reversibility of redox couple used, the expression of thermal power flow rate can be simplified to equation (6) which means very small and fast chemical reaction can be designed in TEC(Gunawan et al., 2013).

$$\frac{\partial Q}{\partial T} = KA \frac{\Delta T}{d} \quad (6)$$

2.2.3 TEC output power

The open circuit voltage produced by the TEC is dependent of entropy reaction $\Delta S_{reaction}$ which can be reaction of entropy at electrode-electrolyte interface as shown as equation (7).

$$\left(\frac{V_{oc}}{\Delta T}\right)_{t=0} = \frac{\Delta S_{reaction}}{nF} \quad (7)$$

The electrical power of TEC can be expressed as equation (8), where V_{oc} is open circuit voltage and I_{sc} is short circuit current, and ΔT is thermal gradient. The maximum electrical power is obtain if the internal load is equal to external load(Gunawan et al., 2013).

$$P = V_{oc}I_{sc} \quad (8)$$

2.2.4 A modified figure of merit ZT for TEC

Performance of thermoelectricity is measured by figure of merit, (.ZT). ZT is a unit-less parameter which included the effects of conductivity, (σ), thermal conductivity, (K)

and Seebeck coefficient at temperature gradient(Quickenden & Mua, 1995b). Generally for solid state thermoelectric, ZT was expressed as

$$ZT = \frac{S_e^2 \sigma}{K} \quad (9)$$

However, the conductivity of the electrolyte in TEC is not the only transport properties that affect TEC performance. A modified figure of merit that takes account of mass transport was introduced by Abraham et al. such that the figure of merit (now termed ZT) is more appropriately written as:

$$ZT = \left(\frac{z^2 F^2}{R} \right) \frac{S_e^2 D_{lim} c}{k} \quad (10)$$

Where S_e is Seebeck coefficient, k is thermal conductivity, z is charge on the ion, F is Faraday constant, R is gas constant, D_{lim} is limiting diffusion coefficient c is concentration of the redox couple.

The conversion efficiency of TEC, (CE) can be derived as equation (11). The CE which related to the maximum electrical power can be approximated as $V_{oc}I_{sc}$ that is related to the S_e and the conductivity of electrolyte while input heat is depends on the electrolyte thermal conductivity, cell thickness and, in some cases, natural or forced convection(Salazar, Stephens, Kazim, Pringle, & Cola, 2014).

$$CE[\%] = \frac{\text{Maximum electric power}}{\text{Input heat}} \times 100 \quad (11)$$

Where the relative efficiency with respect to Carnot efficiency, CE_r can be derived as

$$CE_r = CE \left(\frac{T_H}{\Delta T} \right) \quad (12)$$

2.3 TEC capability

Figure 2.8 show TEC capability for energy harvesting. TEC is an alternative to overcome solid TE device that has an efficiency limitation at low temperature gradient. Seebeck generation which three orders of magnitude higher than semiconductor solid TE in TEC makes them an interesting alternative to solid-state devices for low temperature thermal energy harvesting(Quickenden & Mua, 1995b).

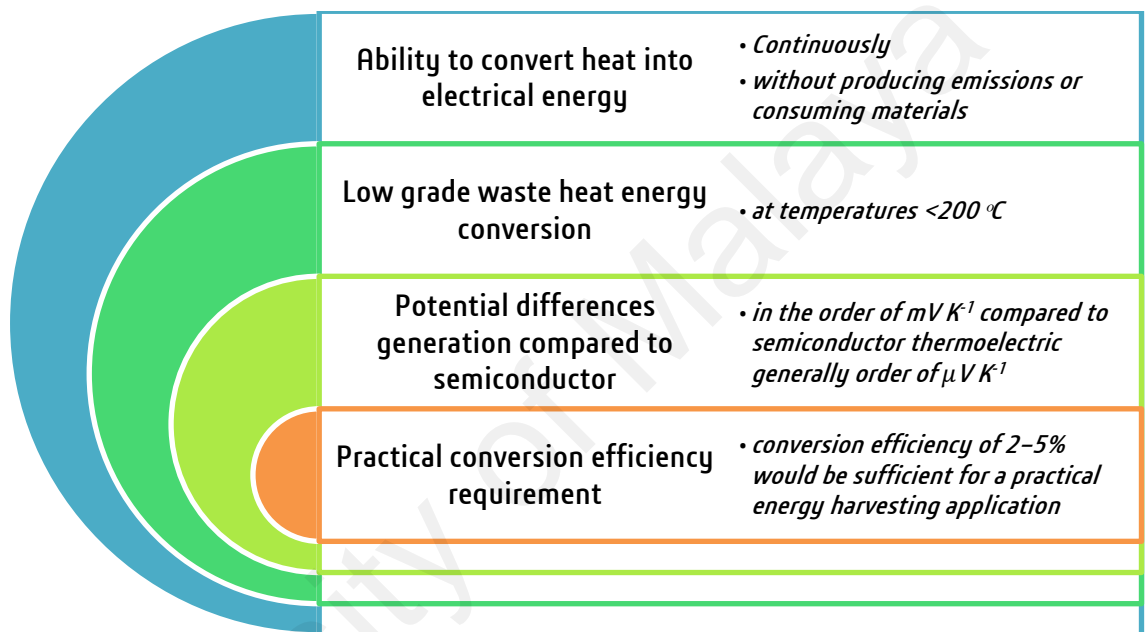


Figure 2.8. TEC power generation capability

2.4 Recent Development of TEC

Recently, the development of TEC is focusing on redox couples, electrolyte properties, electrode materials and cell design and optimization(Dupont et al., 2017). The reasons are to increase the potential difference that can be generated in a cell, and increasing the current density at the electrodes. As discussed below, all of these aspects are currently being investigated as potential strategies for improving the performance of TEC devices.

2.4.1 Redox couples

Aqueous ferri/ferrocyanide $Fe(CN)_6^{3-}/Fe(CN)_6^{4-}$ has a Seebeck coefficient of $-1.4 mV K^{-1}$ that depends slightly on concentration(Dupont et al., 2017). The Seebeck coefficient

of other redox couples can exhibit considerably greater concentration dependence than ferri/ferrocyanide. One example is the iodide/triiodide I^-/I_3^- redox couple, which has been studied in a range of aqueous and non-aqueous solvents (Abraham et al., 2013). The Seebeck coefficient of this redox couple in ethylammonium nitrate (EAN) ionic liquid changes 3 fold between concentrations of 0.01M and 2M, with a maximum value of 0.97mVK^{-1} measured in 0.01 M solution. The Seebeck coefficient for iodide/triiodide is positive, attributed to the positive entropy change associated with the increase in the number of molecules upon reduction. The $\text{Co}^{2+/3+}(\text{bpy})_3(\text{NTf}_2)_{2/3}$ redox couple (bpy=2,20-bipyridyl), $\text{NTf}_2 = \text{bis}(\text{trifluoromethanesulfonyl})\text{amide}$ was tested in a variety of solvents and a maximum Seebeck coefficient of 2.19mV K^{-1} for an 0.01 M solution in 3-methoxypropionitrile (MPN) was observed (Abraham et al., 2011). This high Seebeck coefficient can be attributed to the change in spin state (Spin crossover (SCO) effect) of $\text{Co}^{2+/3+}$ when it is oxidised or reduced in most coordination complexes, which adds an additional electronic contribution to the total entropy change (Abdullah et al., 2015). Solutions of 1-ethyl-3-methylimidazolium ($[\text{C}_2\text{mim}]$) $[\text{NTf}_2]$ containing either ferrocene/ferrocenium (Fc/Fc^+), iodide/triiodide (I^-/I_3^-) or a mixture of Fc and iodine (I_2), which forms the ferrocene triiodide salt (FcI_3), were examined previously (H. Y. Zhou, Yamada, & Kimizuka, 2016). The Seebeck coefficients were measured for Fc/Fc^+ (0.10mV K^{-1}) and I^-/I_3^- (0.057mV^{-1}) and compared to the FcI_3 redox couple (0.81mV K^{-1}). These authors also combined I_2 with a range of substituted ferrocenes, the highest Seebeck coefficient being 1.67mV K^{-1} for 1,10-dibutanoylferrocene (DiBoylFc) (Anari et al., 2016). Organic redox couples, such as thiolate/disulphide (McMT^-/BMT) which has a Seebeck coefficient of -0.6mV K^{-1} . The Seebeck coefficient for $\text{Cu}^{2+}/\text{Cu}(\text{s})$ system is 0.84mV K^{-1} (for $0.7\text{M}\text{CuSO}_4$) but cannot be operated continuously as the anode will eventually be consumed (Lin et al., 2013). This recent redox couple development and how they are interlinked are shown in Figure 2.9.

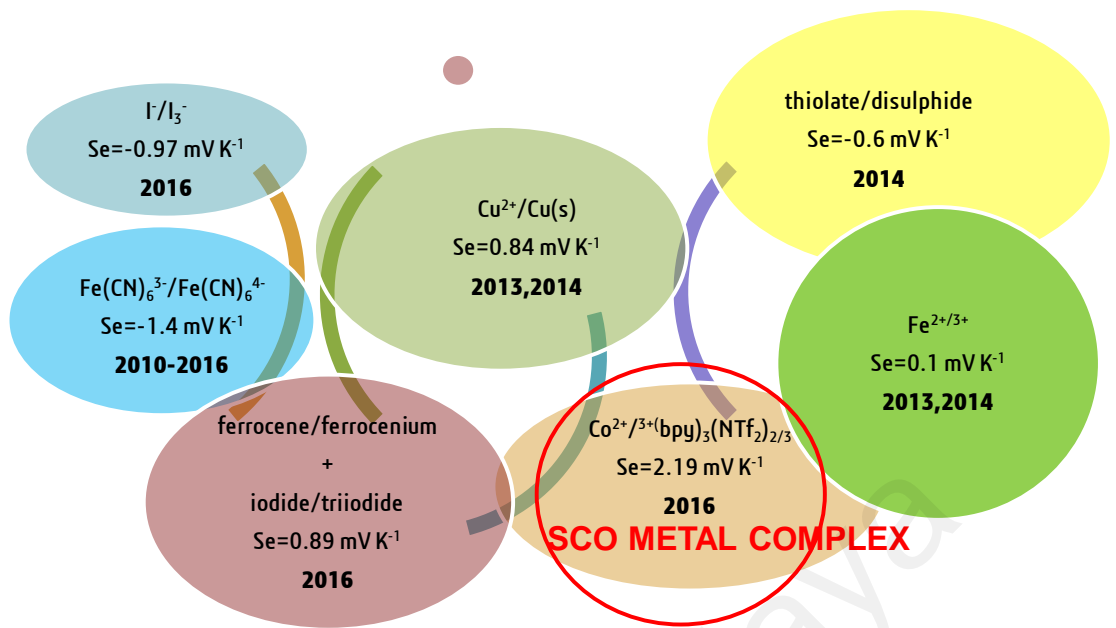


Figure 2.9. Recent development of redox couple

2.4.2 Electrolyte properties

Electrolyte development for TEC was critical due to low conductivity compared to semiconductor solid state TE devices(Laux et al., 2016; Migita, Tachikawa, Katayama, & Miura, 2009; Sun, Pu, & Tang, 2016; Yamato, Katayama, & Miura, 2013; Zhang et al., 2017). However, it can be tuned by several strategies as shown in Figure 2.10 that will be explained more detail in the next section.

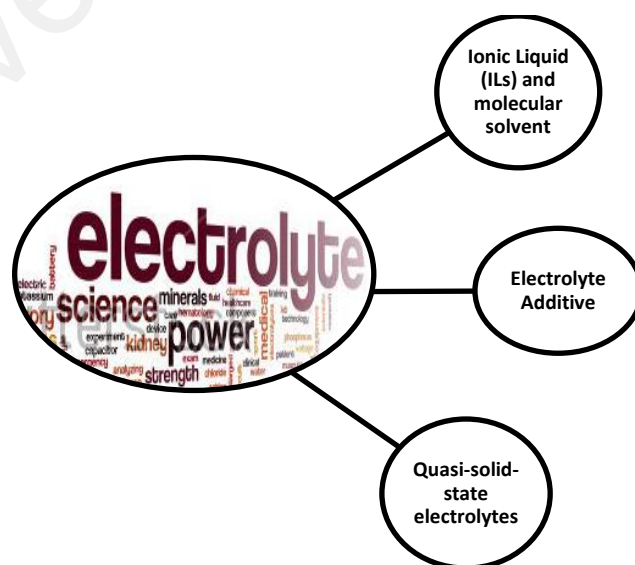


Figure 2.10. Recent development of TEC electrolytes

2.4.2.1 Ionic liquid and molecular solvent

Aqueous electrolytes generally exhibit higher power output due to the relatively fast diffusion of ions but having drawback of low boiling point of water that limits the operating temperatures of such devices to 100 °C. Non-aqueous electrolytes can be used to solvate redox couples that are water insoluble, or to utilise redox couples with oxidation states that are unstable in aqueous environments. Unique solvation environment provided by ILs may result in larger entropy changes upon oxidation/reduction of the redox couple, leading to higher S_e (Abraham et al., 2013).

The S_e of a range of iron redox couples in 1-butyl-1-methylpyrrolidinium bis(trifluoromethanesulfonyl)amide ([C₄mpyr][NTf₂]). Fe(CN)₆^{3-/4-} in [C₄mpyr][NTf₂] was 1.49 mV K⁻¹ compared with -1.4 mV K⁻¹ in water (Gunawan et al., 2013).

The Seebeck coefficients for a number of iron-based redox couples in different ILs that have been investigated previously suggest that the redox reaction entropies are dominated by Coulombic interactions between the redox couple and electrolyte ions with the opposite charge to the redox couple (Migita et al., 2009). The positively charged redox couple Fe(bpy)₃^{3+/2+} had a similar Seebeck coefficient in all ILs containing the [NTf₂] anion ([C₄mpyr][NTf₂]: 0.45 mV K⁻¹, [C₂mim][NTf₂]: 0.5 mV K⁻¹ and 1-methyl-1-propylpiperidinium (PP13) [NTf₂]: 0.49 mV K⁻¹) but had a significantly smaller S_e in [C₄mpyr] bis(perfluoroethylsulfonyl)amide ([NPf₂]) (0.33 mV K⁻¹). The authors also observed that the S_e of the redox couple was affected by the charge density of the IL ions, where an increase in charge density led to an increase in the absolute magnitude of the S_e . Iodide/triiodide redox couple in a range of ILs found that the maximum power output were determined by the nature of both the IL cation and anion. The best performance for an IL was achieved with 0.4 M I⁻/I₃⁻ in 1-ethyl-3-methylimidazolium tetrafluoroborate

([C₂mim][BF₄]), with a measured S_e of 0.23 mV K⁻¹ and a maximum power output of 29 mW m⁻².

2.4.2.2 Electrolyte Additive

Another strategy to improve TEC is by improving mass transport of the charge carrier with addition of other species to the electrolyte (Kazim & Cola, 2016). The addition of CNTs and poly-(3,4-ethylenedioxythiophene)–poly(styrenesulfonate) (PEDOT:PSS) to an aqueous ferri/ferrocyanide electrolyte had showing improvement of the power output by 30% (Salazar, Stephens, et al., 2014). Interestingly, host–guest interaction of I⁻/I₃⁻ by adding a-cyclodextrin to the electrolyte capable to increase the S_e from 0.86 to 1.45 mV K⁻¹ (Anari et al., 2016).

2.4.2.3 Quasi-solid-state electrolytes

To avoid leakage of the electrolyte quasi-solid state electrolyte had been develop by combination of a solid (e.g. polymer) and liquid component (Jin, Greene, MacFarlane, & Pringle, 2016; Wu, Black, & Aldous, 2017). The optimal cellulose concentration (5 wt%) the power output only decreased by 20%, compared to the aqueous electrolyte. The increment of the S_e of quasi-solid electrolyte had mass transport limitation.

2.4.3 Electrode materials

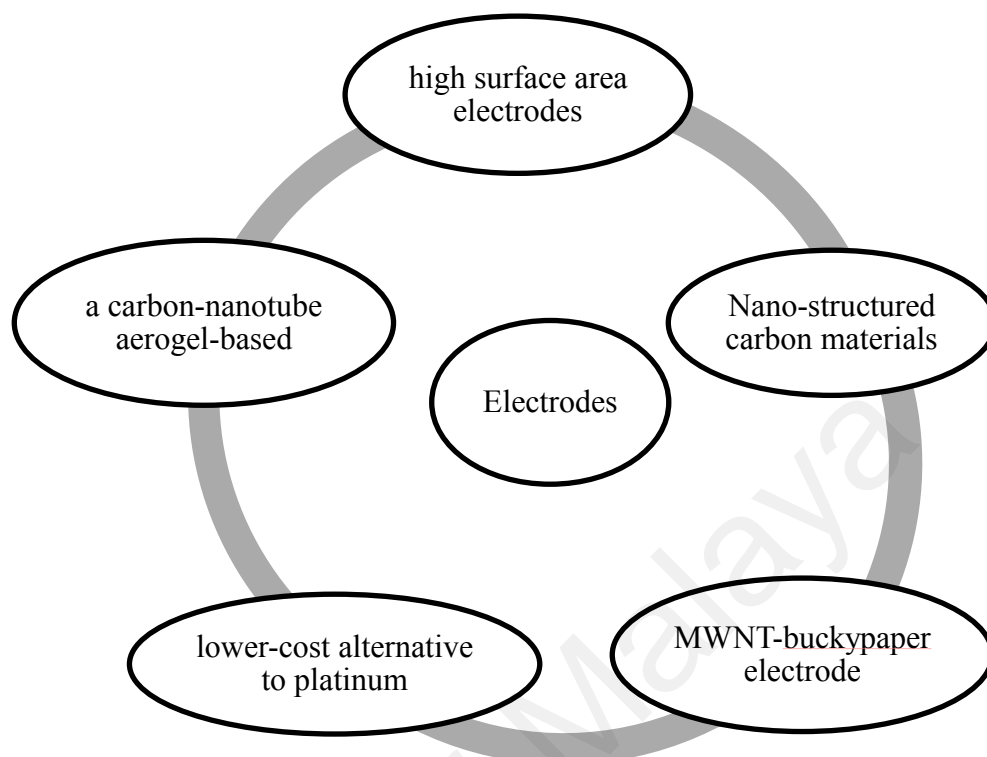


Figure 2.11. Recent development of TEC electrode

The electrocatalytic performance of electrodes is depended on the redox couple used in TEC. It requires optimisation for each redox electrolyte system which will be challenging in TEC electrode development. The strategy to optimise TEC performance for electrode is by increase the power of TEC by using high surface area electrodes(Nugent, Santhanam, Rubio, & Ajayan, 2001). Previously, nano-structured carbon material which having high surface area that can increase the number of reaction site had been reported. A carbon based electrode and MWNT-buckypaper shown alternative lower cost and 33% higher power output than expensive noble platinum electrode. In the other hand, carbon nano tube aerogel based electrode was the highest TEC conversion reported in aqueous ferri-ferrocyanide with 3.95% conversion efficiency(Hu et al., 2010).

2.4.4 Cell design and optimization

Figure 2.12 shown recent cell optimization development of TEC devices that will be explained in detail in next section which cover cell modeling optimization, series stacking of TEC cell to enhance voltage output, separators and membranes inserted in TEC cell to lower thermal conductivity and cell orientation and electrode spacing optimization.

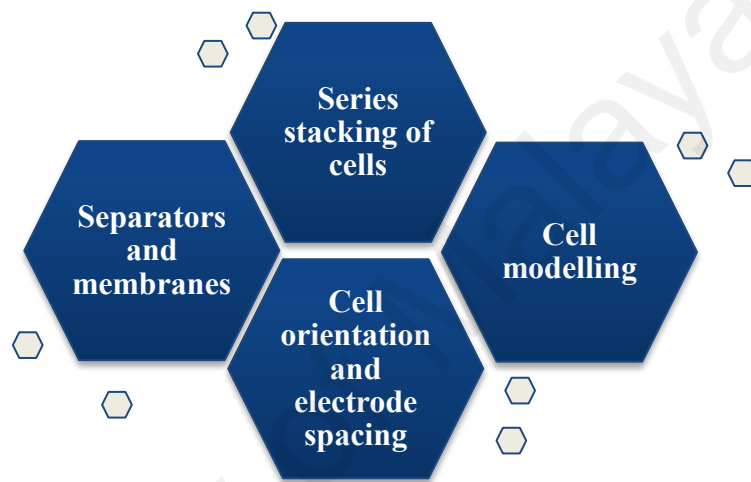


Figure 2.12. Recent cell optimization development of TEC devices

2.4.4.1 Cell modeling

Cell modeling of TEC previously reported to optimize TEC power output by optimizing TEC design parameter using experimental value of redox potential, diffusion coefficient, thermal conductivity, viscosity and other electrochemical properties. The simulation study use experimental parameter to simulate the current density and power curves(Salazar, Kumar, & Cola, 2014). The study prove that the natural convection increases mass transfer of the electrolyte by a factor of 8 by making the thermocells in series stacking that capable increase the overall conversion efficiency due to optimization of the natural convection impact on mass and heat transfer in the individual cells.

2.4.4.2 Cell orientation and electrode spacing

In the other study (Dupont et al., 2017; Kang et al., 2012; Quickenden & Mua, 1995a), the investigation of the cell orientation and electrode spacing had been done. Hot over cold vice versa and vertical orientation of electrode had been investigated where the maximum output of TEC was when the orientation of the electrode can have natural convection to enhance mass transport. Hot over cold orientation can limit the convection that decrease the mass transport.

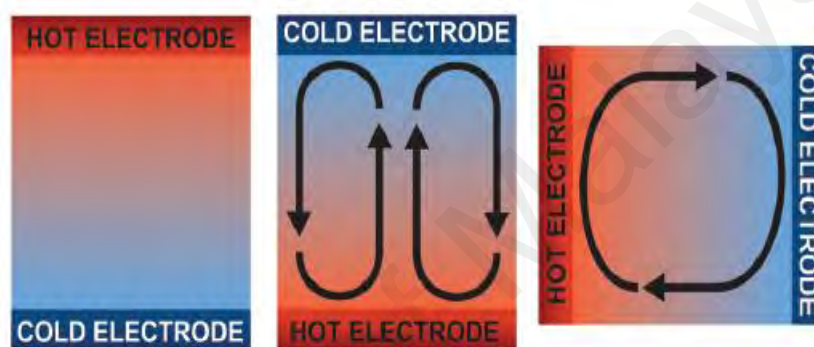


Figure 2.13. TEC cell orientation natural convection investigation (Salazar, Kumar, et al., 2014)

2.4.4.3 Separators and membrane

Separators and membrane rapidly used in designing battery cell to separate electrolyte within the cell for separate redox reaction at anode and cathode. In TEC, separator and membrane with specific thermal conductivity which depend on membrane type can maintain large thermal gradient to enhance TEC performance (Zhang et al., 2017). Hasan et al. had demonstrate by introduce PVDF membrane in TEC where the optimal performance was when the membrane was positioned in the middle of the cell and having same distance between both hot and cold electrode using iodide/tri-iodide redox couple in aqueous solution. The thermal distribution studies across the TEC demonstrated the significance of the membrane and separator in TEC to maintain large thermal gradient that act as self-cooling system in TEC (Hasan et al., 2016).

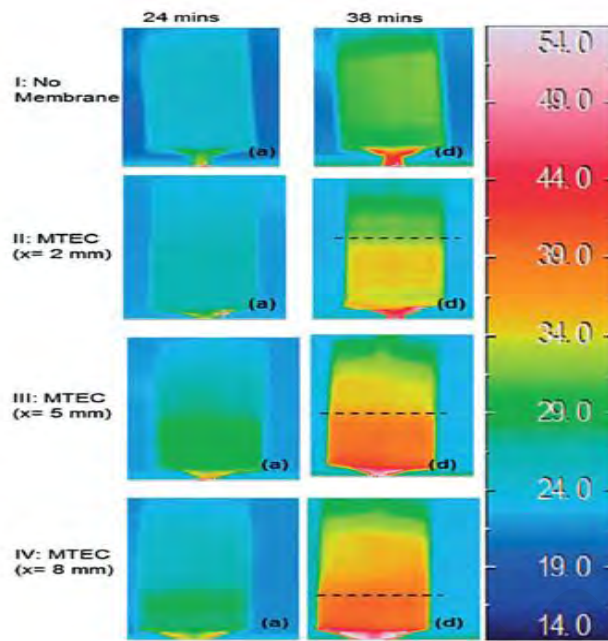


Figure 2.14. Thermal distribution of inserted membrane TEC(Hasan et al., 2016)

In an other study, cotton membrane was used as separator and the optimal performance was when the membrane was positioned near to the cold electrode. Increases the thickness of the membrane also decrease the power performance of the TEC.

2.4.4.4 Series stacking of cell

TEC performance also limited by low output voltage. Series stacking of numbers of TEC cell can increase the TEC output voltage significantly(S. Uhl et al., 2015). The similar concept that used in solid state thermoelectrics, are equivalent to the n-type and p-type semiconductor stacking in series to maximize power output in which multiple thermoelectric couples are connected in series to maximise power output. For same Seebeck sign, series stacking of the TEC cell will more difficult compared to the TEC cell which having positive and negative S_e . The potential of PVA-based hydrogel electrolyte containing either ferri/ferrocyanide or ferric/ferrous chloride had been demonstrated to be double up but the current are remain the same for series stacking TEC(Zhang et al., 2017).

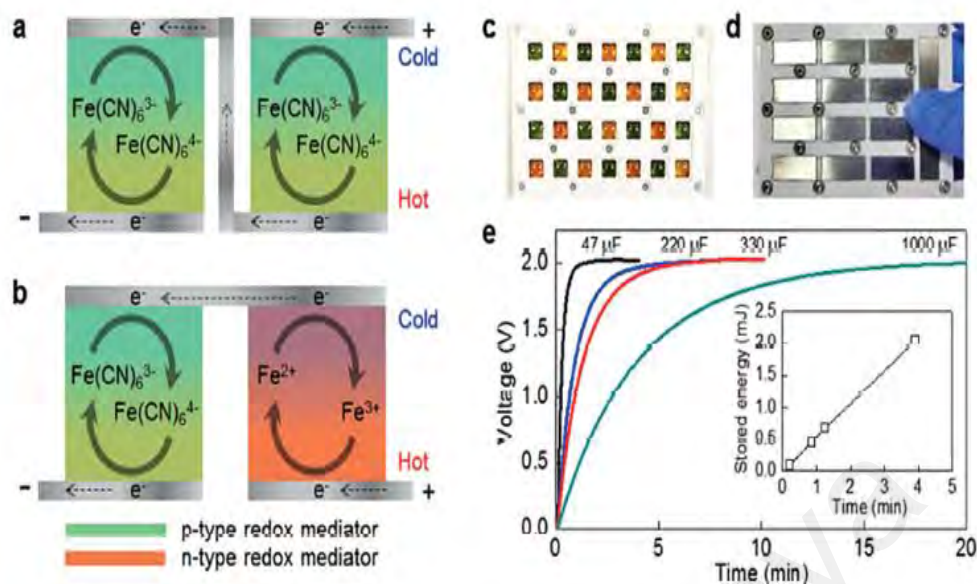


Figure 2.15. Series stacking TEC a) same electrolyte b) p/n-type electrolyte c) Photograph of alternating n-type and p-type mediators for a thermocell array with 14 n–p cells d) Photograph of the sealed thermocell array for the redox couple array in (c), which shows the top plate that completes the electrical connections e) the voltage–time curves of different capacitors when charged by four series-connected thermocell arrays(Zhang et al., 2017)

2.5 Theory of Cyclic Voltammetry of TEC

Cyclic voltammetry (CV) is electroanalytical technique that can study electroactive species mechanism. The ease of CV measurement has resulted in extensive use of this kind analysis in the fields of electrochemistry, inorganic chemistry, organic chemistry, and biochemistry. Cyclic voltammetry is very useful for the first experiment performed in an electrochemical study of a compound, a biological material, or an electrode surface. The effectiveness of CV results from its capability for rapidly observing the redox behavior over a wide potential range(Kissinger & Heineman, 1983). The resulting voltammogram is analogous to a conventional spectrum in that it conveys information as a function of an energy scan. Cyclic voltammetry technique use working, counter and reference electrode. The applied electrode potential is varied from an initial value voltage to a final value voltage at a constant scan rate. Once the final potential value is reached the direction of the scan is reversed while maintaining the same scan rate where the potential brought back to the initial value. The example of single redox reaction cyclic

voltammogram trend is as shown in Figure 2.16. In the two cases the form of the potential-time impulse. The Cyclic voltammetry technique can be used to confirm redox reaction by determine the redox peak(Nicholson, 1965).

The maximum potential difference that can be generated in TEC is determined by the Seebeck coefficient of the redox couple, which represents the entropy change that occurs when the species is oxidised or reduced. The entropy change is influenced by factors including the structural changes in the redox species and effects from their solvent shells and their interactions with the solvent. It has been observed in both aqueous and non-aqueous solvents that the sign of the entropy change (positive or negative) is related to the difference between the absolute charges of the oxidant and reductant. This reflects the strength, of the primarily Columbic, interaction between the charged redox species and its solvation shell. If the absolute charge of the oxidant is larger than the reductant, the S_e is positive (and vice versa). For practical TEC requirements such as stability, electrochemical reversibility can be confirmed using cyclic voltammetry analysis as shown in Figure 2.16 where the material needs to be able to reduce and oxidise. This is shown by the redox peak. This measurement requires both oxidation states of the redox couple in solution.

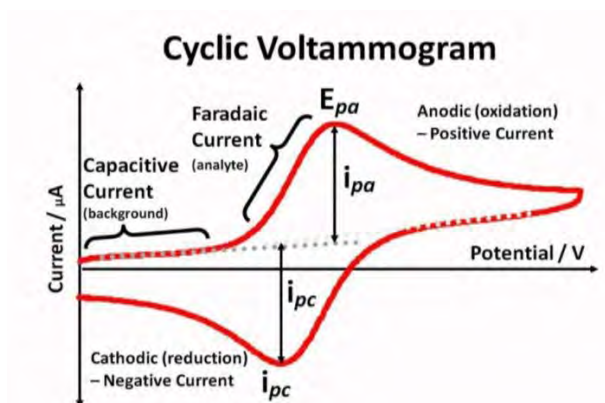


Figure 2.16. Cyclic Voltammogram of single redox reaction

2.5.1 Theoretical derivation of Seebeck coefficient using CV

For a single working, counter and reference electrode dip in SCO solution as shown in Figure 2.17(a), the reaction quotient, (Q) is a function of the activities or concentrations of the chemical species involved in a chemical reaction, can be represented as equation (13 and 14)

$$Q_{reduction} = \frac{[B]^\beta}{[A]^\alpha} \quad (13)$$

$$Q_{oxidation} = \frac{[A]^\beta}{[B]^\alpha} \quad (14)$$

Where $[A]$ is the concentration of the oxidised species and $[B]$ is the concentration of the reduced species.

To understand further the relation of the entropy reaction to electrochemical properties, the Nernst equation is applied for S_e estimation. The sign of the entropy change (positive or negative) is related to the difference between the net charges of the oxidation and reduction agents. This can be derived directly from the diffusion coefficients of the oxidation and reduction agents above. This reflects the strength of the primarily Columbic interaction between the charged redox species and its solvation shell. If the absolute charge of the oxidant is larger than the reduction, the S_e is positive (and vice versa). The redox reaction is in equilibrium at initial steady-state condition, and the equilibrium potential can be expressed by $[A]$ and $[B]$ at the working electrode for an isothermal (no temperature gradient) cell as shown in equation (15-17):

$$E = E_f + \frac{RT}{nF} \ln Q \quad (15)$$

$$E = E_f + \frac{RT}{nF} \ln \frac{[B]^\beta}{[A]^\alpha} \quad (16)$$

$$E_f = E^0 + \frac{RT}{nF} \ln \frac{\gamma_{ox}}{\gamma_{red}} \quad (17)$$

where R is the standard gas constant, and E_f is the formal potential, E_0 is standard electrode potential, γ_{ox} and γ_{red} are the activity coefficient of oxidized and reduced species respectively.

However, for an actual TEC cell, the device can be considered to have two working electrodes as shown in Figure 2.17, each for the hot and cold side. Consequently, the Nernst relation will be more complicated. Figure 2.18 shows an example of the TEC cell that possess a temperature gradient across the cell when the hot side is at working electrode 1 (Platinum) and the cold side at working electrode 2 (Platinum).

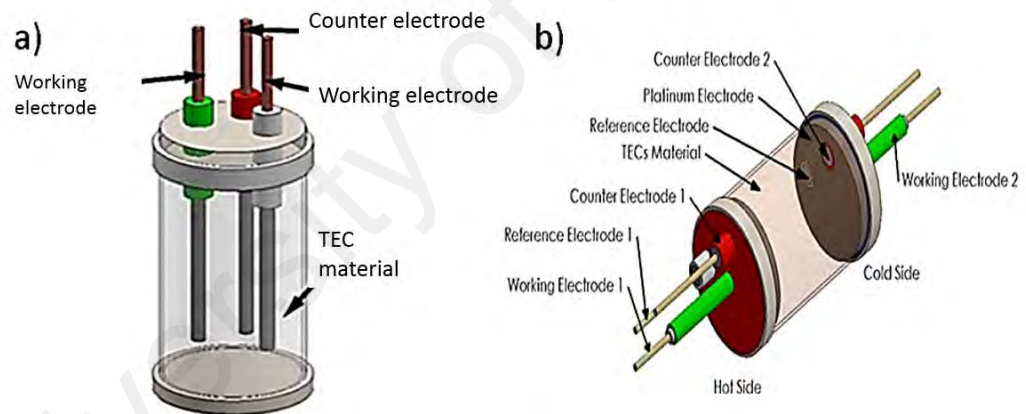


Figure 2.17. Isothermal Cell of TEC having a) one working electrode b) two working electrode

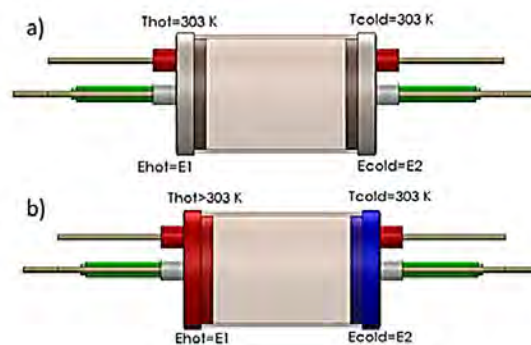
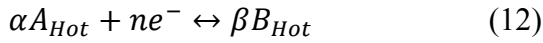


Figure 2.18. TEC a) no temperature gradient and b) at temperature gradient

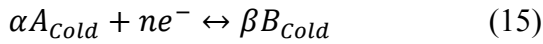
The equilibrium reaction at the hot side can be expressed as



$$Q_{Hot} = \frac{[B]^{\beta}}{[A]^{\alpha}} \quad (13)$$

$$E_{Hot} = E_{f_{Hot}} + \frac{RT_{Hot}}{nF} \ln \frac{[B]^{\beta}}{[A]^{\alpha}} \quad (14)$$

The equilibrium reaction at the cold side can be expressed as



$$Q_{Cold} = \frac{[B]^{\beta}}{[A]^{\alpha}} \quad (16)$$

$$E_{Cold} = E_{f_{Cold}} + \frac{RT_{Cold}}{nF} \ln \frac{[B]^{\beta}}{[A]^{\alpha}} \quad (17)$$

S_e can be expressed as the potential difference between hot and cold working electrodes over a temperature gradient as shown in equation (18).

$$S_e = \frac{E_{Hot} - E_{Cold}}{T_{Hot} - T_{Cold}} \quad (19)$$

Using the condition of equation, can be described in detail by expressing the equations for the hot side and cold side as follows:

$$\Delta T = T_{hot} - T_{cold} \quad (20)$$

$$\Delta E_f = E_{f_{HOT}} - E_{f_{COLD}} \quad (21)$$

$$S_e = \frac{\Delta E_f}{\Delta T} + \frac{R}{nF\Delta T} (T_{hot} \ln \frac{[B]^{\beta}}{[A]^{\alpha}} - T_{cold} \ln \frac{[B]^{\beta}}{[A]^{\alpha}}) \quad (22)$$

Initially, at $\Delta T=0$, the TEC system is in thermal equilibrium at a constant, uniform temperature and uniform ion number densities. The initial condition, as stated above, shows that the reaction at both hot and cold electrode cancels each other out, which shows that both have the same potential at the same temperature. The potential, E can be determined by using cyclic voltammetry technique at initial temperature (room temperature).

When there is a temperature gradient in the TEC, the activity of the redox process at the hot and cold electrode creates an over potential which is more than the initial equilibrium potential, due to diffusion and convection. The sign of the sum potential of the TEC cell depends on the Q and E_f values. Identical electrodes used in TEC possess with the same E_f at no temperature gradient, now possess different E_f due to the difference in the electrochemical band gap energy for both electrodes, which allows electron transfer to complete the circuit. As the heat propagates across the TEC, the charge carriers migrate toward the cold electrode (via the Soret effect) which is balanced by the Brownian diffusion and electromigration caused by an induced electric field. The migration of charge carriers were at different rates at both hot and cold electrode (according to the reduce Sorret Coefficients) which results in a difference in the concentration gradient and the regions of net charge near the electrodes.

Temperature dependent cyclic voltammetry (CV) can be used to determine Seebeck coefficient (Koerver et al., 2015). Cyclic voltammetry techniques for determining S_e can be employed, even only in one part of the redox couple. Synthesis and isolation of both species can be impractical or expensive. Thus, it is beneficial to have a method in which only one species is necessary to predict redox couple Seebeck coefficient, to facilitate the preliminary investigation of new redox materials. Studies on reaction entropies of transition metal complexes indicated the applicability of cyclic voltammetry (CV)

techniques. The half-wave potentials extracted from cyclic voltammetry are based on thermodynamic, plus kinetic contributions:

$$E_f = 1/2 (E_{pa} - E_{pr}) \quad (23)$$

$$E_{1/2} = E_f - \frac{RT}{2nF} \ln \left(\frac{D_o}{D_R} \right) \quad (24)$$

The diffusion coefficients of both redox species have to be examined, and can be calculated from the Randles-Sevcik equation, which relates the diffusion coefficient for a known concentration, C, at a certain temperature, to the scan rate (ν) and electrode area, A:

$$i_p = 0.4463FAC \left(\frac{nFD}{RT} \right)^{1/2} \nu^{1/2} \quad (25)$$

Diffusion coefficients were calculated based on the i_p values from the lowest sweep rate ($n = 5$ mV/s) for all temperatures. The diffusion rate of both redox species increases significantly with temperature, which demonstrates that the diffusion limitation of redox species in viscous IL electrolytes at room temperature can be overcome at higher temperatures due to mass transport rates become greatly enhanced.

2.6 Theoretical of Electrochemical Impedance Spectroscopy (EIS) of TEC

Electrochemical Impedance Spectroscopy analysis (EIS), is a powerful technique to study the characteristic of a device and transport studies of TEC. TEC have a solution-electrode interface, solution-solution interface, redox process, and etc. The electrochemical interfaces and reaction in TEC can be expressed in terms of equation based on electrical equivalent circuits as shown in Figure 2.19 that will be explain in detail in next section. Electrical representations of physicochemical phenomena, such as

resistance, capacitance, or inductance are useful in understanding the physicochemical phenomena in TEC.

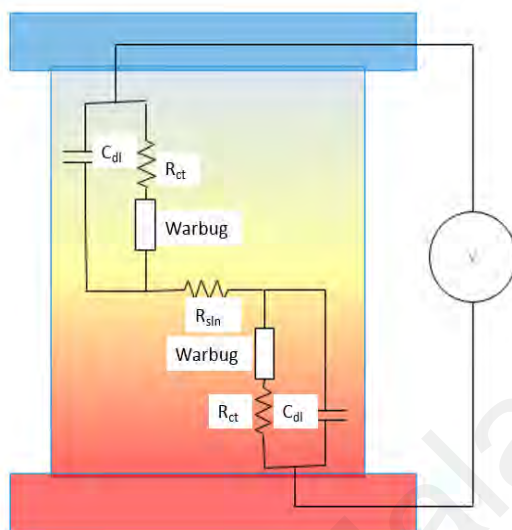


Figure 2.19. Example of TEC electrical equivalent circuit

2.6.1 Electrical Circuit Elements

EIS data are commonly analysed using an equivalent electrical circuit model. Most of the circuit elements in the model are common electrical elements such as resistors, capacitors, and inductors. The elements selected in the model must have a basis in the physical electrochemistry of the system. For example, most models use resistors to model the cell's solution resistance. Knowledge of the impedance of standard circuit components is therefore essential. Table 1 lists the common circuit elements, the equation for their current versus voltage relationship, and their impedance.

Table 1 Circuit elements and current versus voltage relationship with impedance

Component	Voltage relation with current	Impedance
Resistor	$E = IR$	$Z = R$
Inductor	$E = L di/dt$	$Z = j\omega L$
Capacitor	$I = C dE/dt$	$Z = 1/j\omega C$

Polarizable electrodes also known as blocking electrode, if immersed in a solution containing supporting electrolyte can be represented as a connection of the solution resistance and electrode capacitance in series. The impedance Z can be expressed as equation 54. In a three-electrode setup, the working electrode (WE), counter electrode (CE), and reference electrode (RE) are immersed in a cell and connected to the potentiostat. R_s is solution resistance and C_{el} is electrode capacitance of the electrode surface which is a product of real surface area S_r , and the specific double layer capacitance, C_{dl} of of the electrode.

$$\hat{Z} = R_s + \frac{1}{j\omega C_{el}} \quad (26)$$

$$C_{el} = S_r C_{dl} \quad (27)$$



Figure 2.20. Equivalent circuit of double layer formation

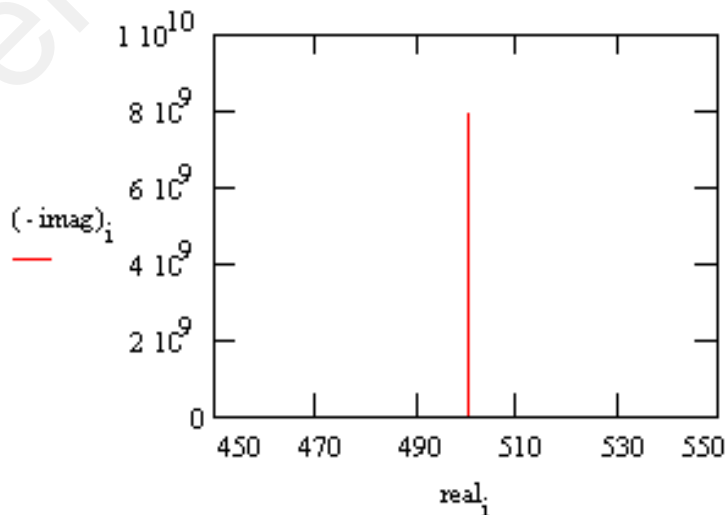


Figure 2.21. Nyquist plot of double layer impedance

In a two-electrode cell, C_{el} represents the sum of the capacitance of the working and counter electrodes as expressed in equation 56 below.

$$\frac{1}{C_{el}} = \frac{1}{C_{WE}} + \frac{1}{C_{CE}} \quad (28)$$

In the presence of redox species in solution, an electrochemical process involving the transfer of electrons between the electrode and species in solution may occur at a certain potential. Impedance of the Faradaic reactions can be represented by the faradaic impedance, Z_f , in parallel with the electrode capacitance, as shown in the equivalent circuit of Figure 2.22.

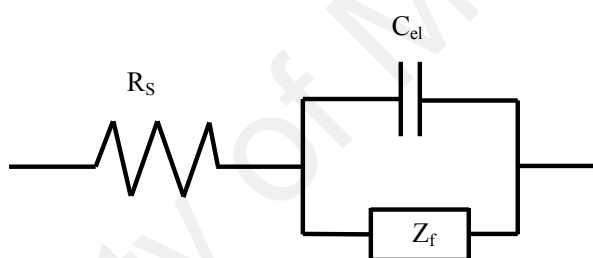


Figure 2.22. Equivalent circuit for Faradaic reaction

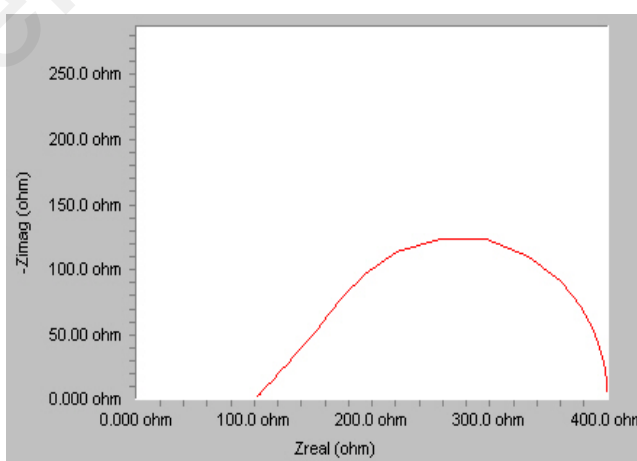


Figure 2.23. Nyquist plot of Faradaic impedance using Gamry software

The faradaic impedance consists of one real part arising from the derivative and is called the charge transfer resistance, R_{ct} , and the second part containing $j^{1/2}$ is called the

mass transfer impedance, Z_W , which, in the case of semi-infinite linear diffusion, is called the Warburg impedance and is composed of two parts: Z_{WO} and Z_{WR}

$$\widehat{Z}_f = R_{ct} + Z_W \widehat{=} R_{ct} + \widehat{Z}_{WO} + \widehat{Z}_{WR} \quad (29)$$

The frequency of relaxation time of the material for successful charge carrier transfer to the electrode can be investigated by dielectric loss relaxation time analysis by plotting the loss tangent plot from impedance (Arof, Amirudin, Yusof, & Noor, 2014). The loss tangent plots of these samples were calculated from fraction of imaginary dielectric permittivity (ϵ_i), and real dielectric permittivity (ϵ_r) according to the equation:

$$\tan \delta = \frac{\epsilon_i}{\epsilon_r} \quad (30)$$

$$\epsilon_r = \frac{Z_i}{(Z_r^2 + Z_i^2)} \left(\frac{d}{\omega \epsilon_0 A} \right), \epsilon_i = \frac{Z_r}{(Z_r^2 + Z_i^2)} \left(\frac{d}{\omega \epsilon_0 A} \right) \quad (31)$$

where, d is electrode distance, ω is angular frequency, A is electrode surface area, Z_r is real impedance and Z_i is imaginary impedance. The peak frequency of the loss tangent plot is the frequency of relaxation time of the material for charge carrier transfer. The change of the spin state of SCO material due to molecular distortion can be identified through changing of the relaxation time where higher conductivity expected to have relaxation frequency peak at lower frequency.

2.7 Potential of spin cross over material for TEC application

Molecule with valence electronic configurations ($3d^4-3d^7$) with ligands of intermediate field strength (mostly N-donors) are widely studied as spin crossover materials, (SCO)(Abdullah et al., 2015). They have labile electronic configurations that may be switched reversibly from high spin, (HS) to low spin, (LS), or vice versa, when subjected to an external stimulus, such as temperature, pressure, light or magnetic field(Murray, Oshio, & Real, 2013). Complexes with higher percentages of low spin are

expected to be more stable compared to the complexes with higher percentages of HS which are more distorted due to the Jahn-Teller effect (Shongwe et al., 2014). Complexes are expected to experience the Jahn-Teller distortion if the ground electronic configuration of the complexes is orbital degenerate and asymmetrically filled, which results in a complex distortion of the molecular geometry in order to remove the degeneracy and achieve a lower energy. Recently, SCO complexes have been studied as materials for TEC applications, with significantly large S_e ($\sim 2 \text{ mVK}^{-1}$) values reported, making them promising TEC candidates. Whilst the values of S_e of SCO solutions are reasonably high, i.e. approximately $5e^{10}$ times higher than the Seebeck coefficient of semiconductor based thermoelectric materials, its power output is limited by a low ionic conductivity.

The capability of manipulating electronic spin state of charge carrier using temperature without applying magnetic field make spin crossover (SCO) material attractive as TEC material (Vasu, Gorla, & Murthy, 2017; Vela, Verot, Fromager, & Robert, 2017). The different of molecular structure between high spin (HS) state and low spin (LS) state can contribute to high entropy reaction thermodynamically depend on the spin state transition dependent of temperature (Hofbauer et al., 2012). The entropy change accompanying the crossover from the LS and HS state vice versa expected to affect the entropy of redox reaction of the complexes. HS state is usually elongated molecule than LS which more compressed molecule due to repulsion of electron that can be described as Jahn-Teller distortion. The different entropy reaction between HS and LS is due to the different energy levels of the molecule and the different electronic configuration in the molecular orbital of the material that differentiates the HOMO-LUMO gap energy for both states. Temperature distribution across TEC can stimuli HS and LS state of SCO complex depends on magnetic susceptibility of material dependent of temperature as shown in Figure 2.24.

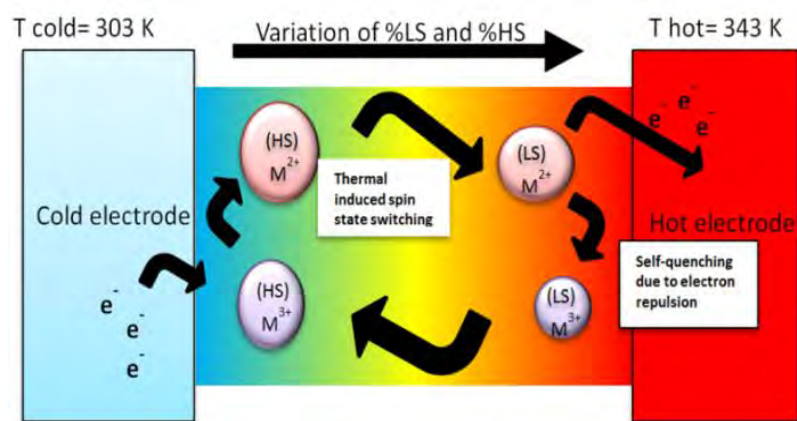


Figure 2.24. SCO effect of SCO material

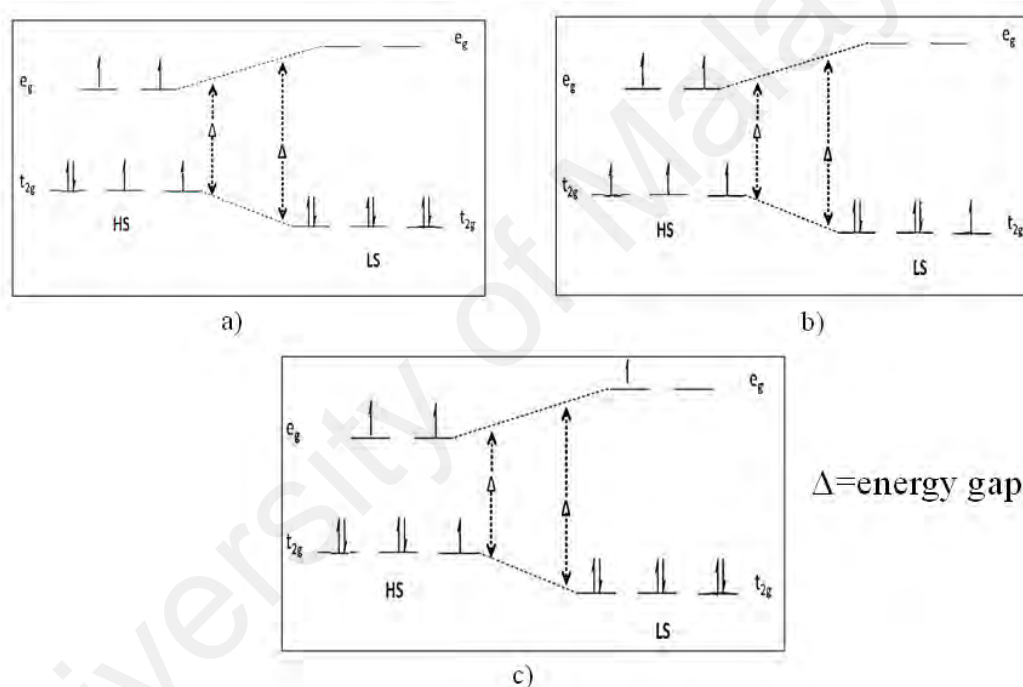


Figure 2.25. Energy gap of HS/LS a)Fe b)Mn c)Co

HOMO-LUMO gap energy influences the ease of redox process and conductivity (Rotaru et al., 2012) for every state for HS and LS is different for complexes. For Fe^{2+} , the LS state is at higher HOMO-LUMO gap energy than the HS state, due to the inexistence of unpaired electron in LS state compared to the existence of unpaired electron in HS state. For Mn^{2+} and Co^{2+} , the electron configurations are more complicated to explain in term of the ease of redox process because both HS and LS are having

unpaired electron. The molecular modeling approach can help to calculate HOMO-LUMO gap energy for each state.

Thermally induced spin crossover is due to the higher electronic degeneracies of the LS form and lower vibrational frequencies of the HS form, thus increasing the entropy. The changes in the metal-ligand vibrational mode of the complexes, emphasizing the transition of spin state where it can be observed from the shift of excitation energy frequency in the stretching vibrational modes of LS state to a HS state vice versa. SCO complexes in solution can provide insight into ligand field effects on the SCO complex, as well as probe interactions with charge balancing ions, added salts as supporting electrolyte and other solvent as guest molecules. The entropy difference based on SCO (ΔS_{spin}) can be expressed by the equation:

$$\Delta S_{spin} = R \ln[(2S + 1)_{HS}/(2S + 1)_{LS}] \quad (38)$$

2.7.1 Jahn-Teller theorem

Jahn-Teller distortion is the geometrical distortion of molecules or ions which due to the asymmetry electron configurations occupied in the orbital (Kugel' & Khomskiĭ, 1982). The Jahn-Teller theorem stated that a non-linear molecule is unstable in a degenerate state and will distort to remove the degeneracy. It was proven particularly relevant to transition metal complexes (Janes & Moore, 2004). The octahedral complex will suffer weak and strong Jahn-Teller distortion if electron unevenly occupied in T_{2g} and E_g orbital respectively as shown in Figure 2.26. Stable SCO molecules inferred to have fast relaxation due to small radius of charge carrier that lead to high mobility, high Seebeck coefficient and high conductivity. The high stable of SCO ionic complexes design is targeted in this study to optimise SCO material for TEC application. Theoretically, $Fe^{2+/3+}$ complex show high possibility for stable SCO complex due to having both stable Fe^{2+} LS state and Fe^{3+} HS state for redox reaction that having SCO effect. Compared to $Mn^{2+/3+}$

and $\text{Co}^{2+/3+}$, both complexes suffer Jahn-Teller distortion for redox reaction for having SCO effect.

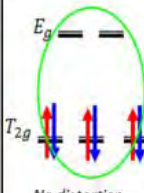
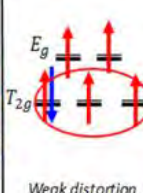
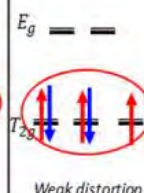
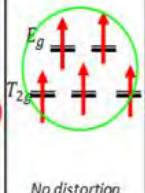
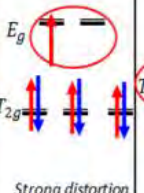
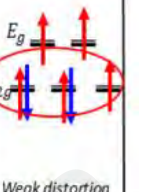
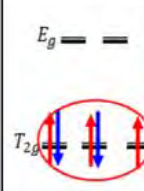
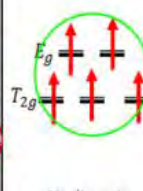
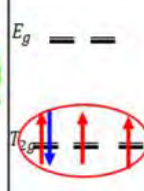
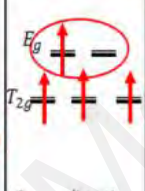
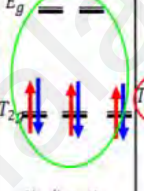
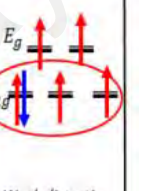
Fe(II)		Mn(II)		Co(II)	
Low Spin	High Spin	Low Spin	High Spin	Low Spin	High Spin
 No distortion	 Weak distortion	 Weak distortion	 No distortion	 Strong distortion	 Weak distortion
Fe(III)		Mn(III)		Co(III)	
Low Spin	High Spin	Low Spin	High Spin	Low Spin	High Spin
 Weak distortion	 No distortion	 Weak distortion	 Strong distortion	 No distortion	 Weak distortion

Figure 2.26. Jahn-Teller distortion

2.8 Practical Requirement of TEC for renewable energy

From the literature review discussed above, propose strategies for practical application of TEC in order to harvest low grade heat waste to electrical energy as follows should be considered;

- Thermal conductivity of TEC material should be design to be as low as possible
 - a) Redox couple concentration used need to be optimize for maximum energy and type of electrolyte used in the TEC system should be high in boiling point
 - b) Ionic liquids (ILs) have high boiling points and low vapor pressure, they generally exhibit relatively high ionic conductivity combined with low thermal conductivity
- Mass transport resistance need to be minimized to reduce electrical losses.

- a) *Finding the minimum electrode separation to increase the short circuit current in the same time maintaining the thermal gradient which quite be challenging without a proper TEC heat thermal insulation system*
- Electrochemical band gap energy is minimum energy required to allow redox reaction and electron transfer at the electrode which should be lower as possible to generate large current densities.
 - a) *Material type use in TEC system needs to be design to overcome large band gap energy. In this work we use SCO material taking advantages of changing band gap energy by spin state transition electron configuration*
- TEC should have high electrode kinetic reaction and surface area where the type of electrode used must be catalytic to the TEC material. Platinum is universal catalytic noble material. This expensive noble metal is not practical to use as electrode for TEC application.
 - a) *The metal can be replaced by using cheaper high conductive catalytic electrode such as graphite and graphene*
- TEC devices should be design as free leakage to maintain electrolyte composition.
 - a) *The physical state of the material for the TEC can be tuned in term of viscosity. Maintaining the TEC performance while changing the physical state of the material to become more viscous to prevent leakage, is a useful strategy to emphasize*
- Redox couples which be used in a TEC require stability, electrochemical reversibility and availability.
 - a) *Cyclic voltammetry analyses need to be used to confirm reversibility of the material(Y. Zhou, Yang, Lam, & Huang, 2016)*

CHAPTER 3: THERMO-ELECTROCHEMICAL GENERATION OF PURE MN, FE AND CO WITH N-DONOR LIGANDS CARBON CHAIN 14 AND BENZOATE AS COUNTER ION WITHOUT KI-KI₃

3.1 Introduction

The capability to manipulate the electronic spin state of charge carriers using temperature, without applying any magnetic field, makes spin crossover (SCO) material attractive as TEC material. Complexes of first-row transition metal ions (valence electronic configurations $3d^4 - 3d^7$), with ligands of intermediate field strengths (mostly N-donors) are widely studied as SCO materials. Studies of TEC electrolytes have shown that the ionic conductivity increases as a function of increased concentration of the redox couple, but at the expense of a reduced S_e .

Development of thermo-electrochemical cell based on spin cross over material for harvesting low grade heat waste, requires understanding of the behavior of temperature dependence of its electrochemical properties. The S_e and power density analysis of octahedral Fe, Mn and Co spin cross over material in solvents, need to be supported by molecular modeling and electrochemical analysis. High performance of TEC was contributed by its high diffusion ratio and low electrochemical HUMO-LUMO gap energy. The selectivity of transition metal type significantly effects the ligand distortion which leads to high S_e and ionic conductivity of the complex depends on polarity of the solvent. The sign of the S_e also found depend on the electrode formal potential and diffusion activity which can be determined from the temperature-dependent cyclic voltammetry analysis.

The aim of this work is to evaluate the potential of standalone SCO material as TEC material using both molecular modeling(simulation) and electrochemical(experimental) methods. Temperature dependent cyclic voltammetry analysis was performed using the

three electrodes setup in the isothermal cell to evaluate electrode formal potential and diffusion coefficient ratio, in order to investigate electrode kinetic (electrode potential) and its thermodynamic (diffusion activity) contribution to the TEC performance. Thus, this chapter gives perspective on how to optimize the complexes.

3.2 Methodology

3.2.1 Octahedral SCO ion complex design

The octahedral structure for a spin crossover ionic complex is chosen for its thermal stability and reversibility of redox reaction. A solution containing a redox couple, spin crossover complex and an appropriate solvent will be evaluated for its thermoelectrochemical generation capability. The molecular structure of the SCO complexes were designed to possess a central hydrophilic group containing a metal centre (Co, Mn, Fe) with a net positive charge which is surrounded with a electropositive group (neutral ligand) bond as shown in Figure 3.1. The metal ligand interaction and electro positivity of the complexes to the ionic solvation will expected to increase the entropy reaction (Hupp & Weaver, 1984). The structure of the complexes was designed to be an octahedral structure where a central transition metal atom was surrounded by six nitrogen atoms. The three ionic complexes are $[\text{Mn}(\text{cyclam})(\text{L14})_2](\text{R})_2 \cdot 4\text{H}_2\text{O}(\text{Mn})$, $[\text{Fe}(\text{cyclam})(\text{L14})_2](\text{R})_2 \cdot 2\text{H}_2\text{O}(\text{Fe})$, and $[\text{Co}(\text{cyclam})(\text{L14})_2](\text{R})_2 \cdot 3\text{H}_2\text{O}(\text{Co})$, where cyclam = 1,4,8,11-tetraazacyclotetradecane, L14 = 4-tetradecyloxypyridine, and R = $\text{C}_6\text{H}_5\text{CO}^-$ ion. The structural formulae of cyclam and L14, and the proposed structural formulae of these complexes are shown.

In order to drive the SCO effect for the octahedral structure, L (a monodentate N-donor neutral ligand) were used in order to tap the possibility of separating the small energy difference between the two states of t_{2g} and e_g in the d-orbital based on strong field ligand interaction to the metal. The metal ions used in this study were, Mn^{2+} ($3d^5$), Fe^{2+} ($3d^6$),

and Co^{2+} ($3d^7$) surrounded by cyclam (a macrocyclic N_4 -donor neutral ligand) and as previously stated, L (a monodentate N-donor neutral ligand) were chosen as they were expected to form SCO complexes with higher percentages of low spin (LS) metal²⁺ atoms. In addition, cyclam has been shown to form kinetically and thermodynamically stable complexes with many transition metal ions, while L increases the solubility of these complexes in organic solvents, and allows for good thermal energy absorption which results from the breaking of weak intermolecular forces between the long alkyl chains. The long alkyl chains used in this study was expected to create stable low spin state at high temperature of the metal complex (Halcrow, 2014; Hayami, Gu, Yoshiki, Fujishima, & Sato, 2001) as strategy to having high S_e . The high S_e founded from $[\text{Fe}(\text{CN})_6]^{4-}$ complexes was reported previously in the low spin state condition and a diamagnetic complexes (Gutlich, Hauser, & Spiering, 1994).

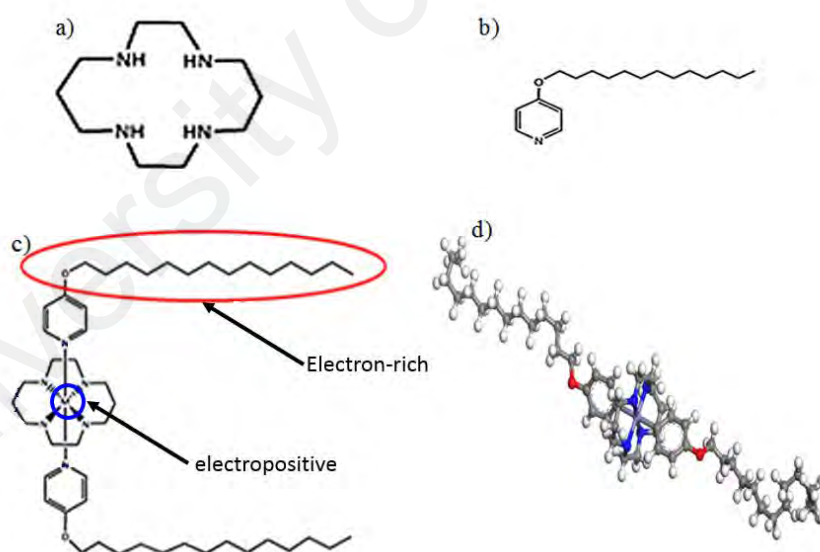


Figure 3.1. SCO material design used for TEC material a) cyclam b) N-donor ligand 14 c) and d) $\text{M}=[\text{Mn}]^{2+}$, $[\text{Fe}]^{2+}$, $[\text{Co}]^{2+}$ calculated molecular structure

	Fe ²⁺	Mn ²⁺	Co ²⁺
High Spin	 Paramagnetic	 Paramagnetic	 Paramagnetic
Low Spin	 Diamagnetic	 Diamagnetic	 Paramagnetic
	Fe ³⁺	Mn ³⁺	Co ³⁺
High Spin	 Paramagnetic	 Paramagnetic	 Paramagnetic
Low Spin	 Diamagnetic	 Diamagnetic	 Diamagnetic

Figure 3.2. d-orbital electronic configuration for HS/LS for Fe, Co and Mn

3.2.2 Molecular modeling

Molecular modeling was used to investigate physical chemistry relation with the chemical and electrochemistry properties that contributes to the TEC output performance for initial octahedral structure and ligand design. The simulation tools used is BIOVIA Material Studio 7.0 which involves geometry optimization, density states calculation, and electrochemical HUMO-LUMO gap energy calculation and optic spectrum analysis (to investigate octahedral d-orbital electronic configuration properties effect to the molecular distortion)

The molecular modeling in this study had shown the complexes properties from theoretical calculation which explain how much significant SCO effect to the molecular geometry distortion of the complexes that affect the Seebeck coefficient based on thermodynamic and electronic geometry optimization. The results of this molecular conformation are of key interest to illustrate the significant effect of the spin state transition on the molecular conformation of metal complexes.

Geometrical and energetic stabilities of molecular structure were investigated for both HS and LS condition using the density functional spin polarized calculations and Perde-

Burke-Ernzerhof (PBE) exchange–correlation functional(Delley, 2006; Perdew, Burke, & Ernzerhof, 1996) using Material Studio Dmol³ module in BIOVIA simulation tools. The methodology flow and the parameter definition of the simulation tool are given in Figure 3.2 and Figure 3.3 respectively. The Kohn–Sham equation was expanded in a double numeric quality basis set with spin polarization (DNP) (Delley, 2006; Inada & Orita, 2008). Energetic convergence tolerance is to be under 10⁻⁵ Ha, the Hartree-Fock self-consistent field (SCF) tolerance is limited to be fewer than 10⁶. Spin state effect calculations uses point energy calculations to calculate each spin state conditions. Energy was calculated using the same settings used in the geometrical optimization setup.

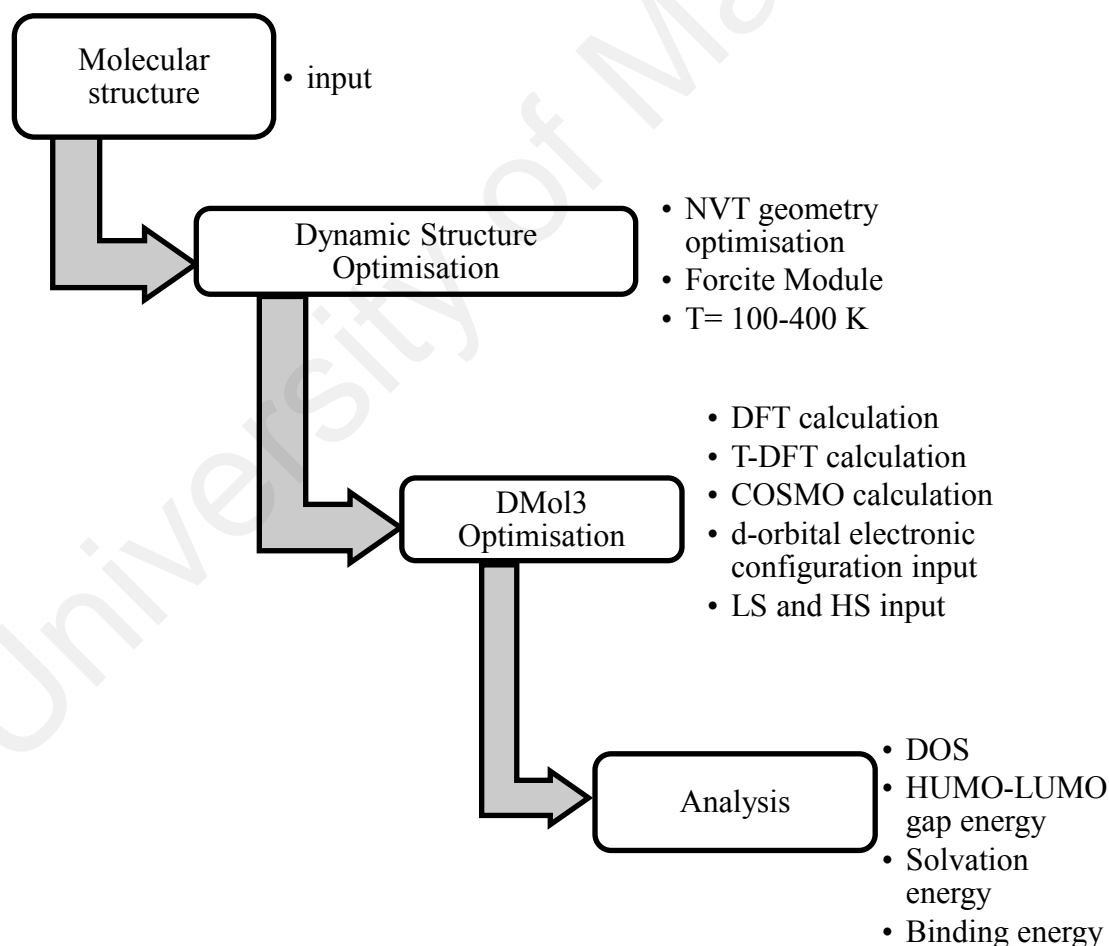


Figure 3.3. Simulation Steps

3.2.2.1 Geometry Optimization

Geometry optimizations of the complex dependent of temperature that been done using Dynamic NVT calculation (based on the use of a chain of M Nosé-Hoover thermostats) in Forcite module. The Forcite module enables thermodynamic optimization of the molecular structure ensemble for the complexes. The optimize geometry from the Forcite calculation, and then optimized in DMoL³ module based on density functional theory (DFT) calculation(Hohenberg & Kohn, 1964). The geometry optimization which based on electronic configuration of initial condition definition of d-orbital for the metal complexes will affect the molecular bond length and structure due to the electron repulsion force and electrostatic Vander walls forces. Investigations into $\Delta S_{reaction}$ based on Born's model mentioned in Chapter 2 for a range of transition-metal based redox couples in different ILs have shown a dependence of Z_{ox} and Z_{red} , r_{ox} and r_{red} on the charge, Z of the electro active species, suggesting a strong influence of electrostatic forces on the magnitude of $\Delta S_{reaction}$. The optimize geometry which represent by the average bond length of N-bond length with metal center is shown in Figure 3.4. For complex with valence charge 2+, the high N-metal average bond length expected for LS state expected to have high HUMO-LUMO gap energy. High HUMO-LUMO gap energy for the ion complex 2+ will be expected to reduce the ionic radius thus increases the entropy reaction and S_e . The molecular conformation of the ion complexes at different temperature dependency from geometry optimisation had given initial insight on how the physical molecular structure can affects the reaction entropy and Seebeck coefficient.

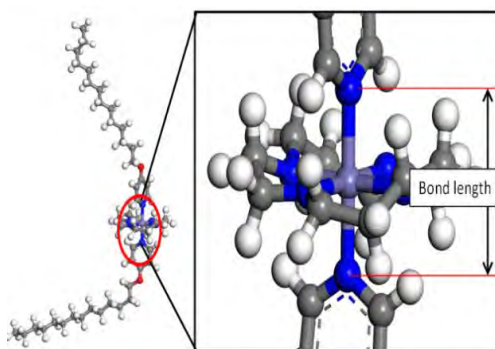


Figure 3.4. Metal to ligand interaction of octahedral structure

3.2.2.2 Dynamic NVT geometry optimizations

The step for modeling, geometry optimizations of the complex as a function of temperature were done using Dynamic NVT calculation (based on the use of a chain of M Nosé-Hoover thermostats) in Forcite module (Lv, Han, Zhang, et.al, 2019). This is to ensure the right molecule conformation is used for further simulation. In this calculation, the thermodynamic molecular structure ensemble for the complexes was identified.

3.2.2.3 DMol³ density of states calculation

The optimized geometry from the Forcite calculation, then optimised in DMol³ module based on density functional theory (DFT) calculation that allow geometry optimization based on electronic configuration initial condition definition of d-orbital for the metal complexes. The possibilities of the initial d-orbital configuration for the complexes are as shown in Figure 3.2. Using Figure 3.2, electronic configuration of d-orbital for the metal complexes was defined based on previous study of the complexes using Nuclear Magnetic Resonance analysis, H1-NMR at room temperature (M. M. I. M. Hasnan et al., 2018; Hussin, 2016). Interestingly, the solvation properties option on the DMol³ Analysis will also optimize molecular geometry based on solvent interaction with the complex molecule based on dielectric permittivity definition (46 and 36 for DMSO and MPN respectively). At this stage, the optimization process was an iterative procedure in which the coordinates of the atoms are adjusted so that the energy of the structure is

brought to a stationary point where the minimum energy of the molecular geometry was identified.

3.2.2.4 Electrochemical HUMO-LUMO Gap Energy Calculation at Room Temperature and dependent temperature (100-400 K)

At room temperature, the electrochemical HUMO-LUMO gap was calculated from the difference between energy of HOMO of ion 3+ with energy of LUMO of ion 2+ of the complex and compared with cyclic voltammetry analysis. From density of states (DOS) calculation using DMol³ geometry optimization, HUMO-LUMO gap energy change due to bond length changes dependent temperatures between metal to ligand interaction were investigated.

3.2.2.5 DMol³ Time-dependent Density Functional Theory (TD-DFT) Optic Spectrum Analysis

Electronic properties involved in DMol³ calculation were density of state (DOS) calculation and time-dependent density functional theory (TD-DFT) of the optical spectrum calculation (Raikawa, Sonigara, Patil et.al, 2019). From DMol³ optical spectrum, the maximum excitation energy at specific wavelength was calculated to investigate the frequency changes of the maximum excited energy dependent of temperature. The HUMO-LUMO gap energy results from the metal-ligand field strength dependent of temperature affect the magnitude and trend of the Seebeck coefficient and ionic conductivity. Maximum excitation energy that occurs at high frequency (low wave number) inferred to produce high ionic conductivity due to fast excitation relaxation. The lower difference in energy between two state of ¹T_{1g} and ¹T_{2g} inferred to give lower HUMO-LUMO gap energy that will lead to high Seebeck value.

The minimum excitation energy of electron for the SCO complexes having initial valence charge 2+ can be related to the minimum activation energy required for the complexes to oxidise from 2+ to 3+ valence state.

3.2.3 Synthesis of SCO material

SCO complexes were prepared (M. M. I. M. Hasnan et al., 2018; Hussin, 2016) as shown in Figure 3.5 and Figure 3.6. The structural formulae for these complexes were deduced from the combined elemental analyses for C, H and N, FTIR spectroscopy, UV-vis spectroscopy and thermogravimetric analysis. In order to understand the behavior of the SCO material, the proposed structures of three SCO complexes were synthesized and are explained briefly below. The syntheses steps for $[\text{Mn}(\text{cyclam})(\text{L14})_2](\text{R})_2 \cdot 4\text{H}_2\text{O}(\text{Mn})$, $[\text{Fe}(\text{cyclam})(\text{L14})_2](\text{R})_2 \cdot 2\text{H}_2\text{O}(\text{Fe})$, and $[\text{Co}(\text{cyclam})(\text{L14})_2](\text{R})_2 \cdot 3\text{H}_2\text{O}(\text{Co})$ are shown as Figure 3.5 and Figure 3.6.

3.2.3.1 Synthesis of $[\text{Mn}(\text{cyclam})(\text{L14})_2](\text{C}_6\text{H}_5\text{COO})_2 \cdot 4\text{H}_2\text{O}$

$\text{C}_6\text{H}_5\text{COONa}$ (5.00 g, 34.7 mmol) was dissolved in H_2O (50 mL) and magnetically stirred at room temperature for one hour. $\text{MnCl}_2 \cdot 6\text{H}_2\text{O}$ (3.44 g, 17.4 mmol) was then added portion wise to the aqueous suspension. The reaction mixture was further stirred for two hours, and then filtered. A white $[\text{Mn}(\text{C}_6\text{H}_5\text{COO})_2] \cdot \text{H}_2\text{O}$ powder was obtained, and its yield was 4.51 g (80.1 %). Next, a suspension of $[\text{Mn}(\text{C}_6\text{H}_5\text{COO})_2] \cdot \text{H}_2\text{O}$ (0.37 g, 1.1 mmol) in $\text{C}_2\text{H}_5\text{OH}$ (100 mL) was magnetically stirred and heated. A solution of cyclam (0.25 g, 1.3 mmol) in $\text{C}_2\text{H}_5\text{OH}$ (50 mL) was added portion wise to the magnetically stirred hot suspension. The reaction mixture was then further stirred and heated for one hour, and then filtered hot. $[\text{Mn}(\text{C}_6\text{H}_5\text{COO})_2(\text{cyclam})]$ was obtained as a brown semisolid, and its yield was 0.46 g (65.6 %). Finally a suspension of $[\text{Mn}(\text{C}_6\text{H}_5\text{COO})_2(\text{cyclam})]$ (0.41 g, 0.66 mmol) in $\text{C}_2\text{H}_5\text{OH}$ (50 mL) was magnetically stirred. A solution of L (0.48 g, 1.65 mmol) in CHCl_3 (20 mL) was added portion wise to

the magnetically stirred suspension. The reaction mixture was further stirred and heated for one hour, and filtered. A dark brown semi-solid Mn was obtained, and its yield was 0.69 g (90.4 %). Anal. calcd. for $C_{62}H_{108}MnN_6O_{10}$: C, 66.6; H, 9.4; N, 7.5. Found: C, 64.6; H, 9.5; N, 7.3%.

3.2.3.2 Synthesis of $[Fe(cyclam)(L14)_2](C_6H_5COO)_2 \cdot 2H_2O$

The procedure was the same as for Mn, but was performed in nitrogen. The reaction between $FeSO_4 \cdot 7H_2O$ (2.69 g, 9.7 mmol) and C_6H_5COONa (2.79 g, 19.4 mmol) produced the $[Fe_2(C_6H_5COO)_4] \cdot H_2O$ as a brown powder and its yield was 2.49 g (81.7 %). $[Fe(C_6H_5COO)_2(cyclam)] \cdot H_2O$ was obtained as a dark brown powder from the reaction between $[Fe_2(C_6H_5COO)_4] \cdot H_2O$ (0.38 g, 0.6 mmol) and cyclam (0.25 g, 1.3 mmol), and its yield was 0.60 g (88.3 %). Fe was obtained as a dark brown semi-solid from the reaction between $[Fe(C_6H_5COO)_2(cyclam)] \cdot H_2O$ (0.22 g, 0.4 mmol) and L (0.23 g, 0.8 mmol), and its yield was 0.34 g (76.1 %). Anal. calcd. for $C_{62}H_{104}FeN_6O_8$: C, 66.6; H, 9.4; N, 7.5. Found: C, 66.2; H, 9.8; N, 7.0%.

3.2.4 Synthesis of $[Co(cyclam)(L14)_2](C_6H_5COO)_2 \cdot 3H_2O$

The synthesis procedure was similar to the synthesis of Mn. The reaction between $CoCl_2 \cdot 6H_2O$ (4.13 g, 17.36 mmol) and C_6H_5COONa (5.00 g, 34.7 mmol) produced 5.15 g (54.6 %) $[Co_2(C_6H_5COO)_3Cl] \cdot H_2O$ as a purple powder. $[Co(C_6H_5COO)_2(cyclam)]$ was obtained as a dark brown semi-solid from the reaction between $[Co_2(C_6H_5COO)_3Cl] \cdot H_2O$ (0.38 g, 0.70 mmol) and cyclam (0.25 g, 1.25 mmol), and its yield was 0.56 g (79.8 %). Co was obtained as a dark brown semi-solid from the reaction between $[Co(C_6H_5COO)_2(cyclam)]$ (0.55 g, 1.1 mmol) and L (0.64 g, 2.2 mmol), and its yield was 0.99 g (79.2 %). Anal. calcd. for $C_{62}H_{106}CoN_6O_9$: C, 65.4; H, 9.4; N, 7.4. Found: C, 65.7; H, 9.3; N, 6.9%.

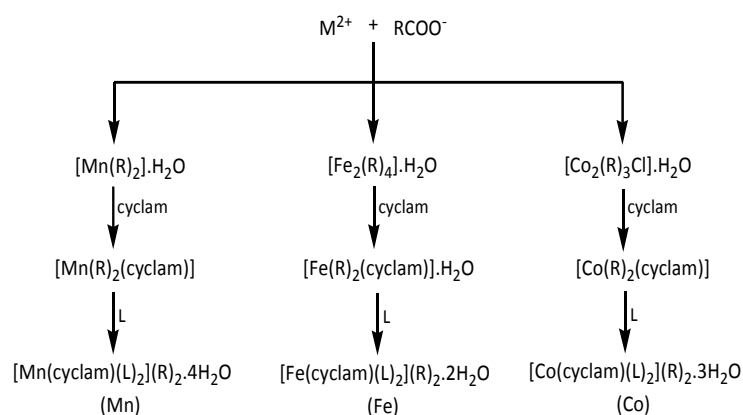


Figure 3.5. Schematic of metal complex synthesis process

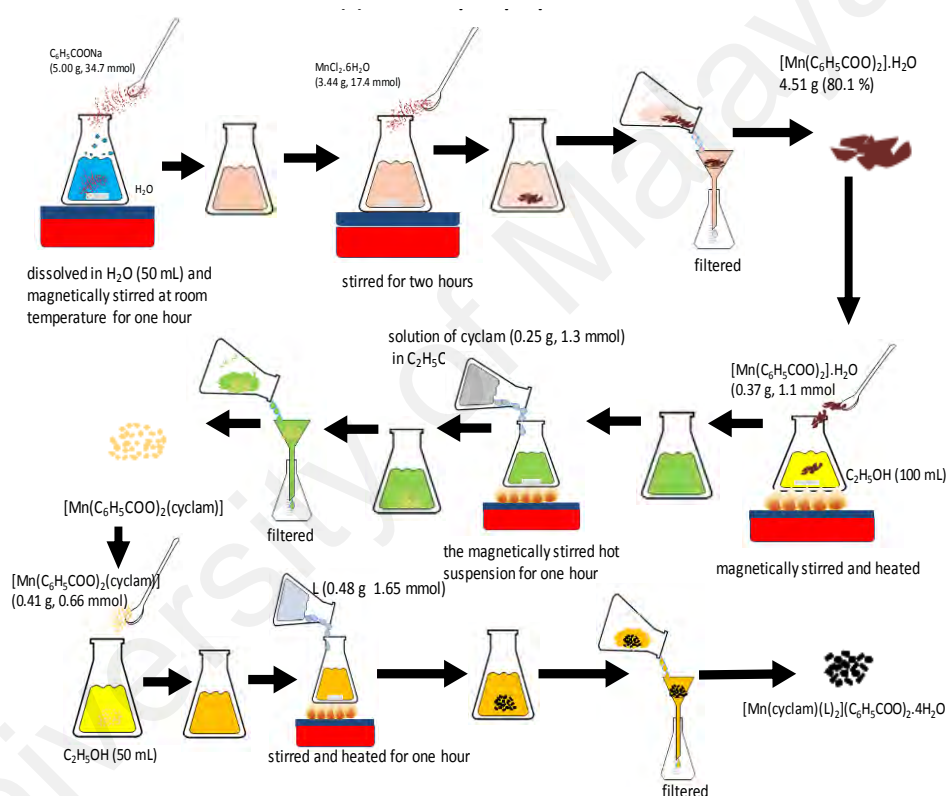


Figure 3.6. Example of Mn complex synthesis steps

After all the transition metals complexes were obtained, the complexes (1 mM) were mixed with tetra-*n*-butylammonium tetrafluoroborate (TBATFB; 0.3 M) as the supporting electrolyte. The Fe complex was dissolved in DMSO and MPN solvents due to the solubility in both solvent, whilst Mn and Co was able to dissolve in DMSO. Both solvent also was used due to higher boiling point than water. We found agglomeration of Fe complex in MPN solvent compared to clear solution of the others complex in DMSO

solvent. The solutions (1mM) were prepared for Seebeck and CV measurement in order to determine the electrochemical properties, as listed in Table 3.1.

Table 3.1. TEC material prepared

No	Material	Solvent	Supporting Electrolyte
1.	Fe(II)	DMSO	TBATFB
2	Fe(II)	MPN	TBATFB
3.	Mn(II)	DMSO	TBATFB
4.	Co(II)	DMSO	TBATFB

3.2.5 Structural Analysis

Elemental analyses were performed using the Thermo-Finnigan Flash analyser (EA 110 CHNS/O). The Fourier transform infrared (FTIR) spectra were recorded in the range from 4000 cm^{-1} to 450 cm^{-1} on a Perkin-Elmer Frontier spectrophotometer equipped with a diamond attenuated total reflectance. The UV-vis spectra were recorded in solution in the range from 1200 to 400 nm on a Shimadzu UV-vis-NIR 3600 spectrophotometer. Thermogravimetry (TG) was performed under N_2 on a Perkin-Elmer Pyris Diamond TG/DTA thermal instrument. The flow rate was 10 $\text{cm}^3\text{min}^{-1}$, the temperature range was 50 - 900 $^\circ\text{C}$, and the scan rate was 20 $^\circ\text{Cmin}^{-1}$.

3.2.6 Cyclic voltammetry analysis

Cyclic voltammetry is powerful technique in determination of electrochemical properties. The method of determination Seebeck using electrochemical method based on temperature dependent cyclic voltammetry (CV) analysis was previously reported. The Seebeck extraction from gradient of the half wave potential calculated from CV analysis at dependent temperatures was validated with non-isothermal cell measurement. From CV analysis, redox potential and reversibility of the TEC material can be confirmed for energy harvesting. CV measurement was done using a Gamry Potentiostat/Galvanostat 600 instrument at 300-355 K, in order to confirm the redox reaction in the sample. A standard three-electrode set-up (platinum working electrode, platinum wire reference

electrode, and platinum wire counter electrode) was used as shown in Figure 3.8. The solution was bubbled with nitrogen gas, (N₂) prior to each scan. The scan rate was 50 mVs⁻¹ and electrode potential values E(V) were the quoted versus Platinum. To make sure all the redox potential acquire from CV analysis were precisely detected using self-custom LAB view program to process experimental cyclic voltammetry data based on first order differential method to identify maximum and minimum redox peak as shown in Figure 3.7. The redox peak point is identified by intersect voltage with half point of the maximum and minimum of first order differential data point.

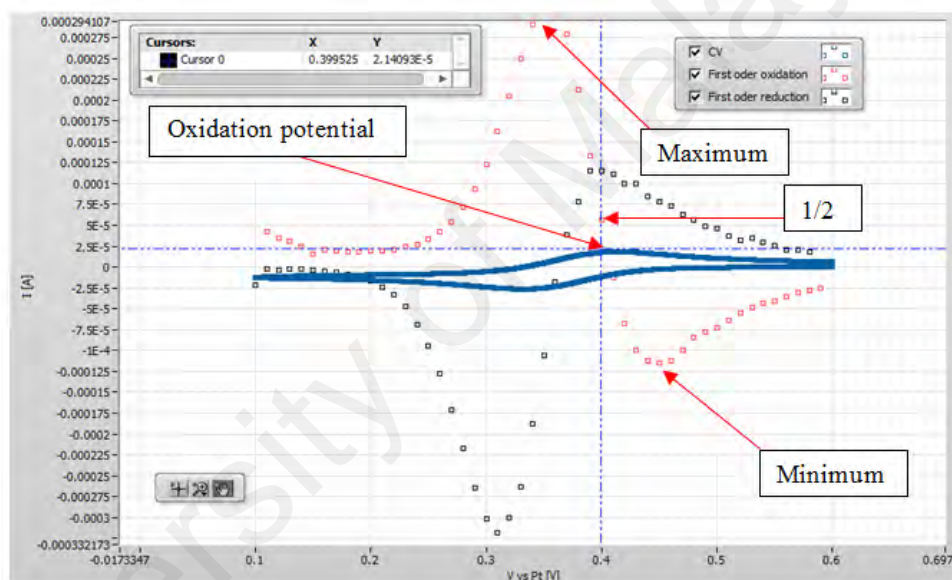


Figure 3.7. Redox potential determination using LAB VIEW

Ionic diffusion is a measure of the rate of charge transfer in solution and is indicative of the molecular structure of the respective metal complex. The diffusion coefficients (*D*) for sample, were calculated using the following Randles-Sevcik equation

$$i_p = 0.4463nFAc \left(\frac{nFD}{RT} \right)^{1/2} v^{1/2} \quad (68)$$

where *i_p* is limitation current peak, *n* is number of electron, *A* is electrode area, *c* is redox concentration, *v* is scan rate and *D* is diffusion coefficient.

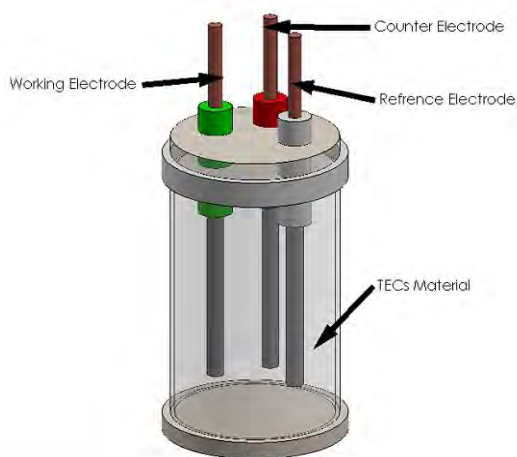


Figure 3.8. CV measurement setup

From the Nernst-Einstein relation it is known that the ionic mobility is proportional to the diffusion coefficient as shown in the following equation:

$$\mu = \frac{eD}{K_b T} \quad (69)$$

where e is electron charge, T is temperature, K_b is Boltzmann constant and D is diffusion coefficient. The ionic mobility can elucidate the molecular distortion relation to the mass transport behavior.

3.2.7 Electrical conductivity measurement

Ionic conductivity (σ) was obtained from the measured molar conductivity and measured directly by the multiparameter analyzer (DZS-708) as shown in Figure 3.9 at various temperatures 27-70 °C. The formula used to calculate σ from the measured molar conductivity is $\sigma = (\Lambda_m c)/1000$, where c is the molarity of electrolyte (1 mM) and Λ_m is the molar conductance.



Figure 3.9. Conductivity measurement setup

3.2.8 Seebeck and power measurement of non-isothermal cell

The S_e and power measurements setup used in this study is similar to previous investigation (Siddique, Balamurugan, Said, Sairi, & Normazlan, 2016) using a digital multimeter (Agilent 34461A) and resistor box with resistance range 1 K-10 M Ω , as shown in Figure 3.10. The samples were filled into a cell made up of two compartments, each containing a Pt wire electrode pre cleaned with diluted HCl followed by distilled water and a thermocouple used as temperature probe. The compartments were then placed inside two separate water baths and connected by a short salt bridge containing the same solution. One water bath was heated with a hot plate (hot side), while the other was left at room temperature (cold side). The ΔV between Pt electrode (area = 0.32 cm²) at the hot side and the cold side was measured in steady state condition at 5 °C intervals, for a temperature range of 25 - 75 °C, using a digital multimeter (Agilent 34461A). The temperature were confirm for every reading using thermocouple type-K that measured the temperature of the solution at both cold side and hot side. The S_e was determined from the gradient of the linear relation of the ΔV and ΔT plot, and all measurements were measured in 3 cycles.

The maximum electrical power is obtain if the internal load is equal to external load (Gunawan et al., 2013). After measuring the S_e , the compartments were maintained at temperature gradient and connected to an external load. Individual resistances (R, Ω)

were applied and the corresponding cell potentials were recorded. The power outputs were calculated using Ohm's law ($P = V^2/R$) (Hasan et al., 2016).

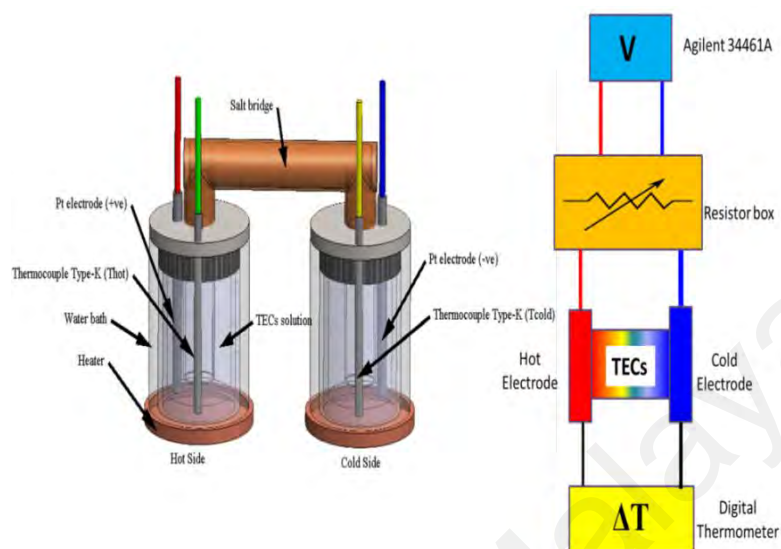


Figure 3.10. Seebeck and power measurement setup

3.3 Results and discussion

3.3.1 Molecular modeling

3.3.1.1 Geometry optimisation

The thermodynamic molecular structure ensemble for the complexes was identified. The optimized geometry from the Forcite calculation was then optimized using the DMoL³ module, to yield the most stable molecular configurations of the HS and LS states as a function of temperature, from 303 K to 343 K at intervals of 10 K. The molecular bond length of metal to ligand interaction as shown in Figure 3.11, Figure 3.12 and Figure 3.13, will ultimately affect the Seebeck coefficient, given the changes in entropy during the spin transition.

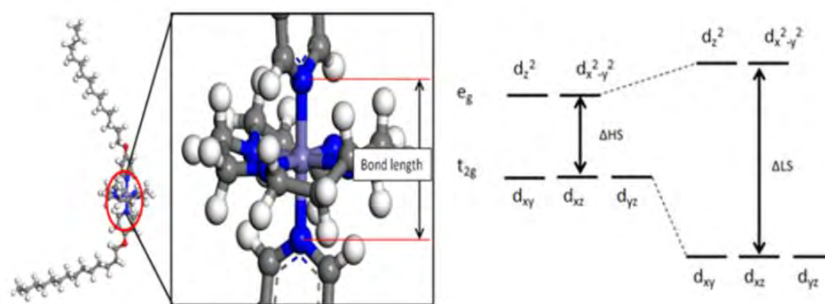


Figure 3.11. Molecular bond length of metal to ligand interaction induce high entropy different between spin state transition

Based on an initial electronic configuration, the possible initial d-orbital configurations for the ionic complex were defined as previously proposed based on experimental H1-NMR studies. The molecular structure of the metal complex was optimized using Dynamic NVT calculation as a function of temperature (303-343 K). The effect of the molecular distortion observed by taking the average of the bond length between the metal center and six nitrogen atoms surrounded as shown in Figure 3.12. Fe^{2+} ion in MPN solvent was shown to have the lowest average metal-nitrogen bond length compared to the other as expected for high stability of LS state compared to Fe^{2+} , Co^{2+} and Mn^{2+} in DMSO which has a higher average metal-nitrogen atom bond length for higher HS state possibility. The effect of the metal to the ligand interaction to the DOS and HOMO-LUMO gap energy was investigated by using the optimized geometry as input for DMol³ optimisation as explained in the next section.

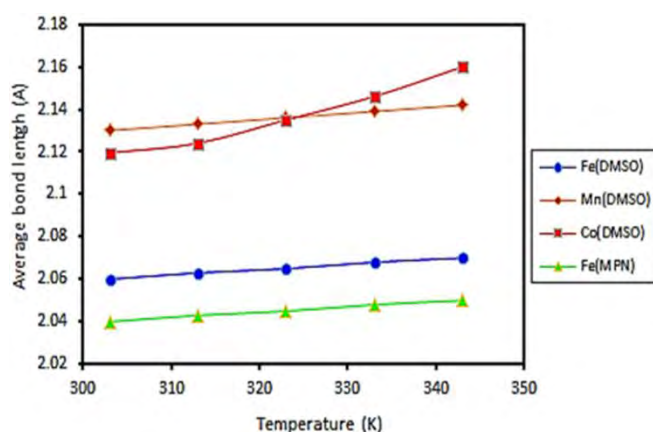


Figure 3.12. Average of bond length between the metal center and the six nitrogen atom

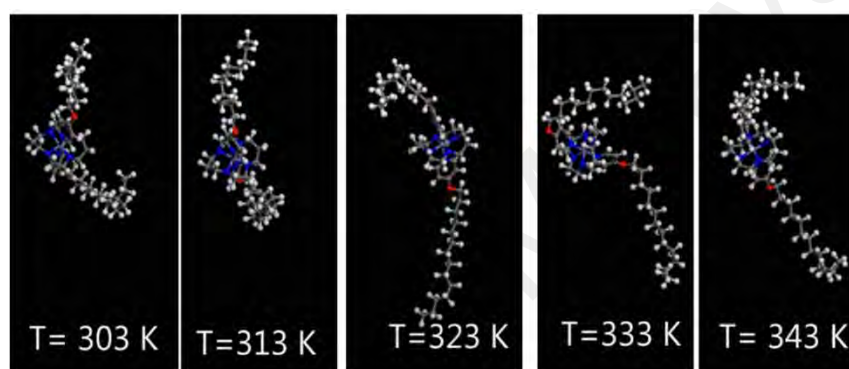


Figure 3.13. Optimize geometry of Fe(II) complex at temperature dependent

3.3.1.2 Density of states (DOS) calculation

Next, DMol³ module in Material Studio was used to calculate HUMO-LUMO gap energy of the complexes from density of states calculation as shown in Figure 3.14. DOS is needed to identify highest occupied molecular orbital HOMO energy and lowest occupied molecular orbital LUMO energy. At single molecular level of the complexes, the HUMO-LUMO gap, solvation energy and binding energy had been calculated for each HS state and LS state for oxidation state (3+) and reduction state (2+). The conductivity of a solution depends on the solvation of its ions. Solvation properties definition included in the DMol³ analysis also optimize molecular geometry based on solvent interaction with the complex molecule based on the respective value of the solvent dielectric permittivity definition (46 and 36 for DMSO and MPN respectively). At this stage, the optimization process was an iterative procedure in which the coordinates of the

atoms are adjusted so that the energy of the structure is brought to a stationary point where the minimum energy of the molecular geometry was identified. Electronic properties involved in DMoL³ calculation were density of state (DOS) calculation and time-dependent density functional theory (TD-DFT) of optic spectrum calculation. Based on density of state calculation, HUMO-LUMO gap energy was calculated from DOS while from optical spectrum, the maximum excitation energy at specific wavelength were calculated to investigate the frequency changes of the maximum excited energy dependent of temperature.

The minimum total energy selected for both LS/HS determination of the ion complex initial state condition as shown as grey highlighted in the Table 3.2. The result showed the spin state possibility of the complexes at room temperature were HS for Mn(II), Mn(III), Co(II), Fe(II) in DMSO and LS for Fe(II) in MPN, Co(III), Fe(III) in DMSO and Fe(III) in MPN respectively for octahedral complex using L14 as highlight in the Table 3.2. Fe in MPN also shown the highest solvation energy compared to the other complexes. The conductivity depends on solvation of the ion hence Fe in MPN expected to have high conductivity. This show the solvation energy is sensitive to the molecular charge and radius(Wang & Wong, 2006) that may also affect the Seebeck generation for the total system in TEC.

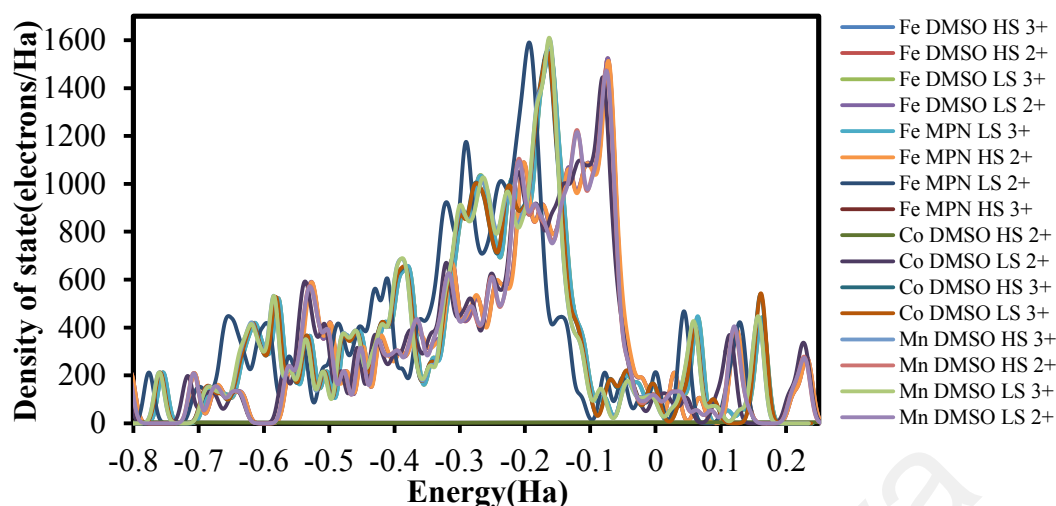


Figure 3.14. Density state calculation of LS/HS state of SCO complexes

Table 3.2. Simulation results of molecular modeling studies

Metal 2+ (Low Spin)	Total Energy (Ha)	Solvation Energy (kcal/mol)	Homo (eV)	Lumo (eV)	HUMO-LUMO Gap (eV)	Binding Energy (Ha)
Mn+DMSO	-3508.224923	-130.60	-5.584	-5.226	0.358	-23.163994
Co+DMSO	-3739.96528	-130.23	-5.44	-5.058	0.382	-23.1904793
Fe+DMSO	-3620.930951	-130.33	-5.681	-4.924	0.757	-23.1956902
Fe+MPN	-3620.928953	-128.95	-5.733	-4.977	0.756	-23.1936914
Metal 2+ (High Spin)	Total Energy (Ha)	Solvation Energy (kcal/mol)	Homo (eV)	Lumo (eV)	HUMO-LUMO Gap (eV)	Binding Energy (Ha)
Mn+DMSO	-3508.225596	-130.73	-5.579	-5.196	0.383	-23.1646608
Co+DMSO	-3739.965497	-130.34	-5.432	-5.041	0.391	-23.190689
Fe+DMSO	-3620.930946	-130.35	-5.678	-4.924	0.754	-23.1956849
Fe+MPN	-3620.928954	-128.95	-5.733	-4.976	0.757	-23.1936914
Metal 3+ (Low Spin)	Total Energy (Ha)	Solvation Energy (kcal/mol)	Homo (eV)	Lumo (eV)	HUMO-LUMO Gap (eV)	Binding Energy (Ha)
Mn+DMSO	-3508.518545	-11.41	-3.167	-2.487	0.68	-23.4558
Co+DMSO	-3740.275428	-11.14	-3.153	-2.16	0.993	-23.4958
Fe+DMSO	-3621.22934	-11.21	-3.321	-2.358	0.963	-23.4927
Fe+MPN	-3621.229085	-11.10	-3.312	-2.341	0.971	-23.4938
Metal 3+ (High Spin)	Total Energy (Ha)	Solvation Energy (kcal/mol)	Homo (eV)	Lumo (eV)	HUMO-LUMO Gap (eV)	Binding Energy (Ha)
Mn+DMSO	-3508.51938	-11.79	-3.171	-2.509	0.662	-23.4585
Co+DMSO	-3740.275504	-11.21	-3.158	-2.166	0.992	-23.4958
Fe+DMSO	-3621.229538	-11.26	-3.317	-2.349	0.968	-23.4929
Fe+MPN	-3621.229077	-11.08	-3.317	-2.346	0.971	-23.4938

Figure 3.15 show energy different calculation using DMol³ module using Material Studio BIOVIA simulation tools based on molecular modeling of the complexes for transition (HS-LS) state at room temperature. The Fe complex show the highest minimum

energy difference followed by Co complex and Mn complex. This indicate the higher possibilities of the Fe complexes to be more stable in the presence low spin state compared to the other Co and Mn complexes which required more less energy to have spin transition from low spin to the high spin.

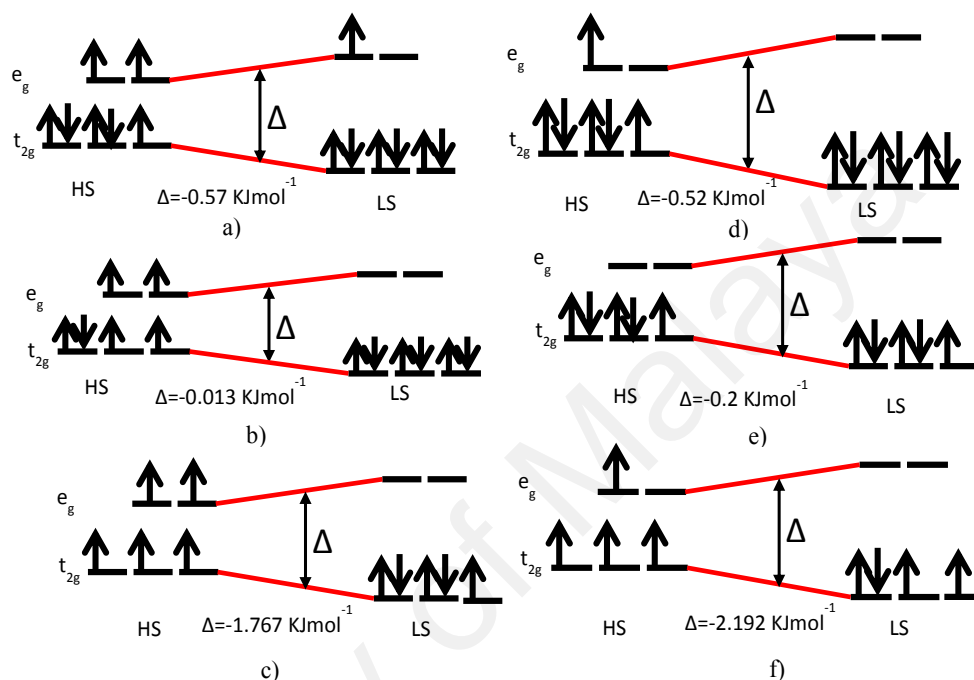


Figure 3.15. Energy different calculation of the complexes for spin state transition of a) Co^{2+} b) Fe^{2+} c) Mn^{2+} d) Co^{3+} e) Fe^{3+} and f) Mn^{3+}

3.3.1.3 Electrochemical HUMO-LUMO gap energy

Redox reaction in TEC depended on electrochemical HUMO-LUMO gap energy state of oxidation state and reduction state of the charge carrier. For high Se, complexes inferred to be as low as possible. Refer to Figure 3.17, electrochemical HUMO-LUMO gap had been calculated from difference energy gap of LUMO of product metal²⁺ to HOMO reactant metal³⁺ at room temperature and showed HUMO-LUMO gap energy of 2.025, 1.88 and 1.603 eV for Mn, Co and Fe respectively. In term of increase of ease of the complex to pursue redox reaction in solvent, the trend was $\text{Fe} > \text{Mn} > \text{Co}$ at room temperature 303 K. The electrochemical HUMO-LUMO gap obtained from cyclic voltammetry measurement (1.464, 1.139, 1.105/0.947 eV for Mn, Co, Fe(DMSO/MPN))

respectively) showed the same trend with electrochemical HUMO-LUMO gap obtained from modeling but slightly different in value because supporting electrolyte TBATFB not defined in the calculation which out of scope of this study. We inferred that the polarity and interaction of the TBATFB with the ionic complexes can reduce the HUMO-LUMO gap energy of the total system.

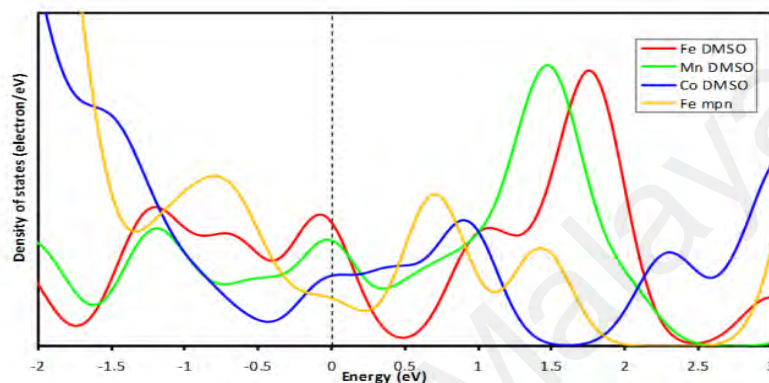


Figure 3.16. Density of state of d-orbital for complexes 2+

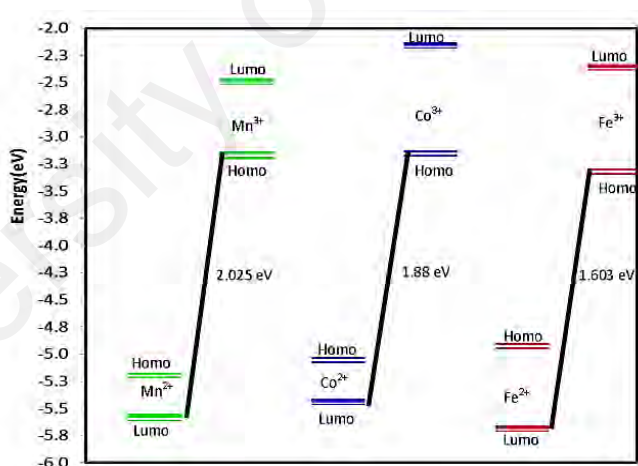


Figure 3.17. Electrochemical HOMO-LUMO gap calculation from DOS

Figure 3.18 shows HOMO-LUMO gap energy calculation of complexes metal 2+ from density of states (DOS) calculation using DMol³ geometry optimization. The HOMO-LUMO gap energy was changes due to bond length changes as function of temperatures as expected (refer to Figure 3.4) between metal to ligand interaction as shown in Figure 3.18. Mn complex show parabolic trend of HOMO-LUMO gap energy at dependent

temperature. The minimum HOMO-LUMO gap energy for Mn was between temperatures 200-300 K. All complexes showed increasing of HOMO-LUMO gap energy after temperature 300 K, indicating for stable LS state of the complexes. The electrochemical HOMO-LUMO gap relation to the S_e generation will be investigated by comparing electrochemical HOMO-LUMO gap extraction using experimental CV analysis and experimental S_e measurement.

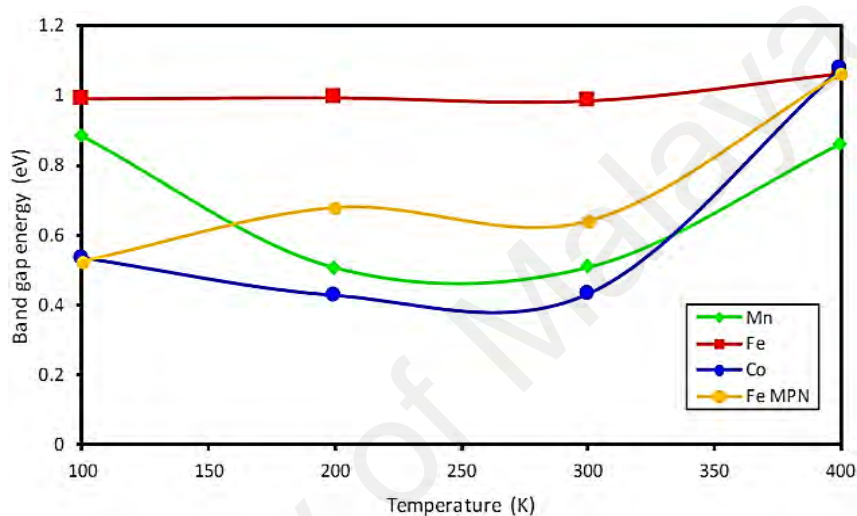


Figure 3.18. HOMO-LUMO gap energy of complexes 2+

3.3.1.4 Optic Spectrum Analysis using DMOL³

By calculating the excitation energies with TD-DFT at variation temperature, the excitation spectra for each complex can be obtained. Figure 3.19 show some of the excited state of the complexes at room temperature. DMol³ enables the electronic states of the final optimize structure to be calculated. The optical analysis in the DMol³ analysis allows optical (UV-Vis) spectra generated. Excitation energy corresponds to the photon absorption energy of the molecule in its initial state which can be related to the metal to ligand (M-L) field strength. The key parameters for studying the phenomenon of absorption are the extinction coefficient and the oscillator strength as shown in Figure 3.20. The small values of oscillator strength at maximum excitation energy for the complexes are due to the assigned d-d band formation and ligand field transition from

interaction between metal and ligand. The d-d bands are assigned to the electronic transitions for metal²⁺ centers, consistent with strong M²⁺-N bonds: ²T_{1g} to ²A_{2g} and ²T_{1g} for Mn, ¹A_{1g} to ¹T_{1g} and ¹T_{2g} for Fe, and ²E_g to ²T_{1g}(P) and ²T_{2g} for Co.

The difference in frequency between peaks ¹T_{1g} and ¹T_{2g} can be related to relaxation of excitation of electron to the higher state, while the difference between the maximum excitation energy observed for peaks ¹T_{1g} and ¹T_{2g} can be related to the different energy level between the two states and ligand splitting energy. The distortion of the long alkyl chain ligand affected by temperature expected to switch the metal-ligand field strength that stimulus spin state transition from HS to LS. The distortion of the ligand which results from changes of metal to ligand bonding can affect the metal spin centers, including redox-induced spin-state switching and charge-transfer induced spin-state changes.

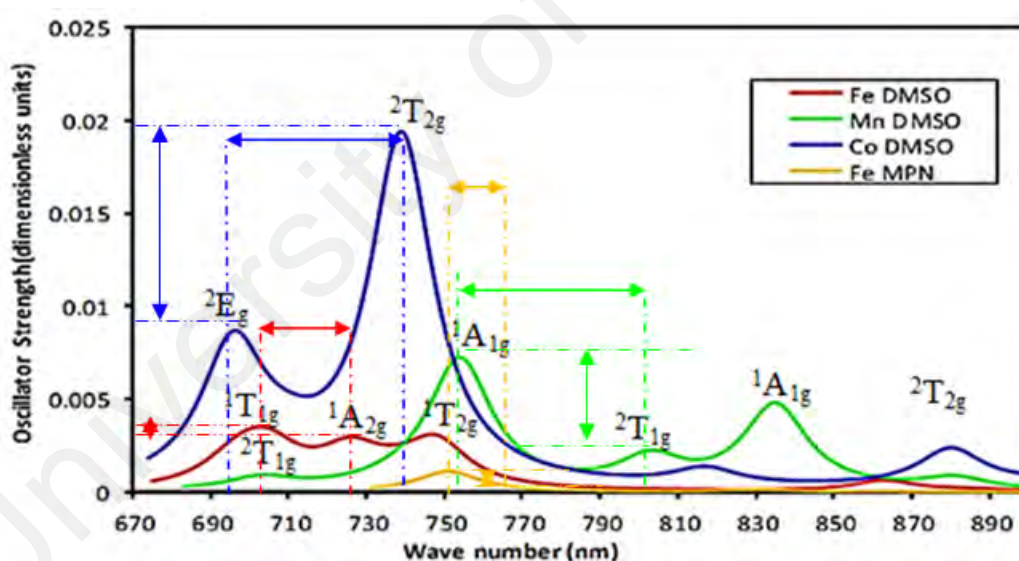


Figure 3.19. Excitation energy calculation of ionic SCO complex ligand 14 at room temperature

From the structural point of view, for Fe, at T= 200-300 K the small energy difference (weak ligand field strength) leads to the overlap of the two peaks assigned for excitation energy of ¹T_{1g} and ¹T_{2g}, which explains the broad peak observed in the visible spectrum and HS state at T=100-300 K as shown in Figure 3.20 . But for strong ligand field strength for Fe at T= 400 K, an optical intensity show sharp peak was assigned for ¹T_{2g} and LS of

Fe. The transition of weak ligand field strength to strong ligand field strength shows a transition of HS to LS across the temperature. The oxidation reaction needed is as low energy as possible to excite electron from ground state to higher state where in HS state the different energy level between ${}^1T_{1g}$ and ${}^1T_{2g}$ was the minimum for Fe compared to the LS state.

Compared to Fe in MPN as shown in Figure 3.20, the maximum excitation energy is increasing with increasing temperature from 300 K to 400 K while the frequency of the maximum excitation energy were shifting from lower frequency(750 nm) to higher frequency(700 nm). The transition from lower to high maximum excitation energy shown that the possibilities of the complex having transition of small to large splitting energy between ${}^1T_{1g}$ and ${}^1T_{2g}$ energy level due to HS to LS state transition of the Fe complex in MPN.

For the Mn complex, drastic changes of frequency of maximum excitation energy from higher to lower frequency (750 to 870 nm) for temperature 300 to 400 K due to transition of weak field strength to high field strength with increasing temperature. The activation energy to pursue redox reaction for Mn LS complex is expected to be higher compared to the HS state which resulting in a decrease in Seebeck magnitude at higher temperature.

For the Co complex, the frequency of the maximum excitation energy was shifted slightly from 730 nm to 784 nm for transition temperature $T=300$ K to $T=400$ K. The sharp and increasing intensity of optical intensity showing increasing excitation energy at $T=400$ K with increasing temperature resulting from high ligand field strength thus produce high conductivity magnitude.

We inferred that the best optimum conditions of FeL14 complexes for high conductivity was the complex in HS state, having a small different of the excitation

energy level of ${}^1T_{1g}$ and ${}^1T_{2g}$ and the excitation energy of ${}^1T_{1g}$ and ${}^1T_{2g}$ excite at small wave number (higher frequency). The best optimum condition of SCO complexes for TEC is where at hot electrode the complexes are in HS state while at cold electrode the complexes are in LS state based on the possibilities of the SCO complexes be redox-induced spin-state switching which can lead to increase entropy reaction.

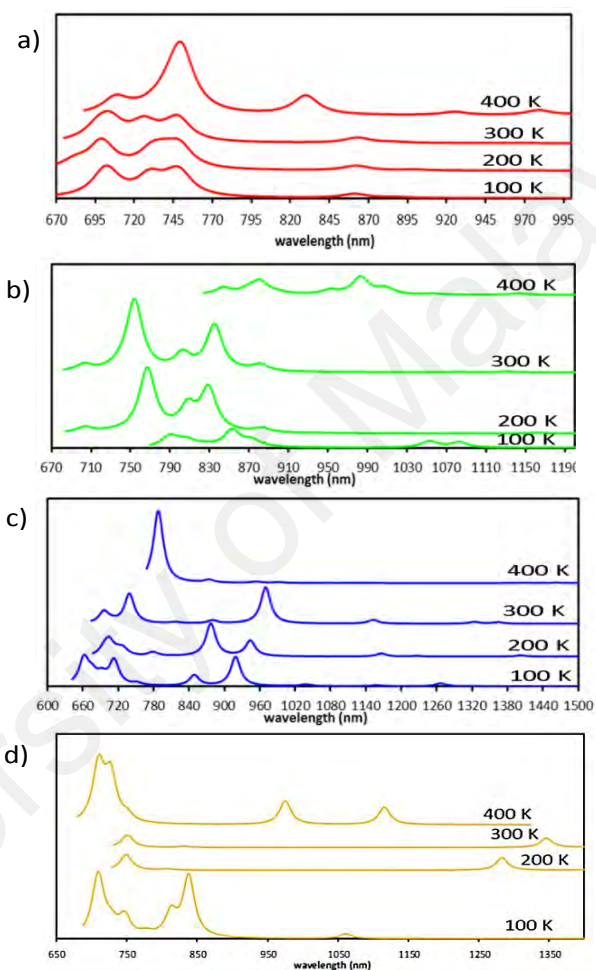


Figure 3.20. Excitation energy trend of the complexes at dependent temperature a)Fe(DMSO) b)Mn(DMSO) c)Co(DMSO) and d)Fe(MPN)

3.3.2 Structural analysis

The structural formulae for these complexes were deduced from the combined elemental analyses for C, H and N, FTIR spectroscopy, UV-vis spectroscopy and thermogravimetric analysis. These data are summarised in Table 3.3. The FTIR spectra for Co, Fe and Mn as shown in Figure 3.21 showed two strong peaks at about 2922- 2930

cm^{-1} ($\nu_{\text{asym}}\text{CH}_2$) and $2853\text{-}2860\text{ cm}^{-1}$ ($\nu_{\text{sym}}\text{CH}_2$) for ligand L, and at about $1555\text{-}1560\text{ cm}^{-1}$ ($\nu_{\text{asym}}\text{COO}$) and $1353\text{-}1380\text{ cm}^{-1}$ ($\nu_{\text{sym}}\text{COO}$) for $\text{C}_6\text{H}_5\text{COO}^-$ ion. The Δ values ($\Delta_{\text{COO}} = \nu_{\text{asym}}\text{COO} - \nu_{\text{sym}}\text{COO}$) were 183 cm^{-1} for Mn, 179 cm^{-1} for Fe and 207 cm^{-1} for Co. These values were higher than the expected value of 160 cm^{-1} for free $\text{C}_6\text{H}_5\text{COO}^-$ ion, suggesting that the anion was hydrogen-bonded to the lattice of H_2O and/or cyclam.

The UV-vis spectra of these complexes in CHCl_3 showed strong charge transfer bands with d-d bands as shoulders at about 347 nm, 454 nm and 654 nm, respectively. The d-d bands are assigned to the electronic transitions for low spin (LS) metal²⁺ centres, consistent with strong M²⁺-N bonds: ${}^2\text{T}_{1g}$ to ${}^2\text{A}_{2g}$ and ${}^2\text{T}_{1g}$ for Mn, ${}^1\text{A}_{1g}$ to ${}^1\text{T}_{1g}$ and ${}^1\text{T}_{2g}$ for Fe, and ${}^2\text{E}_g$ to ${}^2\text{T}_{1g}(\text{P})$ and ${}^2\text{T}_{2g}$ for Co. Moreover, from the thermogravimetric analysis, (TG) data, it is found that the measured percentage mass losses of these samples are in good agreement with the calculated results from their chemical formulae. These results indicate high purity and support their proposed structural formulae. Their decomposition temperatures were $130\text{ }^\circ\text{C}$, $150\text{ }^\circ\text{C}$ and $156\text{ }^\circ\text{C}$ for Mn, Fe and Co, respectively.

The magnetic states of the complexes were inferred from the ${}^1\text{H-NMR}$ Spectra. The ${}^1\text{H-NMR}$ spectra for Mn and Co in solutions at room temperature did not show any peaks, whilst the spectrum for Fe showed sharp peaks for the organic ligands only. Hence, it was inferred that Mn^{2+} and Co^{2+} were paramagnetic complexes (HS/LS) and Fe^{2+} was a diamagnetic (High percentage of LS) complex at room temperature.

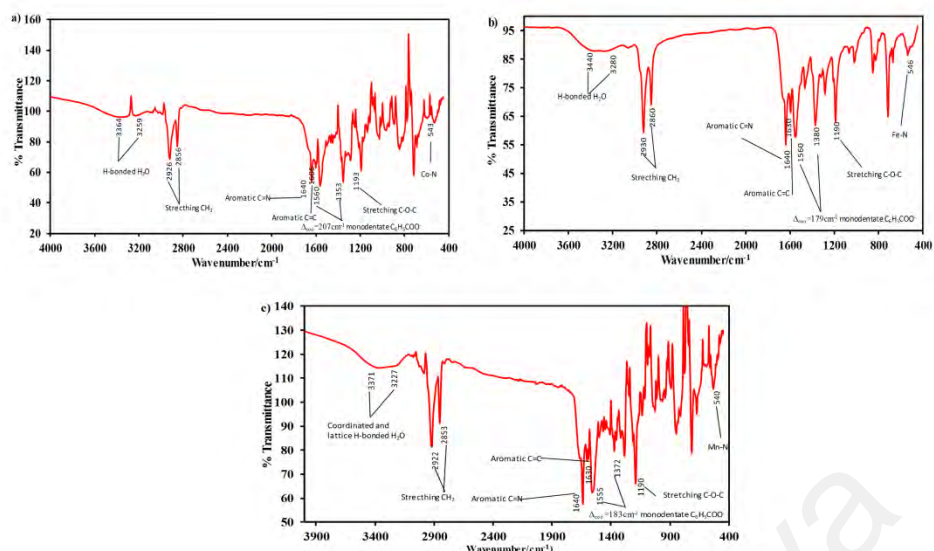


Figure 3.21. FTIR spectrum of a) Co b) Fe and c) Mn complexes

Table 3.3. Spectral (FTIR and UV-vis) and thermogravimetric data for metal complexes

Complex	FTIR $\Delta_{\text{COO}}(\text{cm}^{-1})$	UV-vis $\lambda_{\text{max}}(\text{nm})$ $\epsilon_{\text{max}}(10^2 \text{ M}^{-1} \text{ cm}^{-1})$	T ($^{\circ}\text{C}$)	Thermogravimetry	
				Mass loss (%) Found (Calc.)	Assignment
$[\text{Mn}(\text{cyclam})(\text{L})_2](\text{C}_6\text{H}_5\text{COO})_2 \cdot 4\text{H}_2\text{O}$ (Mn)	183	347 sh (1.1)	80–130 130–680	2.9 (3.2) 89.7 (91.8)	$4\text{H}_2\text{O}$ 2 L, cyclam, $2\text{C}_6\text{H}_5\text{COO}^-$
$[\text{Fe}(\text{cyclam})(\text{L})_2](\text{C}_6\text{H}_5\text{COO})_2 \cdot 2\text{H}_2\text{O}$ (Fe)	179	454 sh (4.8)	56–150 150–693	4.0 (3.2) 92.4 (91.8)	$2\text{H}_2\text{O}$ 2 L, cyclam, $2\text{C}_6\text{H}_5\text{COO}^-$
$[\text{Co}(\text{cyclam})(\text{L})_2](\text{C}_6\text{H}_5\text{COO})_2 \cdot 3\text{H}_2\text{O}$ (Co)	207	654 sh (7.3)	70–156 156–694	5.0 (4.7) 89.0 (90.1)	$3\text{H}_2\text{O}$ 2 L, cyclam, $2\text{C}_6\text{H}_5\text{COO}^-$

3.3.3 Cyclic Voltammetry analysis

From the experimental cyclic voltammetry analysis shown in Figure 3.22, parameters that were investigated are anodic potential, (E_a), cathodic potential, (E_c), electrode formal potential (E_f), oxidation limitation current peak, (I_{fp}) and reduction limitation current peak, (I_{rp}) as summarized in Table 3.5. Based on redox potential peak, reaction equilibrium at hot side and cold side were deduced to determine reaction quotient, (Q_{hot} and Q_{cold}) as a function of concentration ratio of redox species involves as summarised in Table 3.4. The analysis of electrochemical band gap and diffusion coefficient analysis from CV at room temperature as summarized in Table 3.6.

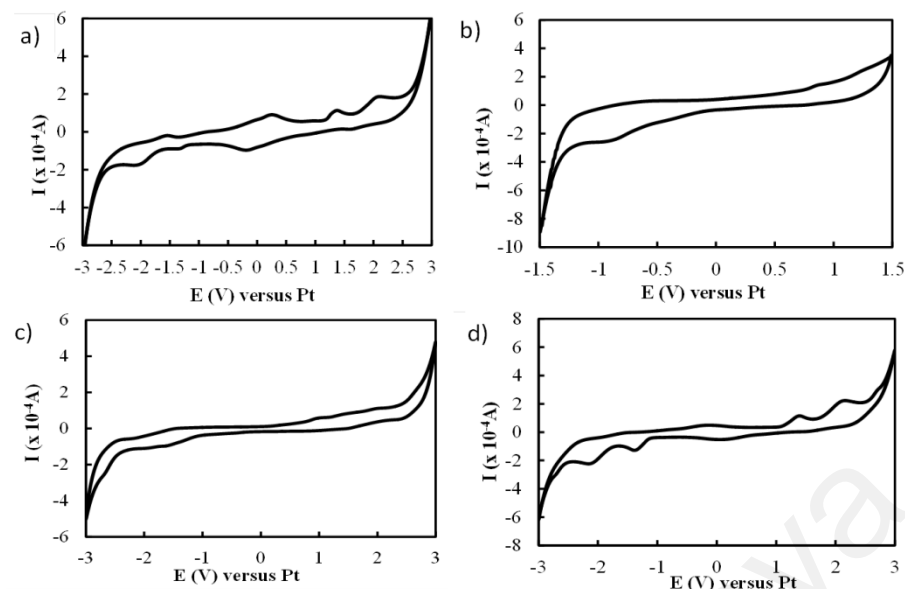


Figure 3.22. Cyclic voltammety characteristic of TEC materials at room temperature for a) Fe(II) in DMSO b) Fe(II) in MPN c) Co(II) in DMSO and d) Mn(II) in DMSO

Table 3.4. Reaction proposed

No	Material	Reaction Equilibrium	Reaction Quotient
1.	Fe(II)+MPN+TBATFB	$[Fe(cyclam)(L)_2]^{2+} \leftrightarrow [Fe(cyclam)(L)_2]^{3+}$	$Q = \frac{[Fe(cyclam)(L)_2]^{3+}}{[Fe(cyclam)(L)_2]^{2+}}$
2	Fe(II)+DMSO+TBATFB	$[Fe(cyclam)(L)_2]^{2+} \leftrightarrow [Fe(cyclam)(L)_2]^{3+}$	$Q = \frac{[Fe(cyclam)(L)_2]^{3+}}{[Fe(cyclam)(L)_2]^{2+}}$
3.	Co(II)+DMSO+TBATFB	$[Co(cyclam)(L)_2]^{2+} \leftrightarrow [Co(cyclam)(L)_2]^{3+}$	$Q = \frac{[Co(cyclam)(L)_2]^{3+}}{[Co(cyclam)(L)_2]^{2+}}$
4.	Mn(II)+DMSO+TBATFB	$[Mn(cyclam)(L)_2]^{2+} \leftrightarrow [Mn(cyclam)(L)_2]^{3+}$	$Q = \frac{[Mn(cyclam)(L)_2]^{3+}}{[Mn(cyclam)(L)_2]^{2+}}$

Table 3.5. CV analysis

No	Material	$E_a(V)$	$E_c(V)$	$I_{fp}(A)$	$I_{rp}(A)$
1.	Fe(II)+MPN+TBATFB	0.938	-0.891	$1.5e^{-4}$	$-2.5e^{-4}$
2	Fe(II)+DMSO+TBATFB	0.65	-0.006	$9e^{-5}$	$-9.8e^{-5}$
3.	Co(II)+DMSO+TBATFB	1.1	-1.5	$5.8e^{-5}$	$-2.5e^{-5}$
4.	Mn(II)+DMSO+TBATFB	-0.16	0.1	$5.3e^{-5}$	$-5.7e^{-5}$

Table 3.6. HOMO-LUMO gap and diffusion coefficient extracted from CV analysis

No	d(eV)	$D_{\text{ox}}(\text{cm}^2\text{s}^{-1})$	$D_{\text{Red}}(\text{cm}^2\text{s}^{-1})$	$D_{\text{Tot}}(\text{cm}^2\text{s}^{-1})$
1.	0.947	4.71e^{-11}	5.50e^{-11}	1.021e^{-10}
2.	1.105	1.93e^{-11}	1.88e^{-11}	3.81e^{-11}
3.	1.139	1.89e^{-11}	3.66e^{-11}	2.26e^{-11}
4.	1.464	1.57e^{-11}	1.79e^{-11}	3.35e^{-11}

3.3.3.1 Diffusion ratio

Diffusion coefficient analyses can describe the mass transport behavior of the charge carriers due to the thermodynamic equilibrium in TEC. Near the working electrode, the diffuse layers with nonzero net charge can be simplified as a diffusion ratio. The diffusion ratio represents the ratio of total oxidation activity over total reduction process of the charge carriers, at both the hot and cold electrodes. Figure 3.23 shows that, the diffusion ratio of Fe(II) in MPN and DMSO were dominated by the oxidation process due to the fact that the value of the diffusion ratio was more than unity, as expected for a diamagnetic Fe(II) complex. Fe(II) shows unique trend of diffusion ratio in MPN compare to the Fe(II) diffusion ratio in DMSO which is more linear. This trend was expected, due to the agglomeration formation of the Fe complex in high polarity MPN solvent that can trap the ionic charge carrier. This contributes to high total diffusion, consequently resulting in high Seebeck coefficient in the temperature range of $T=300\text{-}320\text{ K}$, compared to the no agglomeration formation of the Fe complex in low polarity DMSO solvent. However, the diffusion ratio of Mn was above unity only in the temperature range of $300\text{-}320\text{ K}$, and was less than unity after 320 K . The reduction process of the Mn(III) complex to Mn(II) was inferred to be more difficult at high temperatures due to high molecular distortion of paramagnetic Mn complexes resulting from the Jahn-Teller distortion. The same observation was obtained for the Co complex, where the diffusion ratio became less

than unity after applying heat which indicates the difficulty in oxidising a highly distorted structure of the paramagnetic Co(II) complex. Once Co(II) complex was oxidised to become Co(III), the Co(III) achieved the HS state and was easy to reduce. However due to the high octahedral distortion when changing from LS to HS and vice versa, the reversibility of the LS Co(II) to Co(III) complex vice versa was found to be difficult. This is supported by the large redox separation potential of the CV for the Co metal complex. The reduced Co complex was difficult to oxidise back. The diffusion ratio for all complexes was very useful in predicting the sign of the Seebeck gradient sign, where the sign is positive for diffusion ratio larger than unity, and negative for the diffusion ratio less than unity.

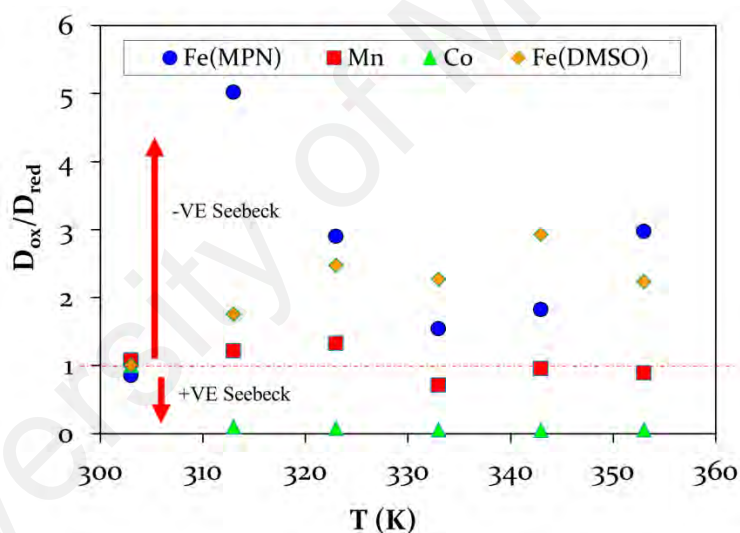


Figure 3.23. Diffusion ratio extraction from CV scan rate 5 mVs^{-1} as a function of temperature for Fe(II) in MPN Fe(II) in DMSO Mn(II)in DMSO and Co(II) in DMSO

3.3.3.2 Total Electrode Formal Potential

As shown in Figure 3.24, the total electrode formal potential shows the electron transfers kinetics between the charge carriers and the electrode (in this case Pt blocking electrode). The molecular conformational changes of the SCO complexes may lead to changes in the gradient and sign of the total electrode formal potential, due to the

differences between electrochemical HOMO-LUMO gap energy at the hot and cold electrodes.

The CV analysis provided the electrode's formal potential as a function of temperature had demonstrated unique characteristic for each complex. The electrode formal potential for high stability LS diamagnetic Fe complexes, showed a linear relationship with temperature, in both high polarity MPN solvent and low polarity DMSO solvent. The magnitude of electrode formal potential for Fe in MPN (range 0.05 ± 0.5 V) was higher than the magnitude of electrode formal potential for Fe in DMSO (range -0.005 V to -0.045 V). Hence we inferred that Fe complex in MPN will generate higher Seebeck due to higher over potential generated compared to Fe in DMSO solvent over a temperature difference.

In the case of Mn and Co complexes, higher distortion and change of spin state can be seen from the electrode formal potential trend, where both have a third order polynomial trend. The transition of spin state from LS to HS for both complexes at transition temperature 320-330 K can be observed through the minimum and maximum value of the electrode formal potential as a function of temperature. Electrode kinetic reaction that was deduced from the electrode formal potential is expected to have a significant impact on the Seebeck coefficient and ionic conductivity that will be explained in the following ionic conductivity sections.

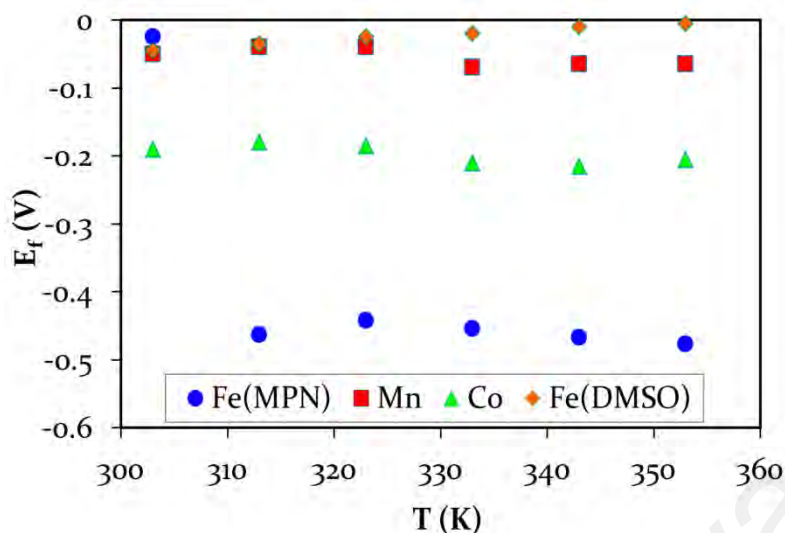


Figure 3.24. Total electrode formal potential extraction from CV scan rate 5 mVs^{-1} as a function of temperature for Fe(II) in MPN Fe(II) in DMSO Mn(II)in DMSO and Co(II) in DMSO

3.3.4 Ionic conductivity

Diffusion activity of the metal complex as a function of temperature is a major contribution to the ionic conductivity of the complexes. Higher diffusion ratio and magnitude of Fe(II) in MPN compared to the others has been proven based on ionic conductivity measurement. Figure 3.25 shows that Fe in MPN has a higher ionic conductivity, by three orders of magnitude compared to the other samples.

The complexes demonstrated nonlinear characteristics of ionic conductivity as a function of temperature due to changes in its spin state when stimulated by heat. The high conformational stability of the LS Fe complex in MPN is the key factor that leads to the high ionic conductivity for Fe in MPN. The lower stability of the agglomerated Fe complex in MPN solvent at temperature range 318-320 K, also explained why the conductivity of the Fe in MPN decreased significantly with increasing temperature. In the case of no agglomeration of Fe in DMSO, the ionic conductivity showed a more linear trend as a function of temperature compared to the Fe in MPN. The ionic conductivity of Co showed a step profile due to the change of LS to HS state at the transition temperature of 320 K. Interestingly, for the Mn complex, the crossover of the ionic conductivity was

found after the transition temperature (320 K) due to the change from LS to HS state. The lower energy of the d-orbital for the HS Mn complex compared to the higher energy of the LS Mn complex, led to the drastic increasing of ionic conductivity of the distorted Mn complex at higher temperature. We inferred that the best selection complex for TEC in this study was Fe in MPN which has both high Seebeck and ionic conductivity. The power output density of Fe complex in both MPN and DMSO solvent were further investigated using non-isothermal measurement, to demonstrate the interaction between the solvent and ion complex that can affect the TEC performance.

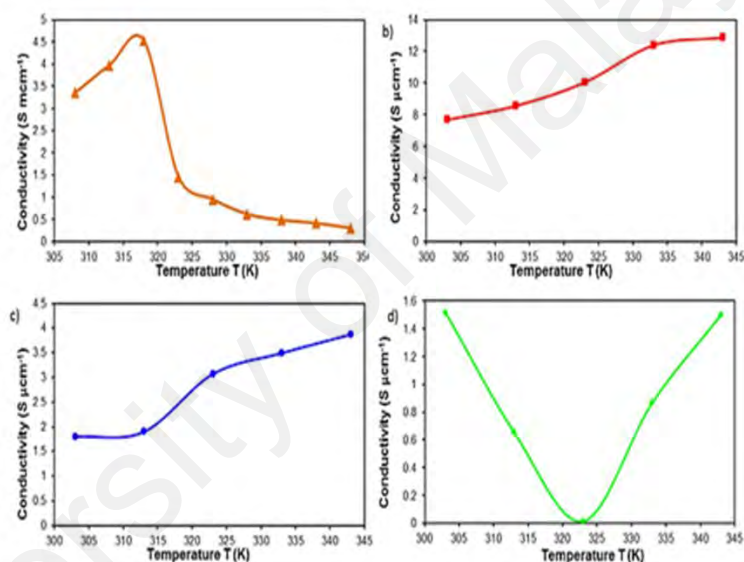


Figure 3.25. Ionic conductivity of a) Fe(II) MPN b) Fe(II) DMSO c) Co(II) DMSO and d) Mn(II) DMSO

3.3.5 Seebeck coefficient

Seebeck coefficient for the complexes were measured using the isothermal two beaker experiment, for three cycles, where $T_{\text{cold}} = 305\text{K}$ and $T_{\text{hot}} = 305\text{-}400\text{K}$. The Seebeck coefficient for the Co complex was $+0.3 \pm 0.01 \text{ mV K}^{-1}$ at $\Delta T = 0\text{-}50 \text{ K}$. Interestingly, there was a change in the Seebeck gradient from negative to positive across the temperature range for Mn. The Seebeck coefficient for Mn was $-0.6 \pm 0.01 \text{ mV K}^{-1}$ at $\Delta T = 0\text{-}25 \text{ K}$ and $+0.4 \pm 0.01 \text{ mV K}^{-1}$ at $\Delta T = 25 \text{ K}$, in DMSO solvent. In addition, enhancement in the Seebeck coefficient for the Fe complex shows that its solubility in a polar MPN solvent

yielded a higher Seebeck coefficient ($-0.96\pm 0.01 \text{ mVK}^{-1}$) compared to the Fe in DMSO ($S_e = -0.5\pm 0.01 \text{ mVK}^{-1}$). Compared to conventional KI-KI₃, the stand alone Fe complex giving much higher Seebeck ($-0.96\pm 0.01 \text{ mVK}^{-1}$) compared to standalone KI-KI₃ ($S_e = +0.5\pm 0.01 \text{ mVK}^{-1}$) in the same solvent.

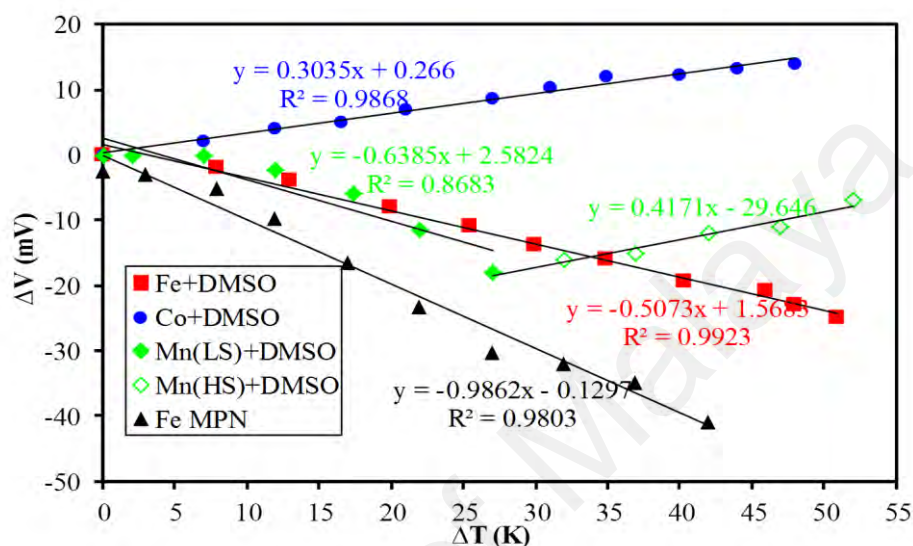


Figure 3.26. Seebeck coefficient of Fe(II) MPN, Fe(II) DMSO, Co(II) DMSO and Mn(II) DMSO

3.3.6 Power density

We have measured power density of Fe(II) complex in different solvent (DMSO and MPN) to show the power density generated by the complexes in different solvent (refer to Figure 3.27). The expected power output for the Fe complex in different solvent supports the fact that the Fe compound with the highest ionic conductivity gave the highest power density, as illustrated in Figure 3.27. The power density of Fe complex in high polarity MPN solvent was three order magnitudes higher than Fe complex in low polarity DMSO solvent. The maximum powers not increase linearly with temperature gradient showing that the effect of spin transition can affect the maximum power generated compared to more linear output power trend for normal redox electrolyte that having no spin state transition at temperature dependent. Interestingly, the effect of spin state transition showing enhancement of temperature gradient at maximum power from

temperature gradient 26 K to 46 K for more stable agglomeration of LS Fe in MPN compared less stable no agglomeration of LS Fe in DMSO. Thus showing that physicochemical of the SCO material at temperature dependent is very significant and worth to be investigated for TEC material development. Power density for Mn and Co cannot be measured due to the fluctuating of unstable power generation observed due to high distortion of paramagnetic Mn and Co. Thus, the standalone of Mn and Co complex inferred to have high distortion and need to be optimise further.

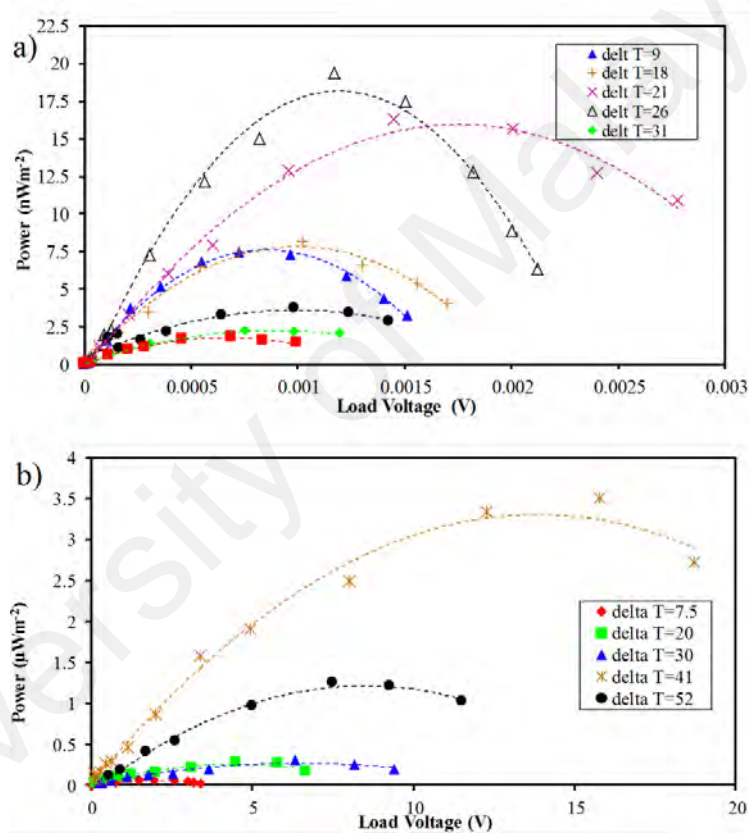


Figure 3.27. Power density of a) Fe(II) in DMSO and b) Fe(II) in MPN at different ΔT

3.4 Conclusions

We have shown the high potential of development of SCO redox electrolytes for TEC low grade heat waste energy harvesting through molecular design and electrochemical analysis. The Fe in MPN solvent has the highest power density as much as three magnitude higher compared with the Fe in DMSO solvent, which is mainly contributed

by the significantly high ionic conductivity in addition to its moderate increase in Seebeck coefficient affected from high stable LS state through agglomeration formation. From the performed temperature dependent analysis of its electrochemical properties using cyclic voltammetry technique, the high ionic conductivity and high S_e of Fe in MPN solvent is due to the high diffusion ratio and activity, and low electrochemical HOMO-LUMO gap energy of Fe complex. Hence, this study showed the capability of low spin type SCO redox electrolyte to harvest energy from temperature different through the molecular modeling and electrochemical analysis at temperature dependent.

University of Malaya

**CHAPTER 4: ENHANCEMENT OF SEEBECK AND IONIC CONDUCTIVITY
SIMULTANEOUSLY OF KI-KI₃ REDOX ELECTROLYTE USING SCO
COMPLEXES MICELLES FORMATION**

4.1 Introduction

Investigation of iodide/tri iodide, (I^-/I_3^-) redox couple based thermo-electrochemical cells (0.4 M) in various solvents have been reported (Abraham et al., 2011) with the S_e range of 0.03 - 0.53 mVK^{-1} . The TECs performance may be further enhanced for S_e value of between 0.813 - 1.67 mVK^{-1} by utilising a combination of redox couples (ferrocene/ferrocenium and iodide/triiodide) to provide a synergistic reaction. The output power of such combinations using a H-cell setup are reported to be in the range of 0.05 - 0.25 μWm^{-2} . This is enabled by the possibility for both ionic species to undergo Grotthus-like conductivity.

Conventionally, complexes of first-row transition metal ions (valence electronic configurations $3d^4 - 3d^7$), with ligands of intermediate field strengths (mostly N-donors) are widely studied as spin crossover materials, (SCO). They have labile electronic configurations that may be switched reversibly from high spin, (HS) to low spin, (LS), or vice versa, when subjected to an external stimulus, such as temperature, pressure, light or magnetic field. Complexes with higher percentages of low spin are expected to be more stable compared to the complexes with higher percentages of HS which are more distorted due to the Jahn-Teller effect. Complexes are expected to experience the Jahn-Teller distortion if the ground electronic configuration of the complexes is orbitally degenerate and asymmetrically filled, which results in a complex distortion of the molecular geometry in order to remove the degeneracy and achieve a lower energy. Studies of TEC electrolytes have shown that the ionic conductivity increases as a function of increased concentration of the redox couple, but at the expense of a reduced Seebeck coefficient. This work aims to overcome this trade-off by proposing a series of SCO materials

possessing an octahedral structure, with the objective of attaining a formulation which is able like “to hit two birds with one stone” by simultaneously increase both ionic conductivity and Seebeck coefficient of conventional redox active electrolyte KI-KI₃.

The strategy to improve the TEC performance of the SCO solution will be threefold which is briefly conceptualised as in Figure 4.1 as follows:

- a) Increasing the Seebeck coefficient of the solution by exploiting the molecular distortion which arises due to the transition of the SCO from LS to HS or vice versa. This distortion will affect the entropy and hence is expected to increase the Seebeck coefficient.
- b) Increasing the ionic conductivity and Seebeck coefficient by manipulating the electrochemical HOMO-LUMO gap which is a function of the molecular bond length, which is in turn, dependent on the spin states. For example, a LS state will result in the SCO complex being in a compression state, and correspondingly, a HS state will result in the SCO to be in an expanded state. It has been previously reported that the LS state is found to be more conductive than the HS.
- c) Increasing both Seebeck and conductivity of redox active material through agglomeration formation of SCO material as charge carrier transport result from lipholicity structure of electropositive and electron-rich of the ionic SCO molecular structure

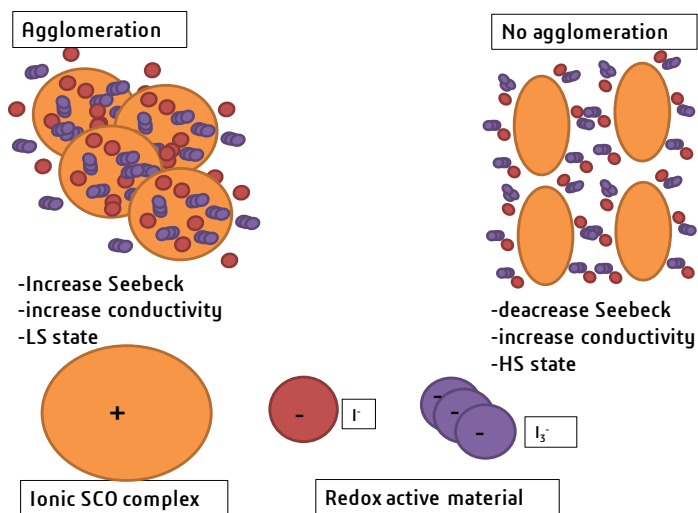


Figure 4.1. Agglomeration formation effect to redox active material

The molecular stability of the SCO complexes will be elucidated using temperature dependent electrochemical impedance spectrometry based on relaxation time of electron transfer, whilst the electrochemical HOMO-LUMO gap will be discussed using cyclic voltammetry data. Consequently, this new perspective of agglomeration formation may provide a molecular design tool for synthesizing spin crossover metal complexes for high performance thermo-electrochemical electricity generation.

4.2 Methodology

4.2.1 Sample synthesis

The proposed structure of three SCO complexes was synthesised using the same method as that used in the previous chapter 3. The syntheses steps for $[\text{Mn}(\text{cyclam})(\text{L14})_2](\text{R})_2 \cdot 4\text{H}_2\text{O}(\text{Mn})$, $[\text{Fe}(\text{cyclam})(\text{L14})_2](\text{R})_2 \cdot 2\text{H}_2\text{O}(\text{Fe})$, and $[\text{Co}(\text{cyclam})(\text{L14})_2](\text{R})_2 \cdot 3\text{H}_2\text{O}(\text{Co})$ can be referred to Figure 3.5 in chapter 3 .

After all the transition metals complexes were synthesised, the complexes (1 mM) were mixed with tetra-n-butylammonium tetrafluoroborate, (TBATFB; 0.3 M) as the supporting electrolyte and with KI-KI₃ (0.01 g) as the redox couple as shown in Figure 4.2. The solvent Dimethyl sulfoxide, (DMSO) was used for Mn and Co and MPN for Fe.

These solvents were chosen due to their high boiling points (189 °C for DMSO and 164 °C for MPN). In this chapter, the prepared samples are referred by sample name as shown in Table 4.1 in addition to the separate condition of solution of solvent mixture (DMSO and MPN), ionic liquid and redox couple with or without complexes

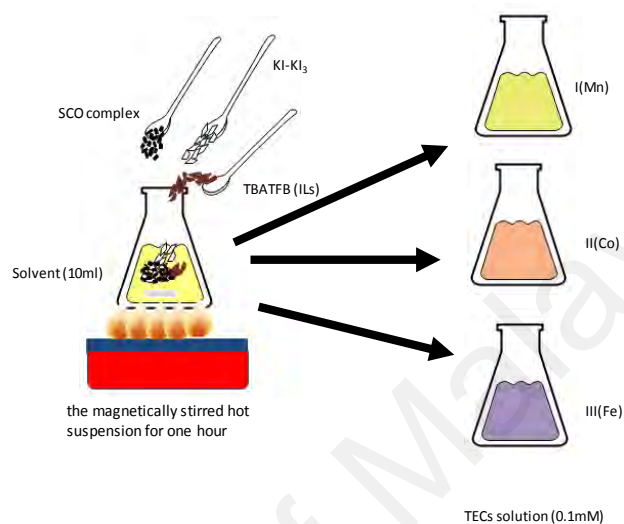


Figure 4.2. Mixture of redox active material with SCO material preparation

Table 4.1. TEC material prepared

No	Sample	Component
1	DMSO+KI-KI ₃	DMSO+TBATFB+KI-KI ₃
2	MPN+KI-KI ₃	MPN+TBATFB+KI-KI ₃
3	Fe(II)	Fe(II)+MPN+TBATFB+KI-KI ₃
4	Mn(II)	Mn(II)+DMSO+TBATFB+KI-KI ₃
5	Co(II)	Co(II)+DMSO+TBATFB+KI-KI ₃

4.2.2 Electrochemical Impedance Analysis

In order to understand the behaviour of the SCO material on relaxation frequency, an electrochemical impedance spectroscopy (EIS) was performed to investigate the relationship of dielectric relaxation time of complexes on spin state at a frequency range of 1 mHz–1 MHz and in the temperature range of 313–343 K. The solutions DMSO+KI-KI₃, MPN+KI-KI₃, Mn(II), Co(II), and Fe(II) were measured in a closed system by using

Pt as the blocking electrode to avoid convection loss. The relaxation frequency is dependent on the spin state of the complexes, denoting different relaxation mechanisms, which could be related to the structural changes (metal to ligand interaction) between the two spin states.

4.2.3 Cyclic Voltammetry

Cyclic voltammetry, (CV) was performed using a Gamry Potentiostat/Galvanostat 600 instrument at 25 °C in order to understand the redox reaction in the samples. A standard three-electrode set-up (platinum working electrode, platinum wire reference electrode, and platinum wire counter electrode) was used. The solution was bubbled with nitrogen gas, (N₂) prior to each scan. The scan rate was 50 mVs⁻¹ and electrode potential values, E(V) were quoted versus Platinum.

4.2.4 Ionic conductivity

Ionic conductivity (σ) was obtained from the measured molar conductivity and directly measured using the multiparameter analyzer (DZS-708) at various temperatures 27-70 °C. The formula used to calculate σ from the measured molar conductivity is $\sigma = (\Lambda_m c)/1000$, where c is the molarity of electrolyte (1 mM) and Λ_m is the molar conductance.

4.2.5 Seebeck coefficient and power

The S_e and power measurements setup used in this study is similar to previous chapter using a digital multimeter (Agilent 34461A) and resistor box. The samples were filled into a cell made up of two compartments and each containing a Pt wire electrode pre cleaned with dilute HCl followed by distilled water and a thermocouple used as temperature probe. The compartments were then placed inside two separate water baths and connected by a short salt bridge containing the same solution. One water bath was heated with a hot plate (hot side), while the other was left at room temperature (cold side). The ΔV between Pt electrode (area = 0.32 cm²) at the hot side and the cold side was

measured in steady state condition at 5 °C intervals, for the temperature range of 25 - 75 °C, using a digital multimeter (Agilent 34461A). The temperatures were confirmed for every reading using a type-K thermocouple that measured the temperature of the solution at both the cold side and hot side. The S_e was determined from the gradient of the linear relation of the ΔV and ΔT plot and all measurements were measured in 3 cycles.

4.3 Results and discussion

For 1 mM, we obtain a clear final solution of Mn(II) and Co(II), but homogenous agglomeration formation was obtained for the Fe(II) solution, as shown in Fig. 3.

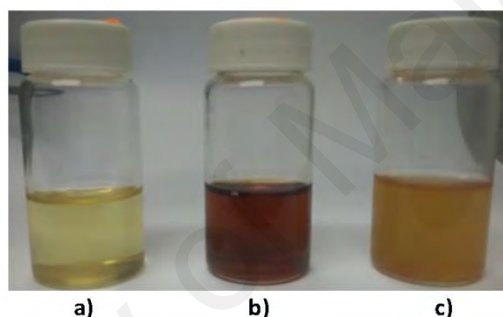


Figure 4.3. Solution prepared a) Mn(II), b) Co(II), c) Fe(II)

4.3.1 Agglomeration studies

For physical investigation, an agglomeration formation that observed for Fe(II) in MPN solvent was further investigated by using optical polarizing microscopy, (OPM), UV-vis spectroscopy analysis and Cyro-Transmission Electron Microscopy, (Cyro-TEM).

4.3.1.1 OPM analysis

Agglomeration formation occurs in sample Fe with KI-KI₃ solution. This is based on visual inspection of the solution prepared compared to the Mn with KI-KI₃ and Co with KI-KI₃ solutions. Figure 4.4 shows a comparison of the OPM images for agglomeration of Fe with KI-KI₃ highlighted with red circle as shown in Figure 4.4 compared to no

agglomeration formation (clear solution prepared of Co with KI-KI₃). Figure 4.3 shows a visual comparison of the agglomerated Fe with KI-KI₃ solution which is cloudier compared to Mn and Co with KI-KI₃ solutions.

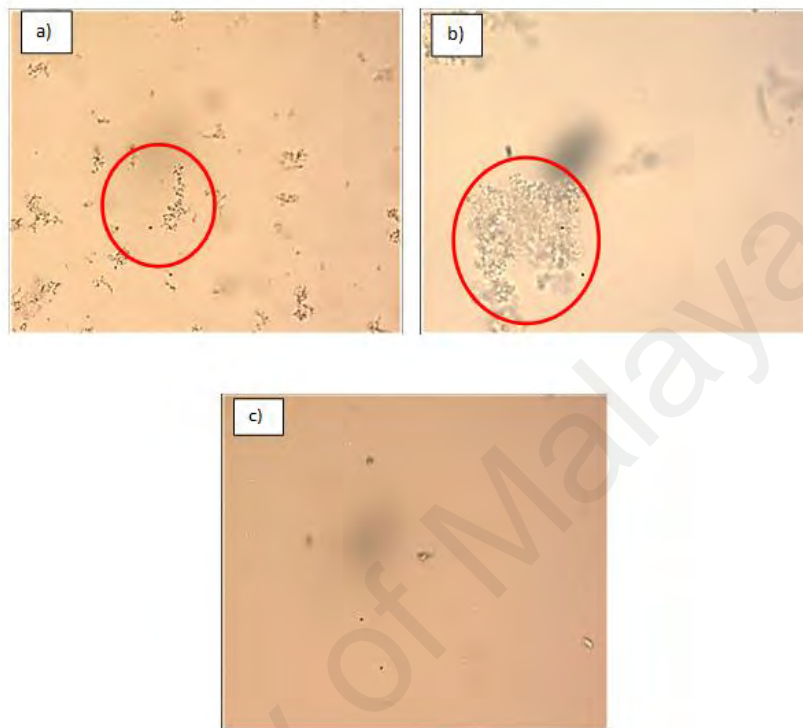


Figure 4.4. OPM analysis a) Fe(II) solution 10x magnification b) Fe(II) solution 50x magnification and c) Co(II) solution 50x magnification

4.3.1.2 UV-vis analysis

The variation of transmitted light through agglomeration suspension was then studied using UV-vis spectrophotometer. Figure 4.5 show the absorbance of the Fe with KI-KI₃ solution against time. It can be seen that at initial stage, the absorbance peak occurred at around 470 nm (Fe complex). Later, peak around 700 nm (KI-KI₃) building up after 20 minutes. The attribute this increases in absorbance due to the increased turbidity due to agglomeration. This hypothesis is also supported by electrochemical analysis discussed in cyclic voltammetry section where the broad peak of redox potential founded was due to the agglomeration formation.

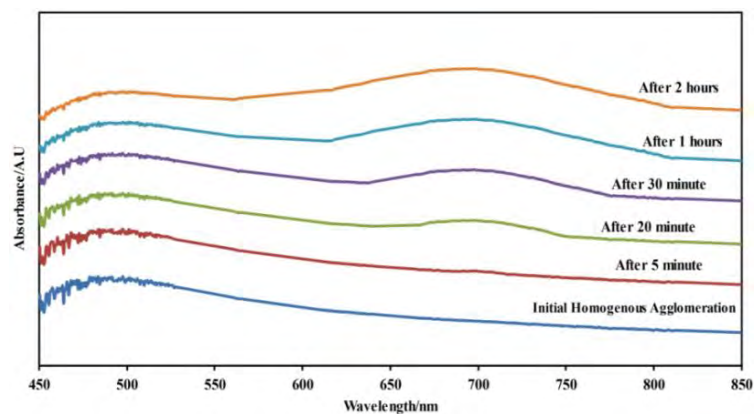


Figure 4.5. Absorbance of Fe solution time dependent

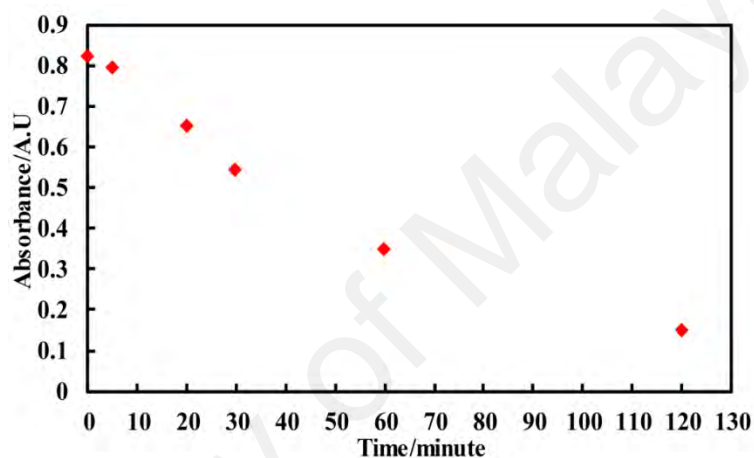


Figure 4.6. Absorbance at 475 nm of Fe solution time dependent

4.3.1.3 Cryo-TEM analysis

Agglomeration formation of Fe complex in redox active material KI-KI₃ was further confirmed by using Cryo-Transmission Electron Microscopy (Cryo-TEM) to observe the type of agglomeration and the agglomeration size. Agglomeration of nanoparticles which inferred by interaction between Fe complex and KI-KI₃ in high polar MPN solvent was observed (refer to Figure 4.7) as spherical micelles in diameter range 100-200 nm.

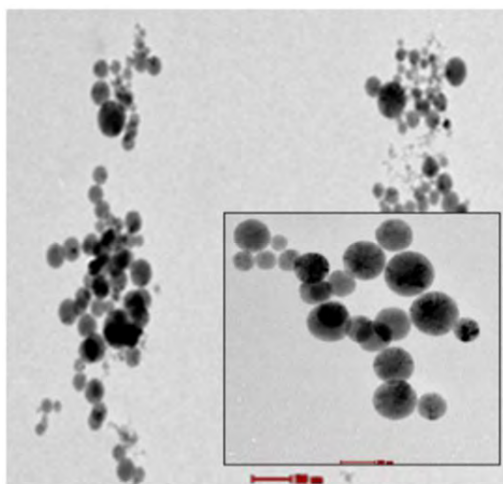


Figure 4.7. Spherical Micelles and agglomeration formation observation using Cryo-TEM analysis

4.3.2 EIS investigation of spin states

In order to understand the spin crossover effect of the complexes in solvent and in the presence of KI-KI₃, temperature dependent impedance spectrometry was carried out to analyse the dielectric relaxation process of the SCO complexes in the temperature range of (313-343K). The loss tangent plots of these samples were calculated from fraction of imaginary dielectric permittivity, (ϵ_i) and real dielectric permittivity (ϵ_r) according to the equation (65-66).

From the control solutions shown in Figure 4.8(a), the loss tangent peak frequencies for the DMSO+KI-KI₃ and MPN+KI-KI₃ samples were the same at temperatures of 303-343 K, as the standalone KI-KI₃ redox solutions are not expected to show spin state transitions. Sample Fe(II) shows a shift from low frequency to high frequency Figure 4.8(b), implying that the $[\text{Fe}(\text{cyclam})(\text{L14})_2]^{2+}$ complex spin transition was from LS to HS with increasing temperature. This is expected to be due to more unpaired electron transfer in the HS state compared to no unpaired electrons in the LS state. However, for $[\text{Mn}(\text{cyclam})(\text{L14})_2]^{2+}$ and $[\text{Co}(\text{cyclam})(\text{L14})_2]^{2+}$ solutions in the presence of KI-KI₃, the loss tangent peaks Figure 4.8(c-d) showed frequency shifting from high frequency to low frequency, indicative of LS transition to HS with increasing temperature. This is

suggested to be due to the presence of more paired electrons than unpaired electron in the LS state compared to the HS state, thus resulting in a decrease of ionic conductivity gradient with increasing temperature (after 343K and 350K for Mn(II) and Co(II) respectively). Thus, it can be concluded that the corresponding steady state geometry for the Fe complex is compressed (in the LS state) whilst for Mn and Co the steady state geometric configuration is in the expanded state. It can also be concluded that $[\text{Fe}(\text{cyclam})(\text{L})_2]^{2+}$, $[\text{Mn}(\text{cyclam})(\text{L})_2]^{2+}$ and $[\text{Co}(\text{cyclam})(\text{L})_2]^{2+}$ SCO complexes in presence of KI-KI₃ are able retain to their spin transition properties in a solution of less than 100°C as indicated by the thermogravimetry analysis shown in previous chapter, which shows degradation of the complexes in the temperature range between 130-156°C. The effect of the geometrical state of the respective spin states will be discussed in the context of its Seebeck coefficient in the thermo-electrochemical characterisation studies section.

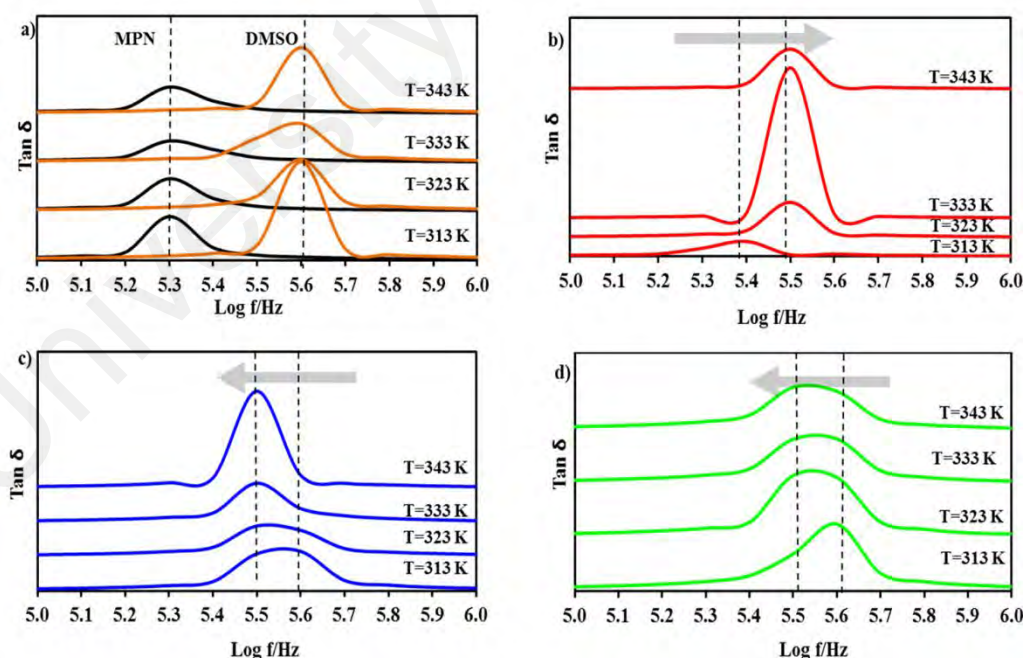


Figure 4.8. Plots of loss tangent peak versus frequency a)DMSO+KI-KI₃) and MPN+KI-KI₃, b)III(Fe), c)II(Co) and d)I(Mn). The arrows indicate transition spin state of the complexes and the black dotted line indicates the frequency at the loss tangent peak.

4.3.3 Cyclic voltammetry analysis

Figure 4.9 shows the measured cyclic voltammograms for DMSO+KI-KI₃, MPN+KI-KI₃, I(Mn), II(Co) and III(Fe) samples. The redox peaks are summarised in Table 4.2. These results will be used to understand the mechanism of redox reaction at the electrodes for the respective complexes. The electrochemical HOMO-LUMO gap, (d) was calculated from the difference between the onsets of redox reaction peaks and are summarised in Table 4.3.

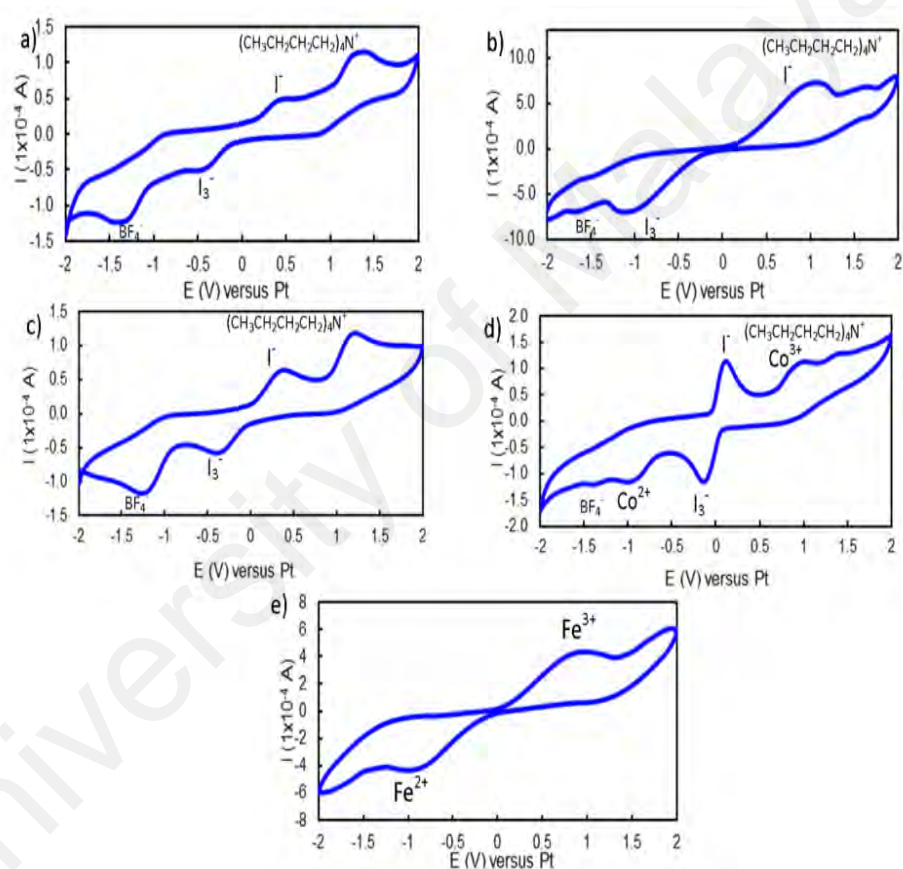


Figure 4.9. Plots of Cyclic Voltammogram a) DMSO+KI-KI₃ b) MPN+KI-KI₃ c) Mn(II), d) Co(II) and e) Fe(II)

Table 4.2. Cyclic Voltammetry Analysis where E_a =anodic potential; E_c =Cathodic potential;
 ΔE_p =Anodic-Cathodic potential separation

Sample	E_a (V)	E_c (V)	ΔE_p (mV)	Reversibility
DMSO+KI-KI ₃	$E_{a1}=+0.337$	$E_{c1}=-0.348$	685	quasireversible
	$E_{a2}=+1.620$	$E_{c2}=-1.620$		
MPN+KI-KI ₃	$E_{a1}=+1.000$	$E_{c1}=-1.000$	1000	quasireversible
	$E_{a2}=+1.250$	$E_{c2}=-1.250$		
I(Mn)	$E_{a1}=+0.237$	$E_{c1}=-0.296$	533	quasireversible
	$E_{a2}=+1.000$	$E_{c2}=-1.000$		
II(Co)	$E_{a1}=+0.070$	$E_{c1}=-0.080$	150	quasireversible
	$E_{a2}=+0.890$	$E_{c2}=-0.890$		
	$E_{a3}=+1.240$	$E_{c3}=-1.240$		
III(Fe)	$E_{a1}=+0.820$	$E_{c1}=-0.820$	1640	quasireversible
	$E_{a2}=+1.000$	$E_{c2}=-1.000$		

Table 4.3. Determined of diffusion coefficient, electrochemical HOMO-LUMO gap, molar conductivity, and Seebeck coefficient of samples

Components	$D(\text{cm}^2\text{s}^{-1})$	$d(\text{eV})$	$\Lambda_m(\text{Scm}^2\text{mol}^{-1})$	$S_e(\text{mVK}^{-1})$
DMSO+KI-KI ₃	1.28e^{-6}	0.24	0.58	+0.44
MPN+KI-KI ₃	3.43e^{-4}	0.21	4.39	+0.25
I(Mn)	1.89e^{-6}	0.04	49	+0.24
II(Co)	7.19e^{-6}	0.02	59	+0.23
III(Fe)	1.32e^{-4}	0.01	40	+0.32

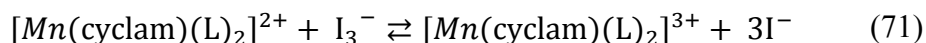
4.3.3.1 Redox reaction of Mn(II) solution under temperature gradient

For the Mn(II) solution two redox peaks due to I_3^-/I^- and TBATFB were observed, as indicated in Figure 4.9(c), and the peak that potentially due to the Mn ion is not visible. This may be explained by the possibility of the Mn solution being in the HS state, and hence the metal centre is shielded by the ligands and is therefore hindered from further participation of Mn(II) in the redox reaction at electrode. For this Mn(II) complex the redox reactions may be described as follows:

Redox reaction 1 (at electrode)



Redox reaction 2 (within electrolyte interface)



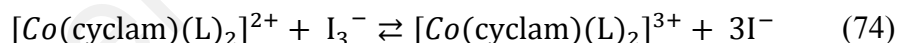
4.3.3.2 Redox reaction of Co(II) solution under temperature gradient

For the Co(II) solution, three redox peaks were detected +0.07 V/-0.08 V (E_{a1}/E_{c1}), +0.89 V/-0.89 V (E_{a2}/E_{c2}) and 1.24 V/-1.24 V (E_{a3}/E_{c3}) as shown in Figure 4.9d. The first strong redox peak (E_{c1}/E_{c1}) was identified as I_3^-/Γ . The second redox peak (E_{c2}/E_{c2}) was proposed for $[Co(\text{cyclam})(L)_2]^{2+}/[Co(\text{cyclam})(L)_2]^{3+}$ and the last peak (E_{c3}/E_{c3}) was identified as TBATFB (redox peak in the range larger than -1 V to +1 V). We proposed that the possibility of redox reactions for Co(II) sample to be summarized as follows:

Redox reaction 1 (at electrode)



Redox reaction 2 (within electrolyte interface)



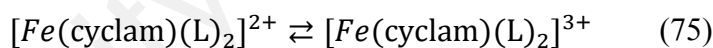
The charge carrier involved in the redox reaction at the electrode was proposed to be I_3^-/Γ and $[Co(\text{cyclam})(L)_2]^{2+}/[Co(\text{cyclam})(L)_2]^{3+}$ due to redox peaks E_{c1}/E_{c1} and E_{c2}/E_{c2} being in the range lower than -1 V to +1 V. The electrochemical HOMO-LUMO gap calculated (0.02 eV) was much smaller than the DMSO+KI-KI₃ sample (0.24 eV) due to the proposed reaction of electron transfer between two redox reactions as shown in the redox reaction 2.

4.3.3.3 Redox reaction of Fe(II) solution under temperature gradient

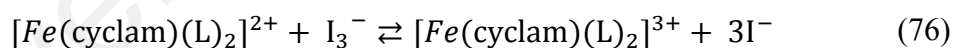
It is interesting to note that for the Fe(II) complex, only a single distinct broad peak was observed, (E_{a1}/E_{c1}), was detected in range -2 V to +2 V at +0.82 V/-0.82 V as shown

in Fig. 8e. We attributed the observation of this single peak to the oxidation of the Fe complex. We propose that E_{a1}/E_{c1} peak was an agglomerated form of $[Fe(cyclam)(L)_2]^{2+}/[Fe(cyclam)(L)_2]^{3+}$. It is believed that the agglomeration of the Fe complex is responsible for hindering the redox reaction of the I_3^-/I^- . The agglomeration also causes a higher internal energy of the system due to the increased elastic interaction within the agglomeration, and this is expected to increase the entropy of the system, and consequently its Seebeck coefficient. Furthermore, the peak of the limiting current for Fe was broad compared to Co and Mn, implying that the relaxation time for the oxidised and reduced states of the Fe ion was longer. Hence, this implies that the oxidised and reduced state of the Fe ion is more stable than Co and Mn. This will be discussed further in the following section. Thus, the redox reactions for the Fe(II) complex may be summarised as follows:

Redox reaction 1 (at electrode)



Redox reaction 2 (within electrolyte interface)



In comparing samples Mn(II), Co(II), and Fe(II), we noted that the ease of removal of an electron from the antibonding e_g orbital for LS $[Co(cyclam)(L)_2]^{2+}$ atom (valence electronic configuration $t_{2g}^6 e_g^1$) is high compared to that from the non-bonding t_{2g} orbital for LS Mn^{2+} atom (valence electronic configuration t_{2g}^5) and LS Fe^{2+} atom (valence electronic configuration t_{2g}^6). This supports our analysis of the electrochemical HOMO-LUMO gap for Mn(II), Co(II) and Fe(II) which were determined to be 0.04, 0.02 and 0.01 eV, respectively, which follow the order of the ease of removal of an electron for the complexes. This shows that the Fe(II) sample has the lowest electrochemical HOMO-LUMO gap, followed by Co(II) and Mn(II). Consequently, at this stage, it can be

summarized that: (a) the redox reactions were quasireversible for Mn(II), Co(II), and Fe(II), and (b) the ease of oxidation of these complexes were in the following order: Co(II) > Mn(II) > Fe(II) and (c) Fe(II) can form stable agglomeration compared to non-agglomeration of Mn(II) and Co(II) with trapped ion inside which can have potential to increase S_e value for TEC system in the same time having lower electrochemical HOMO-LUMO gap.

4.3.3.4 Diffusion coefficient analysis

Ionic diffusion is a measure of the rate of charge transfer in the metal complex solution, and is indicative of the molecular structure of the respective metal complex. The diffusion coefficients (D) for Fe(II), Mn(II) and Co(II) sample, were calculated at 25 °C using the following Randles-Sevcik equation. The calculated D is summarised in Table 4.3 and was found to be decreasing in the following order: Fe(II) > Co(II) > Mn(II). Therefore, from these results, it is inferred that Mn^{2+} has a smaller molecular size than Co^{2+} , which may be explained as follows: (a) all five valence electrons of LS $[Mn(cyclam)(L)_2]^{2+}$ atom occupy the non-bonding t_{2g} orbitals, while the seven valence electrons of LS $[Co(cyclam)(L)_2]^{2+}$ atom occupy the non-bonding t_{2g} orbitals and an antibonding e_g orbital. Hence, the Mn^{2+} -N bonds were stronger (shorter) than the Co^{2+} -N bonds; and (b) the octahedral geometry of $[Mn(cyclam)(L)_2]^{2+}$ in Mn(II) sample was less distorted compared to $[Co(cyclam)(L)_2]^{2+}$ due to the insignificant Jahn-Teller effect experienced by the former complex. In the case of $[Fe(cyclam)(L)_2]^{2+}$ in MPN, it was found that the D value of Fe(II) was larger than the value of Mn(II). This was expected with respect to the above arguments since Fe(II) has a smaller molecular size (stronger Fe^{2+} -N bonds and less geometrical distortion). The values of D for Fe(II) is two magnitudes higher larger than Mn(II) and Co(II) and yet it's molar conductivity and ionic conductivity are the smallest due to having more trapped KI-KI₃ in the Fe(II) complex agglomeration formation.

4.3.4 Seebeck coefficient measurement of SCO complexes with KI-KI₃

Figure 4.10 shows the measured ΔV as a function of a given temperature difference ΔT for Mn(II), Co(II) and Fe(II) samples, in order to calculate the Seebeck coefficient, S_e ($\Delta V/\Delta T$) of the respective solutions. From this figure, it is found that the measured ΔV were in a linear relation with ΔT in the range of $\sim 2 - 40$ K for both I(Mn) and Co(II), and $\sim 2 - 50$ K for Fe(II). From the gradient of this relationship, the S_e of Co(II), Mn(II) and Fe(II) samples were determined to be 0.24 ± 0.02 , 0.23 ± 0.01 and 0.32 ± 0.01 mVK⁻¹ respectively. The measured S_e of the proposed material, Fe(II) was larger than MPN+KI-KI₃ (0.25 ± 0.01 mVK⁻¹) and comparable with reported S_e of I₃⁻/I⁻ (0.34 ± 0.01 mVK⁻¹) in the same MPN solvent but with higher molarity (0.4 M) compared to the low molarity used in this study (1 mM).

In addition, for the case of Fe(II), the S_e value increases to $+0.32 \pm 0.01$ mVK⁻¹ with the addition of low molarity metal complex in comparison to the S_e of the solution without metal transition (sample MPN+KI-KI₃ which has 0.25 ± 0.01 mVK⁻¹). However, for the case of Co(II) and Mn(II) samples, the S_e of the samples were reduced compared to the S_e of DMSO+KI-KI₃ which was $+0.44 \pm 0.01$ mVK⁻¹. The difference of S_e values with the addition of metal complexes can be explained by the agglomeration of structures formed by these complexes, which affects the ionic mobility of the charge carrier in the samples. From the Nernst-Einstein relation it is known that the ionic mobility (μ) is proportional to D .

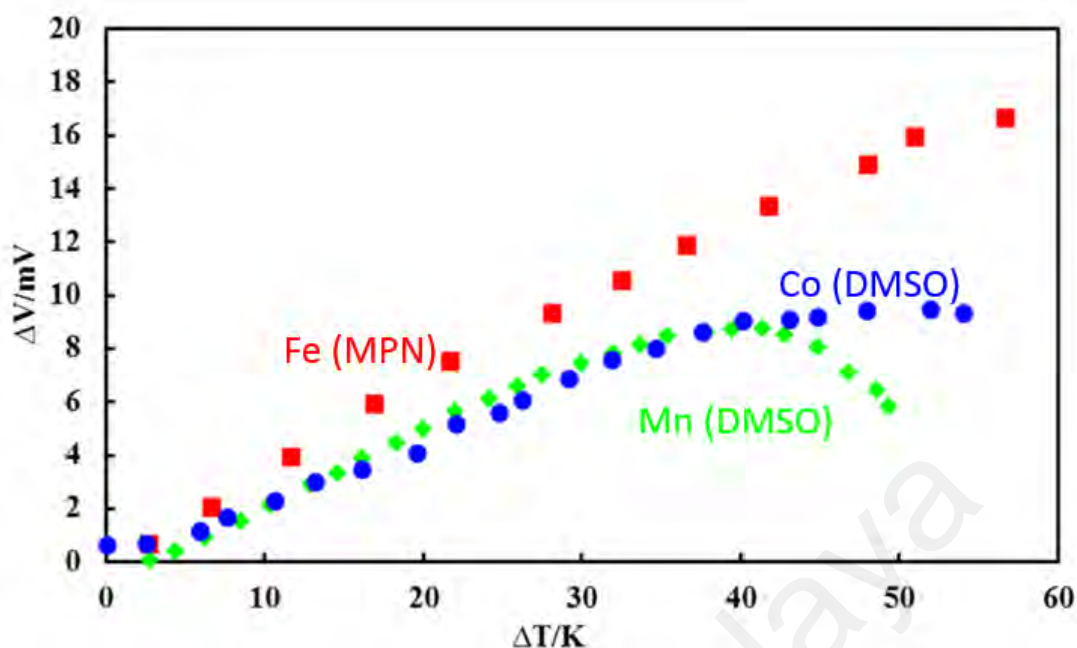


Figure 4.10. Plots of ΔV versus ΔT for solutions of Mn(II), green diamond; Fe(II), red square; and Co(II) blue circle

4.3.5 Ionic conductivity of SCO complexes with KI-KI₃

The σ measured using multiparameter analyzer (DZS-708) for the DMSO+KI-KI₃, MPN+KI-KI₃, Mn(II), Co(II) and Fe(II) are shown in as a function of the average temperature. From Fig. 10(b), it is found that the σ of Mn(II), Co(II) and Fe(II) samples were much higher than the σ of standalone KI-KI₃ without SCO complexes ($\sim 1-9 \mu\text{Scm}^{-1}$) for sample DMSO+KI-KI₃ and MPN+KI-KI₃ refer to Fig. 10(a) and was comparable with the reported thin film SCO complexes ($\sim 2.6 \pm 0.1 \text{ mScm}^{-1}$). This data indicates that a very small amount of the SCO complex is successful in increasing the ionic conductivity by three orders of magnitude, hence providing a pathway for further improvement in thermoelectric performance for solutions containing this SCO complex. The increase in σ of Mn(II), Co(II) and Fe(II) samples is due to the possibility that the KI-KI₃ and SCO ionic complexes to synergistically undergo Grotthus-like conductivity and produces high S_e due to agglomerations (in case of Fe), which allow the ions to be transported.

Moreover, the σ of Fe(II) sample compared with the other two samples was observed to be likely independent of temperature. This trend of σ is consistent with the relative stability of the agglomerations formed by these complexes in solutions: Co(II)<Mn(II)<Fe(II) which effects mobility that is generally proportional to conductivity, as similarly observed in the case of S_e . Agglomerations formed by Co(II) are less stable, allowing for the trapped ions to escape, which led to higher ionic conductivity for Co(II) compared to Mn(II) and Fe(II). Therefore, it is suggested that the ionic conductivity of SCO material can be altered by the type of metal transition through agglomeration.

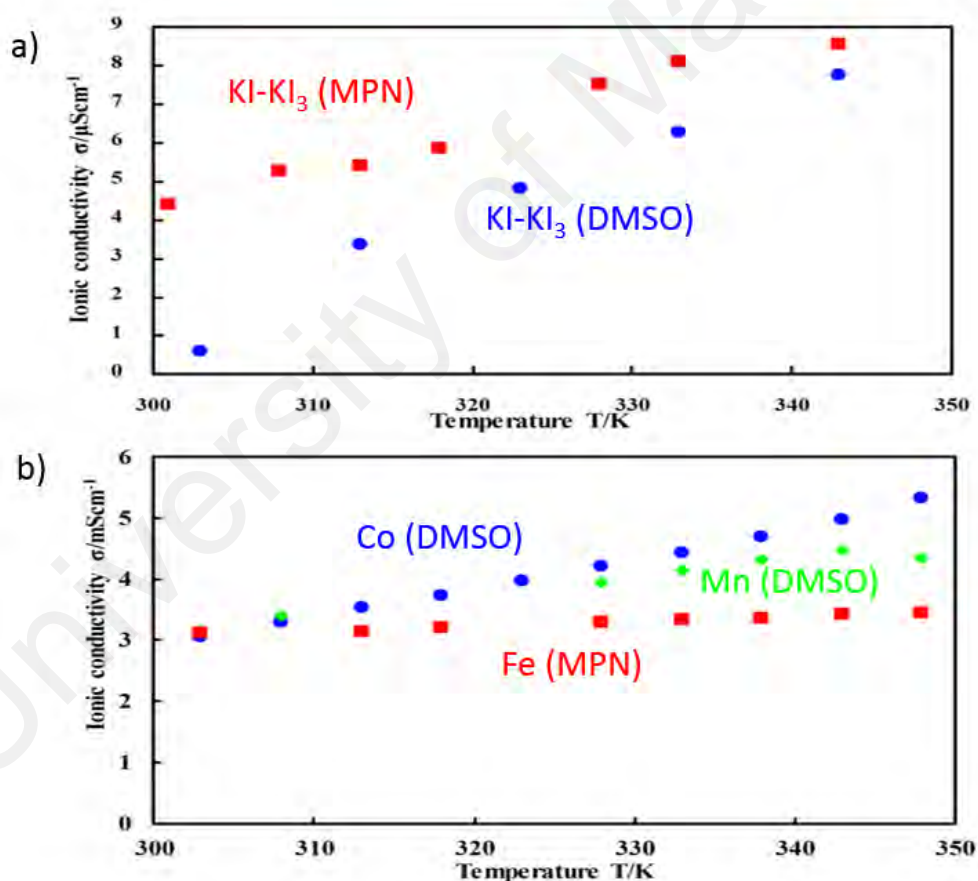


Figure 4.11. Plots of ionic conductivity versus temperature for samples (a) DMSO+KI-KI₃, blue circle; MPN+KI-KI₃, red square and (b) Mn(II), green diamond; Co(II), blue circle; and Fe(II), red square.

4.3.6 Power output

The power outputs for Mn(II), Co(II) and Fe(II) samples were determined at $\Delta T = 40$ K as this was the maximum ΔT to obtain positive S_e for Mn(II) and Co(II) samples, shown in as a function of load voltage. From this Figure 4.12, it can be observed that the maximum power outputs P_{\max} (local maximum peak of the quadratic function) were 4, 5, and $2 \mu\text{Wm}^{-2}$ for Mn(II), Co(II) and Fe(II) sample, respectively. Compared to the other published results, the P_{\max} values produced from these complexes using Pt electrodes were comparable for single cell with output power reported by Anari et al. ($0.25 \mu\text{Wm}^{-2}$) and almost similar with Siddique et al. ($2.13 \mu\text{Wm}^{-2}$). Moreover, these complexes are expected to give high performance at device level which comparable with the power reported by Abraham et al. using carbon nanotube, CNT electrode (0.4Wm^{-2}) and Hu et al. (1Wm^{-2}).

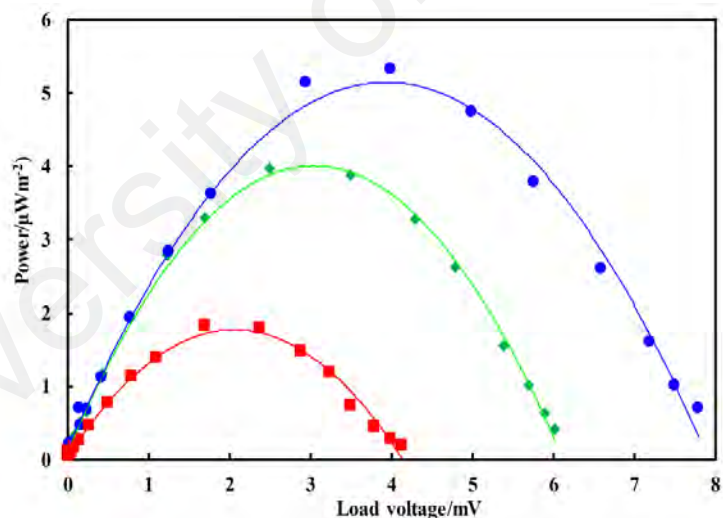


Figure 4.12. Plots of output power versus load voltage for samples Mn(II), green diamond; Co(II), blue circle; and Fe(II), red square

4.4 Conclusions

Three Spin Crossover (SCO) metal²⁺ complexes with transition metals (Mn, Co, Fe) with cyclam and 4-tetradecyloxypyridine (L14) as N-donor co-ligands, and $\text{C}_6\text{H}_5\text{COO}^-$ ion as counter ion were investigated for the capability to enhance thermoelectrochemical

(TEC) materials. A common barrier towards the development of TEC materials is the trade-off between Seebeck coefficient and ionic conductivity. This paper proposes that for this family of SCO complexes can be improved by simultaneously increasing the Seebeck coefficient and ionic conductivity of the conventional KI-KI₃ redox active electrolyte at very low molarities (1 mM) of the metal complexes, which reached at maximum for the case of the Fe(II). For Co and Mn complex both act as catalyst to enhance the ionic conductivity of the KI-KI₃ at very low molarity. Further optimisation of the molecular structure and electrolyte composition is needed for future work to maximize the electrical conversion of the TEC from temperature difference. Central to the molecular design strategy is the agglomeration of the metal complex, particularly for Fe(II), which allows a higher entropy to increase Seebeck coefficient and higher ionic conductivity to increase TEC power output. Thus this indicates a pathway for improving the TEC generation capability through careful selection of octahedral SCO complexes which are able to simultaneously enhance the Seebeck coefficient and ionic conductivity.

CHAPTER 5: THERMO-ELECTROCHEMICAL GENERATION OF PURE MN, FE AND CO WITH N-DONOR LIGANDS CARBON CHAIN 16 AND BENZOATE AS COUNTER ION WITH KI-KI₃

5.1 Introduction

The thermoelectrochemical (TEC) effect allow generation of electrical potential in an electrolyte upon application of a thermal gradient. In previous work, the spin crossover effect in metal complexes have shown to be beneficial to generate high Seebeck coefficient due to the high entropy associated with the conformational in the spin state change. In this chapter, the diamagnetic stability of the SCO material was examined through optimisation of the ligand chain length. The diamagnetic stability of SCO material inferred can enhance the TEC S_e generation through ligand optimisation of the octahedral structure. In this study, the investigation had been done by optimizing the ligand structure to design highly stable diamagnetic complexes for high S_e generation. Weak field ligands stabilize the high spin (HS) state (maximum spin multiplicity) ground state, whilst strong field ligands stabilize the low spin (LS) state (minimum multiplicity) ground state. The coordinate bonds in HS complexes are longer (weaker) than in LS complexes. The strategy to enhance the Seebeck and power densities for TEC is by increasing the ligand field strength is by increasing of the ligand carbon chain length number of previous octahedral structure design in order to improve diamagnetic stability and thermal stability (M. M. I. M. Hasnan et al., 2018). This generally required the use of neutral N-donor ligand ($C_n=C_{14}$) and benzoate as counter ion. In order to maintain intermediate ligand field strength of the complexes to drive SCO effect, the maximum number of carbon chain length(C_{16}) was followed using a concept proposed by Hayami (Hayami, Komatsu, Shimizu, Kamihata, & Lee, 2011). He proposed the “hook” effect of the long alkyl chain which postulated to have ability to pull out the ligand from the metal centre in HS state at room temperature. Upon apply temperature, the van der Waals forces

between the alkyl chains expected to be broken allowing for a closer approach of the ligand to the metal center that drive stable LS state. The carbon chain length of long alkyl chain N-donor ligands increased from C₁₄ to C₁₆ to increase the S_e generation and compared with previous L14 paramagnetic complex for Co, Mn and less diamagnetic Fe respectively. Based on DSC studies of Fe based octahedral complex an endothermic absorption accompanies the spin crossover transition was investigated to be correlated with the diamagnetic induced thermal stabilisation as a function of temperature. This chapters therefore indicates a molecular design strategy of optimisation of SCO metal complex through optimization of ligand chain length.

5.2 Methodology

5.2.1 Ligand (L16) preparation(Hussin, 2016)

A mixture of 4-HOC₅H₄N (5.01 g, 52.70 mmol), K₂CO₃ (17.28 g, 125.10 mmol) and KI (0.33 g, 2.00 mmol) in DMF (200 mL) in a round bottomed flask was stirred vigorously at room temperature. CH₃(CH₂)₁₅Br (15.25 g, 50.0 mmol) was added portion wise to the magnetically stirred solution. The reaction mixture was then refluxed for 72 hours, and left to cool at room temperature overnight. Distilled water was added into the mixture and it was left overnight. The yellow solid formed was collected by suction filtration and washed with distilled water. The product was a white powder and its yield was 12.98 g (81.27%). The structure of the L16 was ascertained using CHN elemental analyses, ¹H-NMR spectroscopy and FTIR.

5.2.2 SCO complexes preparation

The solution of L16 in CHCl₃ (20 ml) prepared then was added portion wise to the three different magnetically stirred suspension prepared same as previous chapter which were (Co(C₆H₅COO)₂(cyclam)(C₆H₅COO)), (Fe(C₆H₅COO)₂(cyclam).2H₂O) and (Mn(C₆H₅COO)₂(cyclam).7H₂O).

The structural formulas of the complexes prepared were deduced using combined analysis of CHN elemental analysis, Fourier transforms infrared spectroscopy (FTIR), nuclear magnetic resonance spectroscopy ($^1\text{H-NMR}$ spectroscopy), ultra violet spectroscopy (UV-vis) and SQUID magnetometer.

The complexes prepared then were dissolved in DMSO for Mn and Co and in MPN solvent for Fe respectively to form 1 mM TEC solution in presence of 1 mM KI-KI₃ as redox active material and 0.1 M TBATFB as supporting electrolyte.

5.2.3 Structural analyses

The CHN elemental analyses(carbon, hydrogen and nitrogen) were recorded on a Perkin-Elmer PE 2400 Series II CHNS/O analyser and Thermo-Finnigan Flash EA 110. A small amount of sample(1.5-2.0 mg) was placed in a tin capsule with a dimension of 5 mm x 8 mm. The weighed sample was wrapped and then folded into a smaller piece before being placed into analyser.

The Fourier transform spectroscopy (FTIR) spectra were recorded neat from 4000-400 cm^{-1} at room temperature on a Perkin-Elmer Spectrum 400 FT-IR/FT-IR Spectrometer with a pike 22107 Technologies GladiATR attachment.

5.2.4 Thermal analysis

Thermal stabilities of the complexes had been determined by thermogravimetry (TG) analysis. The thermogravimetric trace was recorded using Pyris Diamond TG/DTA Perkin-Elmer instrument. An empty ceramic pan was placed in the holder, and then tarred. The sample(about 4 mg) was loaded onto the pan and its weight was recorded. The spectrum was recorded in the temperature range 303-1173 K under N₂ at flow rate 293 K min^{-1} .

The Differential scanning calorimetry (DSC) was performed on a METTLER TOLEDO DSC 822. The sample was weight (about 4.0 mg) in an aluminium pan by using external microbalance and then placed inside the DSC heating stage. The scans were recorded for one heating and cooling cycle in the temperature range 298-390 K. The heating and cooling rates were 278 Kmin⁻¹.

5.2.5 Magnetic analysis

Magnetic properties of complexes can be inferred by ¹H-NMR spectroscopy. Diamagnetic complexes are NMR active, and therefore produce well resolved ¹H-NMR signals. Paramagnetic complexes are partially NMR active, and therefore do not produce well resolved ¹H-NMR signals (the broadening peak) or some peaks were missing) due to the unfavourable electronic relaxation time.

In order to investigate magnetism at dependent temperature, SQUID magnetometer analysis had been used to measure magnetic susceptibility value at dependent temperature.

5.2.6 UV-vis spectroscopy

The UV-vis spectrum was recorded from 1000 nm to 300 nm on Shimadzu UV-vis NIR 3600 spectrophotometer. An exactly known amount of the sample(about 5 mg) was dissolved in 10 ml solvent and then placed into a 1 cm quartz cuvette. The absorbance spectrum was recorded against the solvent background with the fast scan rate. The molar absorptivity (ϵ_{Abs}) was calculated using the Beer-Lambert law as expressed in equation 3

$$A_{Abs} = \epsilon_{Abs}cl \quad (77)$$

Where A_{Abs} is absorbance, c is molarity, and l is the path length (1 cm).

5.2.7 Non-isothermal Seebeck measurement

The Seebeck coefficient for the complexes were measured using non-isothermal two beaker experiment setup (Abdullah et al., 2015; Abraham et al., 2011; Aldous et al., 2017; Anari et al., 2016; Gunawan et al., 2014; Hasan et al., 2016; Inagaki, Itoh, & Tanaka, 1990; Siddique et al., 2016; H. Y. Zhou et al., 2016) for three cycles in where T_{cold} is 305K and T_{hot} is 300-350K. The temperature for every measurement was confirmed by using thermocouple type K. 1m M of the complexes were dissolved in 10 ml of DMSO solvent for Co and Mn and dissolved in 10 ml of MPN for Fe respectively in presence of 0.1 M TBATFB as supporting electrolyte and 1 mM KI-KI₃ as redox couple. The temperature gradient was confirmed using thermocouple type-K.

5.3 Results and discussion

5.3.1 Ligand 16 characterisation

The results of CHN elemental analyses (76.0% C; 13.1% H; 3.9% N) were in good agreement with those calculated for the empirical formula, C₁₂H₃₇NO (76.5% C; 12.6% H; 3.3% N; formula weight 337.52 g mol⁻¹) (Megat Muhammad Ikhsan Megat Hasnan et al., 2019). Figure 5.1 shown ¹H-NMR spectroscopy analysis for L16, where the corresponding assignments for the ligand structure are as labeled based on the integral of the chemical shift found.

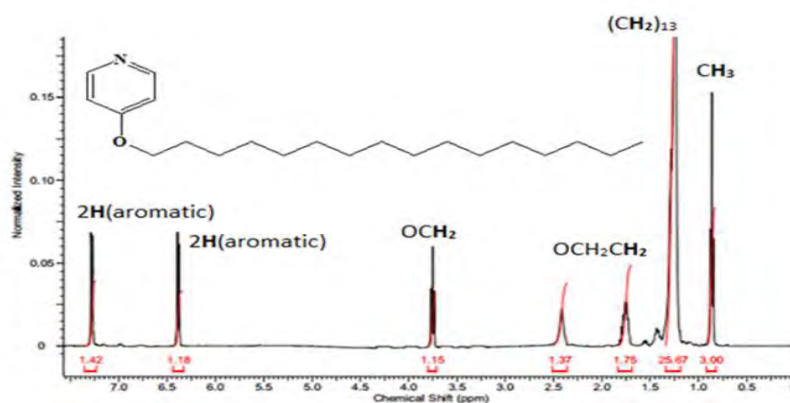


Figure 5.1. ¹H-NMR spectrum of L16 at room temperature

From FTIR spectrum as shown in Figure 5.2, two strong peaks at 2918 cm^{-1} and 2850 cm^{-1} for CH_2 asymmetric and symmetric stretching respectively while strong peaks at 1638 cm^{-1} , 1596 cm^{-1} and 1188 cm^{-1} show assignment for aromatic $\text{C}=\text{N}$, $\text{C}=\text{C}$ and $\text{C}-\text{O}-\text{C}$ stretching respectively which shown good agreement with the formulae structure of L16 deduced from CHN elemental analyses and $^1\text{H-NMR}$.

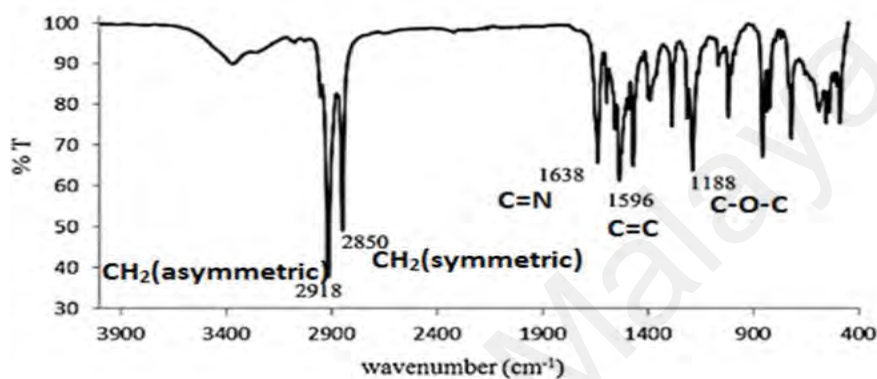


Figure 5.2. FTIR analysis of L16 at room temperature

5.3.2 Fe, Mn and Co complexes preparation

The new complex formulae using new chain ligand assigned as L16 (as compared to ligand L14 were utilized in Chapter 3 previously) were deduced as shown in Table 5.1. Co chemical formula, based on the results of elemental analyses (65.7% C; 9.5% H; 6.0% N), was in good agreement with those calculated for chemical formula $\text{CoC}_{73}\text{H}_{121}\text{N}_6\text{O}_{12}$ (65.7% C; 9.1% H; 6.3% N; formula weight, $1333.71\text{ g mol}^{-1}$). For Fe, the CHN analyses (65.3% C; 10.0% H; 6.0% N) were in good agreement with those calculated for $\text{C}_{73}\text{H}_{121}\text{FeN}_6\text{O}_{12}$ (65.9% C; 9.2% H; 6.3% N; formula weight, 1330.6 g mol^{-1}). The result of Mn elemental analyses (61.2% C; 8.8% H; 6.4% N) was in good agreement with those calculated for the chemical formula $\text{C}_{52}\text{H}_{84}\text{MnN}_5\text{O}_{11}$ (61.8% C; 8.4% H; 6.9% N; formula weight, 1010.2 g mol^{-1}). It was found that from CHN elemental analysis, the new complex synthesised had different in number of mol of water lattice bonding and number of mol of benzoate($\text{C}_6\text{H}_5\text{COO}^-$) counter ion compared to previous study thus suggested valence

charge of the complexes were metal 2+ and metal 3+ for L14 and L16 respectively. The actual binding modes of a RCOO ion inferred from FTIR spectroscopy shown in , based on the difference (Δ) in the values of the asymmetric vibration of COO group (ν_{asym}) and the symmetric vibration of COO group (ν_{sym}) were $\Delta_{\text{COO}}= 206 \text{ cm}^{-1}$, $\Delta_{\text{COO}}= 147 \text{ cm}^{-1}$ and $\Delta_{\text{COO}}= 183 \text{ cm}^{-1}$ for Co, Fe and Mn respectively. Thus, suggesting free (non-coordinated) $\text{C}_6\text{H}_5\text{COO}$ ion binding mode for the complexes.

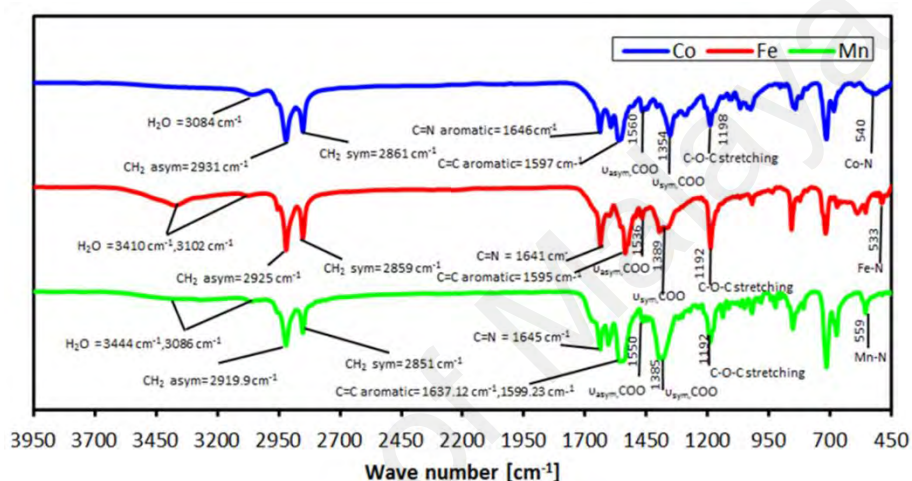


Figure 5.3. FTIR of SCO complexes L16 at room temperature

Table 5.1. Complexes formulae

No	Complex	Ref
1	$[\text{Fe}(\text{cyclam})(\text{L14})_2](\text{C}_6\text{H}_5\text{COO})_2 \cdot 2\text{H}_2\text{O}$	Chapter 3
2.	$[\text{Fe}(\text{cyclam})(\text{L16})_2](\text{C}_6\text{H}_5\text{COO})_3 \cdot 4\text{H}_2\text{O}$	This chapter
3.	$[\text{Co}(\text{cyclam})(\text{L14})_2](\text{C}_6\text{H}_5\text{COO})_2 \cdot 3\text{H}_2\text{O}$	Chapter 3
4.	$[\text{Co}(\text{cyclam})(\text{L16})_2](\text{C}_6\text{H}_5\text{COO})_3 \cdot 4\text{H}_2\text{O}$	This chapter
5.	$[\text{Mn}(\text{cyclam})(\text{L14})_2](\text{C}_6\text{H}_5\text{COO})_2 \cdot 4\text{H}_2\text{O}$	Chapter 3
6.	$[\text{Mn}(\text{cyclam})(\text{L16})(\text{H}_2\text{O})](\text{C}_6\text{H}_5\text{COO})_3 \cdot 3\text{H}_2\text{O}$	This chapter

5.3.3 Thermal properties

Figure 5.4 showed the measured mass loss of the complexes as a function of temperature. The complexes were found to be stable at temperature range 300-400 K. Thus, the complexes were inferred to be stable for TEC application at temperature range 300-400 K. From TG trace, the decomposition temperatures for the complexes were 420 K, 417 K and 413 K for Co, Fe and Mn respectively due to the loss of coordinate H₂O lattice found.

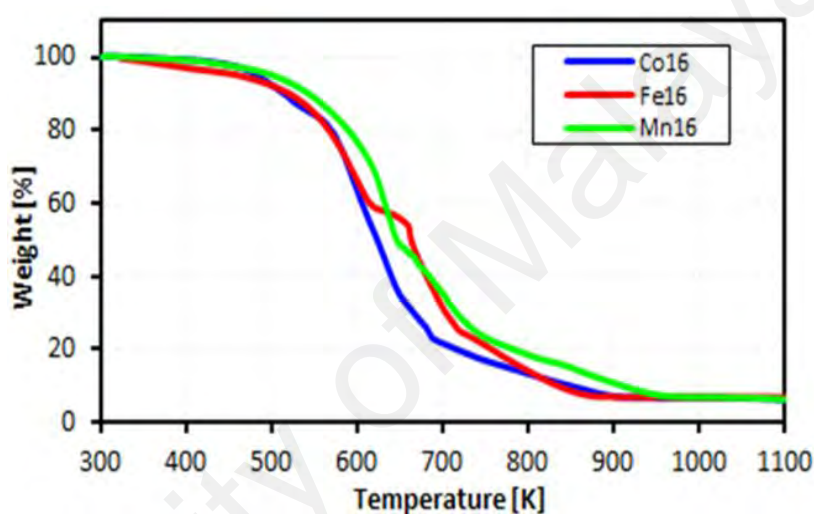


Figure 5.4. Thermogravimetry analysis (TGA) for the SCO complexes L16

Figure 5.5 showed DSC scan recorded in one successive heating–cooling cycle within the temperature range 300-392 K. Co showed strong endothermic peak at 318 K ($\Delta H = +112.6 \text{ kJ mol}^{-1}$) assigned to its melting temperature. On cooling, there was a weak exothermic peak at 328 K ($\Delta H = -2.0 \text{ kJ mol}^{-1}$). Mn showed three endothermic peaks at onset i($T= 303 \text{ K}$, $\Delta H = +13.6 \text{ kJ mol}^{-1}$), ii($T= 321 \text{ K}$, $\Delta H = +1.0 \text{ kJ mol}^{-1}$) and iii($T= 348 \text{ K}$, $\Delta H= +1.1 \text{ kJ mol}^{-1}$). On cooling, only one exothermic peaks at i($T= 318 \text{ K}$, $\Delta H = +1.1 \text{ kJ mol}^{-1}$). Fe showed a strong and broad endothermic peak at 328 K ($\Delta H = 93.1 \text{ kJ mol}^{-1}$) assigned to breaking of strong bonds. On cooling, only one exothermic peaks at i($T= 323 \text{ K}$, $\Delta H = +1.6 \text{ kJ mol}^{-1}$). Thus, Fe showed the highest thermal stability followed by Co and Mn respectively. This observation correlates to the fact that FeL16 complex is the most

stable diamagnetic complex and hence provide the largest entropy change accompanying the spin state transition and correspondingly, highest Seebeck coefficient.

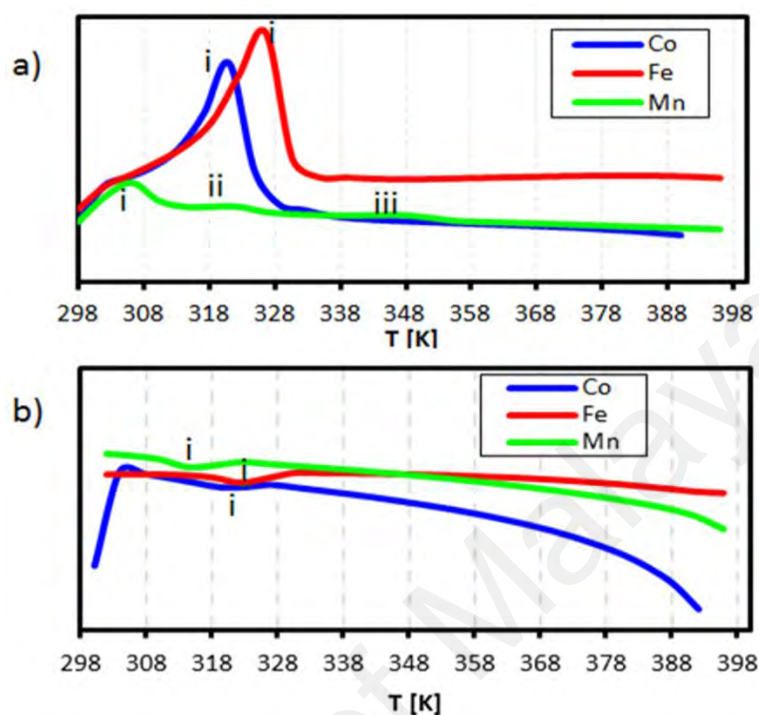


Figure 5.5. DSC scans for a) heating b) cooling of the SCO complexes L16

5.3.4 Magnetic properties

Figure 5.6 was shown $^1\text{H-NMR}$ spectrum for Co, Mn and Fe at room temperature. Co complex showed peak for the organic ligand, suggesting a diamagnetic complex (3d_6 ; LS). However, Fe and Mn showed several broad peaks which indicated paramagnetic magnetism of the complexes at room temperature.

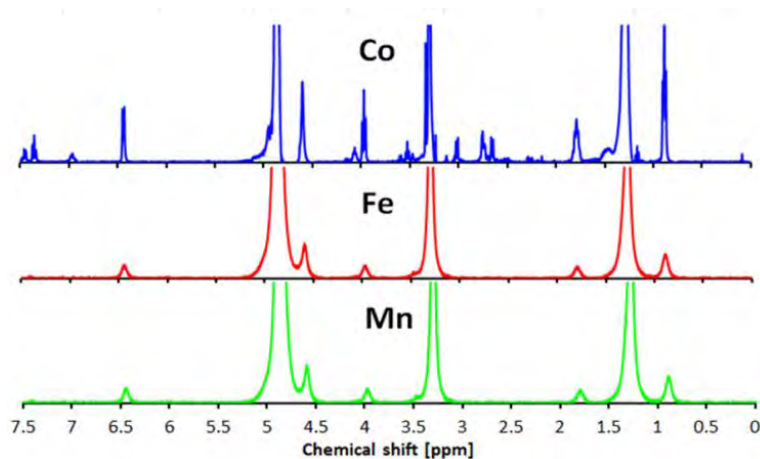


Figure 5.6. ^1H -NMR spectrum of Co, Fe and Mn complex with L16 at room temperature

From SQUID magnetometer analysis at dependent temperature as shown in Figure 5.7 at room temperature (298 K), the magnetism of the complexes showed diamagnetic (LS) for Co($\chi_{\text{M}}T = -0.314 \text{ cm}^3\text{Kmol}^{-1}$) and paramagnetic for Fe($\chi_{\text{M}}T = +0.14 \text{ cm}^3\text{Kmol}^{-1}$) and Mn($\chi_{\text{M}}T = +14.7 \text{ cm}^3\text{Kmol}^{-1}$) which showed good agreement with magnetism of the complex at room temperature found from ^1H -NMR. All complexes showed HS to LS transition with increasing temperature due to the breaking of the van der Waals forces between the alkyl chains allowing for a closer approach of the ligand to the metal center that drives a more stable LS state. (Hayami et al., 2005) Mn complex showed paramagnetic behavior at temperature range 298-390 K suggesting high Jahn-Teller distortion of HS-LS transition. Interestingly, paramagnetic Fe was shown to change to a stable diamagnetic($\chi_{\text{M}}T = -3.31 \text{ cm}^3\text{Kmol}^{-1}$) Fe at transition temperature $T = 350 \text{ K}$. Co showed a two steps LS state transition at temperature 303 K for LS(i) and at temperature 373 K for LS(ii) which expected due to the losses of H_2O lattice bonding upon heating. Hence, it was inferred that in the form of solution, the Fe and Co complexes will form stable LS state in ionic form due to solvation of H_2O lattice. Further investigation was done through temperature dependent UV-vis analysis which presented in next section to investigate the SCO effect of the complexes in the form of solution.

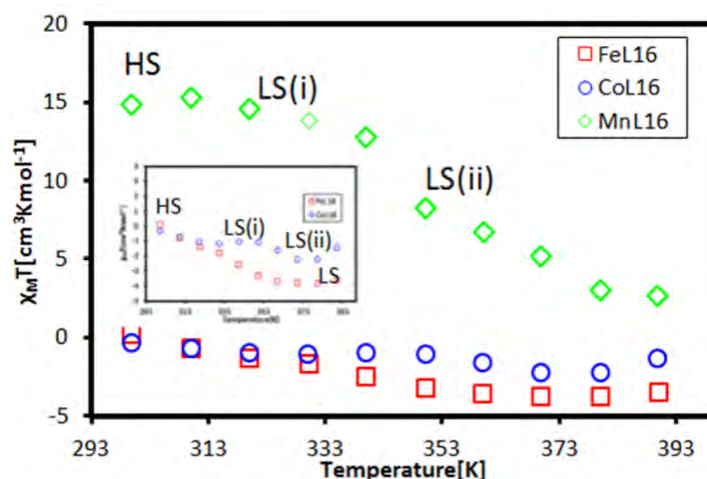


Figure 5.7. Temperature dependent of SQUID magnetometer analysis for complexes L16

5.3.5 UV-vis properties

The UV-vis spectrum as shown in Figure 5.8 for Co showed continuously increasing absorbance from 800 nm to a shoulder of a d-d band (due to the electronic transition from $^1A_{1g}$ to $^1T_{1g}$ for a LS octahedral Co(III)) at about 550 nm of a charge transfer (CT) band at about 286 nm. Fe showed continuously increasing absorbance from 700 nm to a shoulder at 289 nm which proposed for overlapping electronic transition from $^2T_{2g}$ to $^2A_{2g}$, $^2T_{1g}$, 2E_g and $^2T_{2g}$ for an octahedral LS Fe(III) complex. Mn showed the same CT band with Co complex where the absorbance increase continuously from 850 nm to a shoulder of 307 nm suggesting an octahedral LS Mn(III) complex.

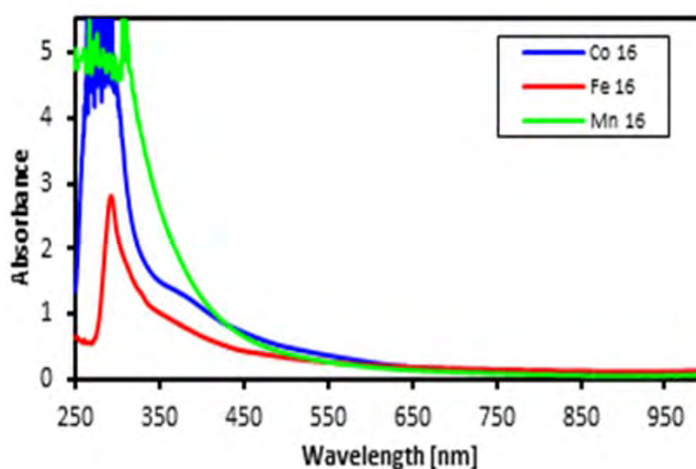


Figure 5.8. UV-Vis spectrum of complexes at room temperature

5.3.5.1 Molar absorption

The absorption spectra of these Fe, Mn and Co in form of solution at different temperatures as shown in Figure 5.9 clearly showed the change in intensities of the spin allowed transitions, due to HS to LS transition vice versa. Co show ϵ values remained unchanged ($863 \text{ M}^{-1}\text{cm}^{-1}$) at first heating cycle at temperature range 300-305 K. Then after 305 K, the molar absorption decreased to $645 \text{ M}^{-1}\text{cm}^{-1}$ and remained unchanged on further heating to 343 K. Upon cooling and reheating, the molar absorption remained unchanged showing that Co complex cannot change to LS once become HS. The Co complex showed a normal SCO behaviour in solution (LS to HS on heating).

Fe showed decreased molar absorption value from $764 \text{ M}^{-1}\text{cm}^{-1}$ to $528 \text{ M}^{-1}\text{cm}^{-1}$ on heating from 300 K to 343 K. On cooling, the molar absorption gradually decreased to $471 \text{ M}^{-1}\text{cm}^{-1}$ and remained constant within the temperature 300-294 K. Upon reheating, the value of ϵ abruptly increased to $840 \text{ M}^{-1}\text{cm}^{-1}$ at 298 K and then decreased abruptly to $441 \text{ M}^{-1}\text{cm}^{-1}$ and $388 \text{ M}^{-1}\text{cm}^{-1}$ at 308 K and 343 K respectively. Thus, Fe inferred to exhibit normal SCO with transition LS to HS on heating and reverse SCO on cooling in form of solution. On reheating, the Fe had shown re-entrant behavior HS-LS-HS transition at 303 K. Thus, Fe showed good SCO reversibility due to the good thermal stability of the long alkyl chain ligand.

Mn shows gradually decreased of ϵ values to $705 \text{ M}^{-1}\text{cm}^{-1}$ on heating. Upon cooling, the value of ϵ gradually increased to $745 \text{ M}^{-1}\text{cm}^{-1}$ and then abruptly decreased to $706 \text{ M}^{-1}\text{cm}^{-1}$ at 343 K. On reheating, the values abruptly decreased to $676 \text{ M}^{-1}\text{cm}^{-1}$ 303 K and then gradually increased to $729 \text{ M}^{-1}\text{cm}^{-1}$ at 308 K. On cooling from this temperature, the value gradually increased until $740 \text{ M}^{-1}\text{cm}^{-1}$ at 298 K. Hence, the Mn complex showed re-entrant SCO at the first cooling mode between at 303-298 K (HS-LS-HS) and upon

second heating (LS-HS-LS) at 293-303 K. The Mn complex was thus inferred to exhibit SCO in solutions.

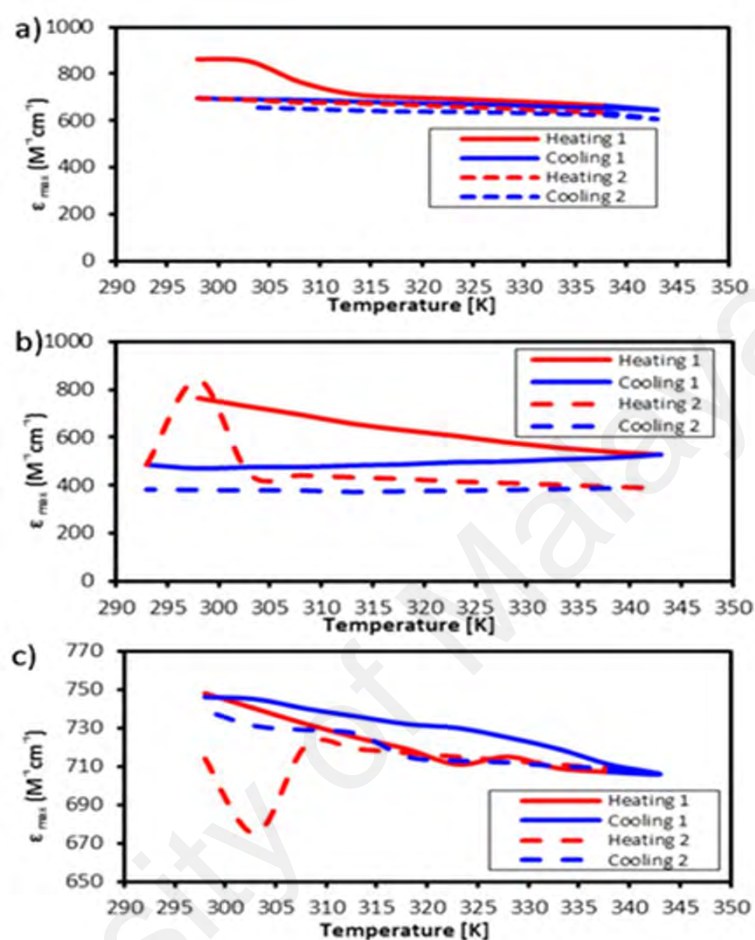


Figure 5.9. Temperature dependent molar absorption values of a) CoL16 b) FeL16 and c) MnL16 in solution.

5.3.6 Seebeck coefficient

Based on the relationship $\Delta V = S_e \Delta T$, where ΔV is potential difference and ΔT is temperature different, the S_e value was calculated from the slope of a linear graph of ΔV versus ΔT that was measured using the non-isothermal Seebeck measurement. Figure 5.10 showed the Seebeck measurement of L14(a previous chapter) and L16 for Mn, Co, and Fe complexes respectively. In terms of S_e sign, Fe shows difference in Seebeck sign which are positive S_e and negative S_e for L14 and L16 respectively. Co complex showed

positive Seebeck sign for L16 whilst L14 showed positive to negative S_e transition at $\Delta T = 40$ K. Mn showed positive S_e sign for both L14 and L16.

The FeL16 complex showed the highest S_e magnitude (-1 mVK^{-1}) compared to the other complexes. The increase of carbon chain length ($C_n = C_{14}$) for the ligand design improved the diamagnetism of the complex upon heating, thus resulting in an improvement of the S_e magnitude for the previous Fe complex compared to a shorter ligand carbon chain length ($C_n = C_{14}$) by 3.43 times Fe complex using L16. Possessing a more stable in the LS state at higher temperature in the same time is able to reverse SCO on cooling was founded of a major key factor that increased entropy reaction in the TEC.

Co that uses L16, was more stable LS state (diamagnetic) compared to distorted (paramagnetic) Co using L14. From S_e measurement, the S_e for Co complex of L16 increased by 1.94 times higher than Co complex contains L14.

However, the Mn complex showed same S_e magnitude ($+0.19 \text{ mVK}^{-1}$) for both L14 and L16 respectively. The S_e did not change due to highly Jahn-Teller distortion whilst entrant/re-entrant SCO mode behaviour of Mn using L16 thus did not give different much on entropy reaction at both hot and cold side of the TEC and non-linear S_e trend. We inferred that paramagnetic behaviour of the Mn complex was not suitable for S_e generation for the TEC devices due to reaction relaxation time was shifting from high to low frequency results from the high Jahn-Teller distortion of the paramagnetic of d^4 Mn(III) complex.

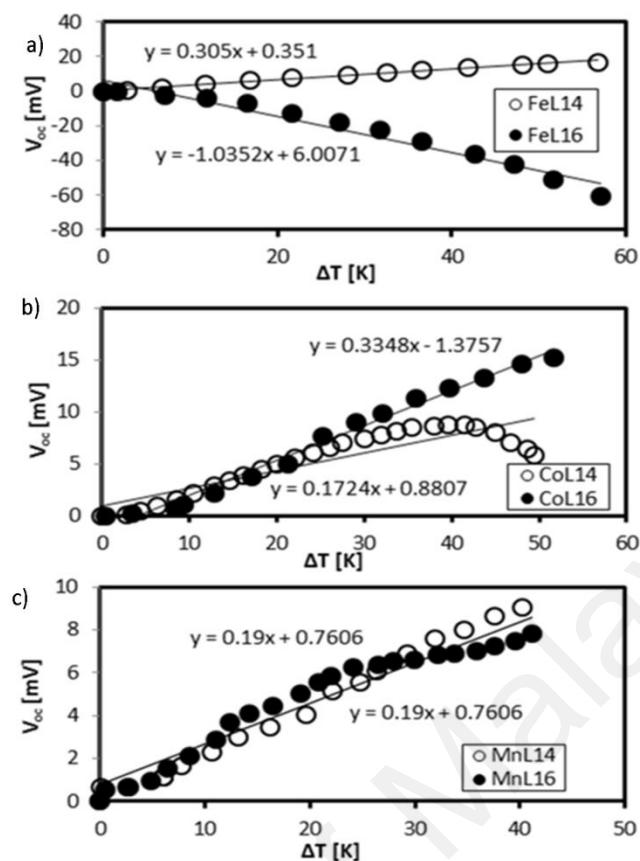


Figure 5.10. Seebeck measurement of a) FeL16 and FeL14 b) CoL16 and Co L14 and c) MnL16 and Mn L14

5.4 Conclusion

This chapter has demonstrated S_e enhancement through enhance of the diamagnetism stability of the metal complexes as function of ligand length. S_e of diamagnetic CoL16 was 1.94 times higher than S_e of paramagnetic CoL14 whilst S_e of diamagnetic FeL16 was 3.43 times higher than FeL14. The enhancement of diamagnetism through the ligand optimisation that enhance S_e generation also can enhance the thermal stability that showed from strong endothermic peak of DSC analysis. This was supported by no enhancement of S_e generation observed for highly paramagnetic MnL14 and MnL16. The high thermal stability of diamagnetism inferred capable in enhancing natural convection thus enhances entropy reaction in the TEC. Thus, this study gives new perspective on developing high S_e TEC material through ligand design strategies based on octahedral structure and magnetic properties optimisation.

CHAPTER 6: ENHANCEMENT OF TEC PERFORMANCE USING SCO

LIGAND 14 WITH KI-KI₃ AND PMMA GEL ELECTROLYTE

6.1 Introduction

TEC devices should be designed as leakage free to maintain electrolyte composition. The physical state of the material for the TEC can be tuned in term of viscosity by using polymer as gelation agent. The challenge is to maintain the TEC performance in terms of redox reversibility and also overcome the diffusion limitation while changing the physical state of the material to become more viscous. To avoid leakage of the electrolyte quasi-solid state electrolyte had been develop by combination of a solid (e.g. polymer) and liquid component (Jin et al., 2016; Wu et al., 2017). The optimal cellulose concentration (5 wt%) the power output only decreased by 20%, compared to the aqueous electrolyte. The increment of the Seebeck of quasi-solid electrolyte had mass transport limitation. Gel electrolyte will be prepared using Poly Methyl Methacrylate, (PMMA) as polymer gelation agent. PMMA was chosen due to the good mechanical strength and ease of free standing gel redox electrolyte preparation. The polymer will be mixed with redox active material and compared in term of TEC power output. In this chapter, gel electrolyte using PMMA as gelation agent was investigated for standard conventional KI-KI₃ as control experiment and FeL14 SCO complex mix with KI-KI₃ to compare with the TEC performance of solution electrolyte. The electrochemical analysis also measured to confirm redox reversibility of the gel electrolyte for TEC power generation capability.

6.2 Methodology

6.2.1 Gel electrolyte preparation

Gelation method was used by mixing the PMMA powder as gelation agent weight ratio 1% with the Fe mixture solution prepared previously as shown in Figure 6.1. The solution was stirred and heated at 70°C for 8 hours. PMMA was chosen due to thermal stability

and solubility in MPN solvent while Fe mixture solution was chosen due to higher Seebeck compared to Co and Mn.

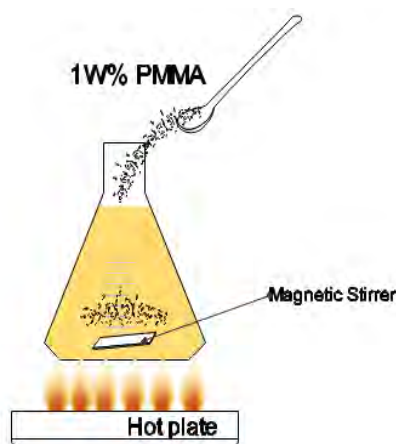


Figure 6.1. Gel redox electrolyte preparations using pure PMMA

6.2.2 Electrochemical analysis

In this section, electrochemical analysis of CV had been repeated to prove that quasi-solid electrolyte can be operate as TEC material.

6.2.3 Power output density

Power output density measurement had been repeated using previous method to highlight the potential of gel electrolyte TEC power generation.

6.3 Results and discussion

6.3.1 CV analysis of gel KI-KI₃ and gel FeL14 complex with KI-KI₃ at room temperature

Figure 6.2 show cyclic voltammogram analysis of gel KI-KI₃ and gel Fe complex with KI-KI₃. It was proven that all gel redox electrolytes can pursue redox reaction in gel form in this case PMMA as gelation agent. Redox potential was summarised as shown in Table 6.1 and Table 6.2. From the redox potential separation, all gel samples were quasi-reversible where gel Fe with KI-KI₃ having smaller redox potential separation than gel KI-KI₃.

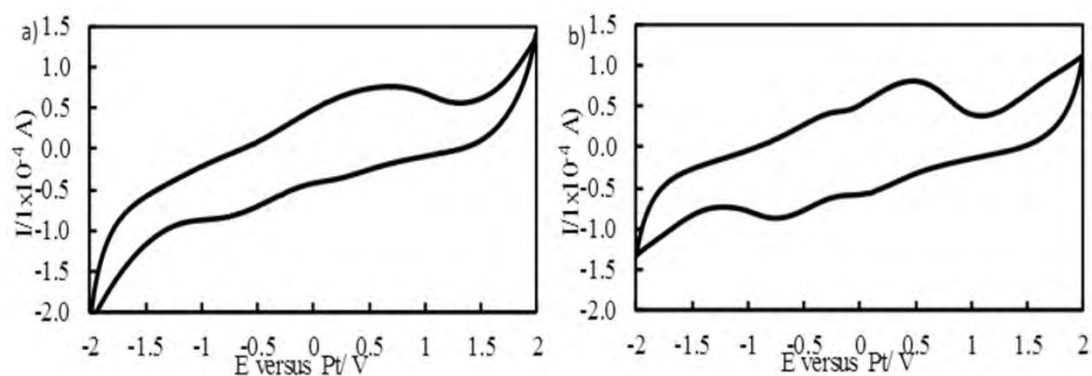


Figure 6.2. CV analysis at room temperature for a) PMMA+KI-KI₃+MPN b) PMMA+Fe+KI-KI₃+MPN

Table 6.1. CV analysis

No	Material	E _a (V)	E _c (V)	I _{fp} (10 ⁻⁴ A)	I _{rp} (10 ⁻⁴ A)
1.	PMMA+KI-KI ₃ +MPN	+0.55	-0.659	+0.74	-0.72
2.	PMMA+Fe+KI-KI ₃ +MPN	+0.4	-0.66	+0.786	-0.837

Table 6.2 Reversibility analysis

No	Material	ΔE(mV)	Reversibility
1.	PMMA+KI-KI ₃ +MPN	1209	Quasi-reversible
2.	PMMA+Fe+KI-KI ₃ +MPN	1060	Quasi-reversible

6.3.1.1 Diffusion coefficient and electrochemical HOMO-LUMO gap

From diffusion calculation based on current limitation peak, there have increment of diffusion rate of gel Fe with KI-KI₃ compared to the gel KI-KI₃. Electrochemical HOMO-LUMO gap for gel Fe with KI-KI₃ also much lower than gel KI-KI₃ which inferred to have potential to have higher Seebeck and ionic conductivity. We inferred that the power output of FeL14 PMMA gel electrolyte were the highest because the total diffusion increase with decreasing electrochemical HOMO-LUMO gap energy. Based on figure of merit ZT governing equation, Seebeck coefficient square was inversely proportional to the diffusion limitation. However trough agglomeration, both parameters can be increases and enhanced by gel formation. We inferred that PMMA gel can

maintain the stability of the agglomeration size and distance between particles compared in solution.

Table 6.3. Diffusion and HOMO-LUMO gap extraction from CV

No	Material	$D_{\text{tot}}(\text{cm}^2\text{s}^{-1})$	$d(\text{eV})$
1.	PMMA+KI-KI ₃ +MPN	5.87e^{-11}	0.5
2.	PMMA+Fe+KI-KI ₃ +MPN	7.21e^{-11}	0.001

6.3.2 Power output density

First gel of KI-KI₃+MPN solvent electrolyte was prepared as reference using pure PMMA as experiment control. Figure 6.3 show power density of KI-KI₃ +MPN gel electrolyte at different temperature gradient. The power density of the KI-KI₃ gel electrolyte is slightly higher than power of solution of Fe complex with KI-KI₃ in MPN solvent. The power also increase linearly with increase of temperature different expected due to no spin state transition for KI-KI₃ redox couple.

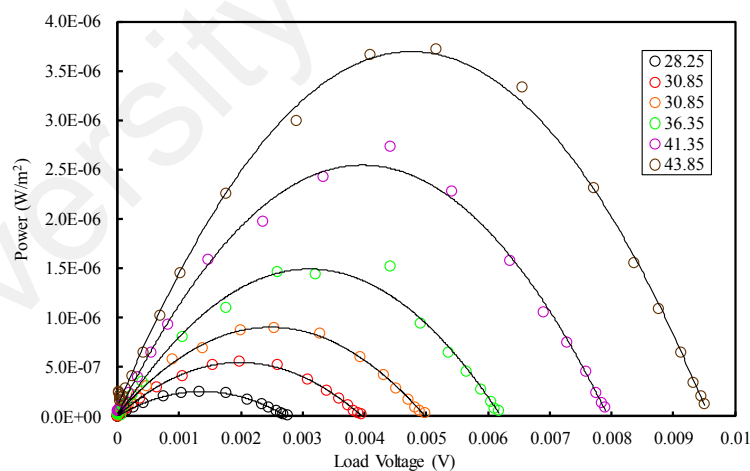


Figure 6.3. TEC Output power of PMMA+KI-KI₃ at different temperature difference

When FeL14 mixture solution with KI-KI₃ in MPN solvent were turned to gel electrolyte by using pure PMMA as gelation agent, the power density as show in Figure 6.4 show enhancement of power density by 1 magnitude order higher compared to TEC electrolyte in solution and gel electrolyte of conventional KI-KI₃ redox couple.

Interestingly, the power density show large increment by 50% after temperature gradient 46 expected due to spin state transition from LS to HS. This step up profile of power density output dependent of temperature showing promising power enhancement capability of SCO material that stimulus by temperature.

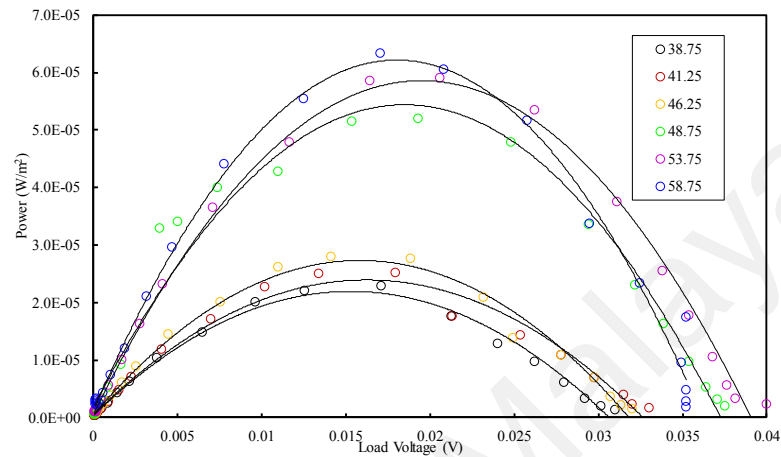


Figure 6.4. TEC Output power of PMMA+Fe+KI-KI₃ at different temperature difference

6.4 Conclusion

This chapter had shown large improvement of TEC output power density using SCO gel PMMA electrolyte compared to solution electrolyte in order to avoid leakage problem. Thus, this is a developing field and there is much unexplored territory and fundamental to develop high mass transport gelled electrolyte based on thermal energy harvesting.

CHAPTER 7: FABRICATION OF MICRO-TEC DEVICES FOR LOW GRADE HEAT WASTE POWER GENERATION

7.1 Introduction

Recent research in liquid state as new thermoelectric materials demands a suitable implementation in an industrially producible generator. Such a high power density micro generator can harvest electrical energy in order to extend battery lifetime or serve as single energy source for medical and wearable applications. Series stacking of numbers of TEC cell can increase the TEC output voltage significantly (S. Uhl et al., 2015). The similar concept that used in solid state thermoelectrics, are equivalent to the n-type and p-type semiconductor stacking in series to maximise power output in which multiple thermoelectric couples are connected in series to maximise power output. For same Seebeck sign, series stacking of the TEC cell will more difficult compared to the TEC cell which having positive and negative Seebeck thus need both P-type and N-type material development. The potential of PVA-based hydrogel electrolyte containing either ferri/ferrocyanide or ferric/ferrous chloride had been demonstrated to be double up but the current are remain the same for series stacking TEC (Zhang et al., 2017). This chapter was motivated by the first and only reported microTEC power generator using MEMS technology (Stefanie Uhl et al., 2014; S. Uhl et al., 2015). A first technological prototype with 1182 serial P-type and N-type connected ionic liquid (IL) cells was presented with no power output evaluation reported until now. The base material of the device fabricated consists of a commercially available metal-clad laminated polyimide sheet (DuPont, Pyralux AP8565) using Deep Reactive Ion Etching (DRIE) and plasma etching to create cavity. The challenge part was high technology electrolyte filling process and device sealing where the samples must be bubble-free sealed.

This study presents the investigation of single cell TEC devices performance using Si as base material which good candidates for high density cell using MEMS fabrication process. This study more like as basis work before fabricating high integrated TEC starting from preparing P-type and N-type material (using conventional iodide/triodide and Fe(II)/Fe(III) redox couples in presence of citric acid as supporting electrolyte and water as solvent) until fabricating the single P-N junction of the TEC device. The prediction of P-type and N-type Seebeck had been shown using Cyclic voltammetry technique then had been proven with the output Seebeck generated from the fabricated devices. To avoid leakage, increasing electrolyte life time and having high thermal gradient, material used in this study as TEC material was synthesised as quasi-solid electrolyte using 5% Wt PVA as gelation agent. Several pair of electrode combination using Pt, Au and porous Si-Pt electrode deposited also had been investigated as Seebeck enhancement strategy to compare with the conventional planar Pt electrode through the additional double layer formation in the porous Si layer.

7.2 Methodology

7.2.1 P-type and N-type TEC material preparation

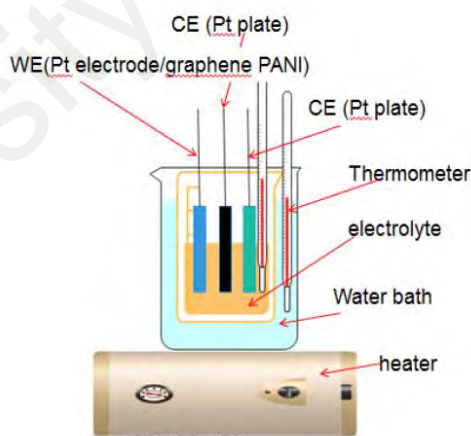
For this work, two type of gel electrolyte were used in this study using 0.25 M iodide/triodide(P-type) and 0.25 M Fe^{2+/3+} (N-type) as redox couple while 5% weight Polyvinyl Alcohol (PVA) as gelation agent dissolve in high polar water solvent(stir at 100 r.p.m at 95°C for 5 hours. For homogenous and high conductivity gel electrolyte due to Grotthus mechanism of H⁺ and OH⁻ bonding, high concentration 10 M of citric acid was used as supporting electrolyte. The quasi state transition of gel electrolyte was confirmed and observed by measuring solution resistance at dependent temperature of iodide/triodide gel electrolyte using HZ-electrochemical potentiostat at frequency 100 kHz.

Table 7.1. TEC material prepared

Type	Salt	Supporting electrolyte	Solvent	Gelation agent
P-type	KI-KI ₃	Citric Acid	Water	PVA (3%,5%Wt)
N-type	FeCl ₂ +FeCl ₃	Citric Acid	Water	PVA (5% Wt)

7.2.2 Temperature dependent CV analysis

Temperature dependent cyclic voltammetry (CV) was used to determine Seebeck coefficient sign of prepared gel TEC material (Koerver et al., 2015). The half-wave potentials extracted from cyclic voltammetry are based on thermodynamic, plus kinetic contribution. The diffusion coefficients of both redox species had been examined, and had been calculated from the Randles-Sevcik equation. Diffusion coefficients were calculated based on the limitation current peak i_p values from the lowest sweep rate ($v = 5 \text{ mVs}^{-1}$) for all temperatures.

**Figure 7.1.** Cyclic voltammetry analyses of isothermal cell setup at dependent temperature

7.2.3 Single cell TEC device design and fabrication

Figure 7.2 shown a single TEC device design used in this study to investigate single cell isothermal TEC device performance. SU-8 polymer was used to bond Si-Ti-Pt electrodeposited with the glass substrate.

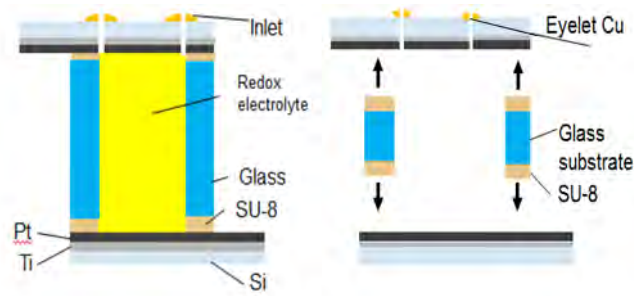


Figure 7.2. Single cell TEC device design using conventional planar electrode

In this study, we measured the power density for the isothermal TEC devices. The TEC devices were fabricated using micromachining technology using the process flow as shown in Figure 7.3. $2 \times 2 \text{ cm}^2$ silicon wafer substrate with $300 \mu\text{m}$ thickness was used as base material due to high thermal conductivity ($148 \text{ Wm}^{-1}\text{K}^{-1}$) for fast heat transfer and fast steady state response and glass and SU-8 dry film resist as intermediate bonding layer which having low thermal conductivity ($0.2 \text{ Wm}^{-1}\text{K}^{-1}$) to maintain the thermal gradient across the TEC. The microTEC fabrication process is as shown in Table 7.2, Table 7.3 and Figure 7.3.

Table 7.2. Upper electrode Fabrication process

a)	Si $300\mu\text{m}$	
b)	Photoresist layer: OFPR 200CP (+ve) Si Photolithography	SUS Aligner
c)	Patterned Si Deep RIE etching	SPT-SRE machine
d)	Pt Si Pt Electrode deposition Sputter	SHIBAURA sputter

Table 7.3. Lower electrode Fabrication process

a)	Si $300\mu\text{m}$	
b)	Pt Si Pt Electrode deposition Sputter	SHIBAURA sputter

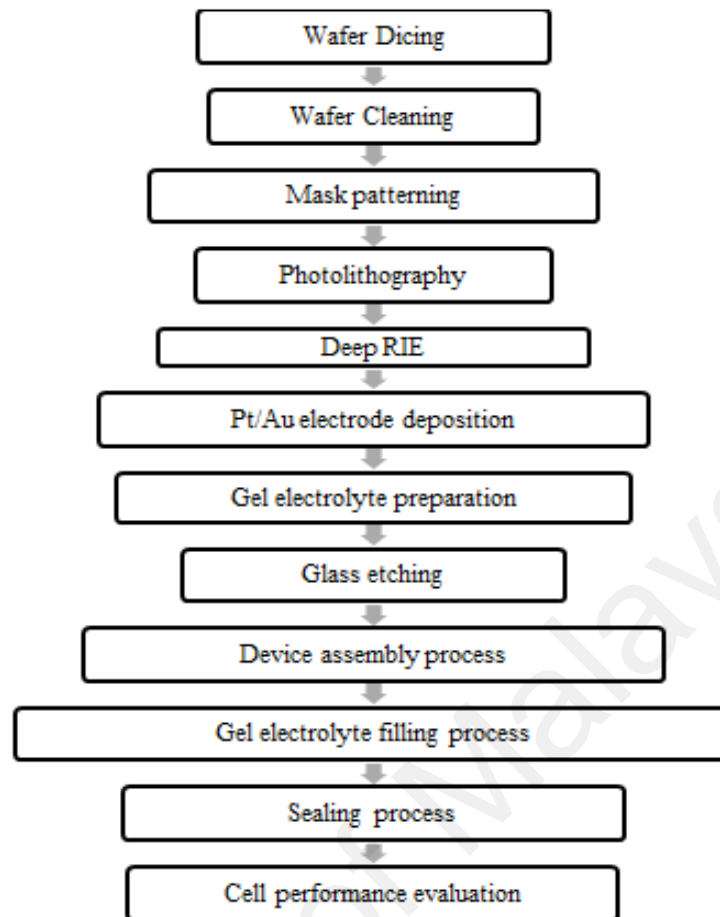


Figure 7.3. TEC device fabrication process flow

(a) *Wafer dicing*

Substrate used for single cell TEC device was 4" silicon wafer with thickness 300 μm . The wafer was cut to 14 part with cross section are $2 \times 2 \text{ cm}^2$ per wafer. Silicon was chosen due to high thermal conductivity 148 W/mK for fast response steady state condition.

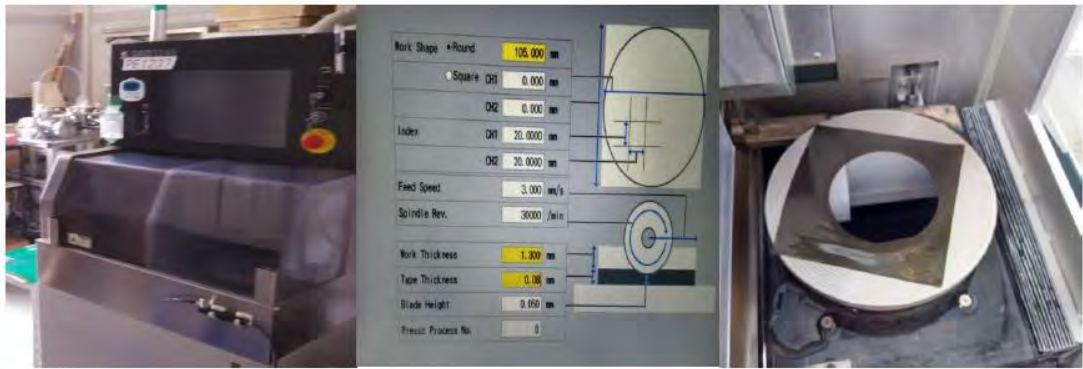


Figure 7.4. Si wafer dicing machine

(b) Wafer cleaning

After wafer dicing, wafer cleaning process as shown in Figure 7.5 was done to prevent micro and nano particles that attached on Si surface while dicing process. Due to the high electrostatic force the nanoparticle attached on Si substrate is difficult to be cleaned thus high heat generate from high chemical reaction of high concentrated acid and base needed to weaker the electrostatic force. All the process was done in clean room.

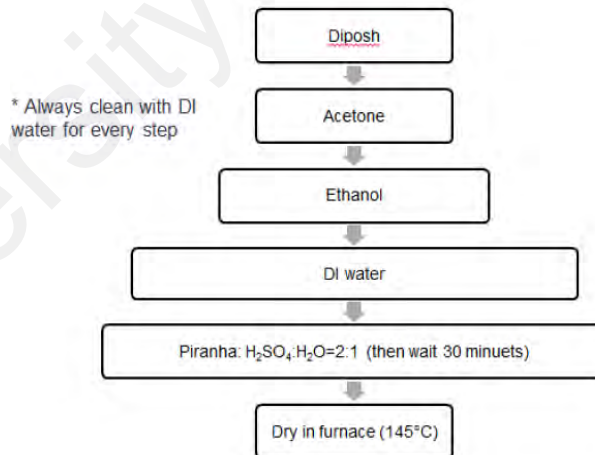


Figure 7.5. Si wafer cleaning process

(c) Photolithography process

Photolithography process for photo masks patterning on Si wafer as shown as Figure 7.6. Mask design was design using Layout editor as shown in Figure 7.9(a). OFPR-200CP

and OAP photoresist solution was coated using spin coater before exposed with UV light using SUSS-mask aligner machine before develop the pattern using TMAH solution.

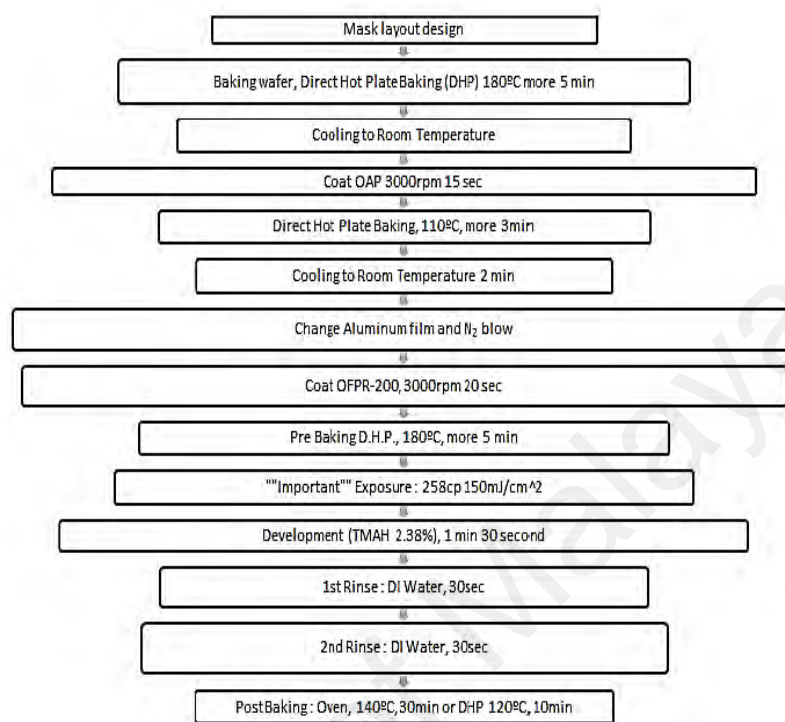


Figure 7.6. Photolithography process flow

(d) **Deep RIE etching**

After photoresist layer developed on Si wafer, the Si wafer was etched using SPT-SRE Deep Reactive ion etching machine as shown in Figure 7.8 using high rate etching for 200 cycles. The dry etching process is using recipe shown in Table 7.4. Before etching process, the substrate was mounted to dummy wafer using coated OFPR200cp layer after soft bake as shown in Figure 7.7. The Si wafer had been dry etched(hole diameter= 0.5 mm) using high rate(800 W coil power, passivation gas: C₄F₈ 140 sccm flow, etching gas: SF₆ 140 sccm flow, pressure 3.7-9 Pa) deep reactive ion etching (RIE) after photolithography process(refer to using OFPR 300 cp as positive photo resist mask. The hole was made as inlet for the TEC device.

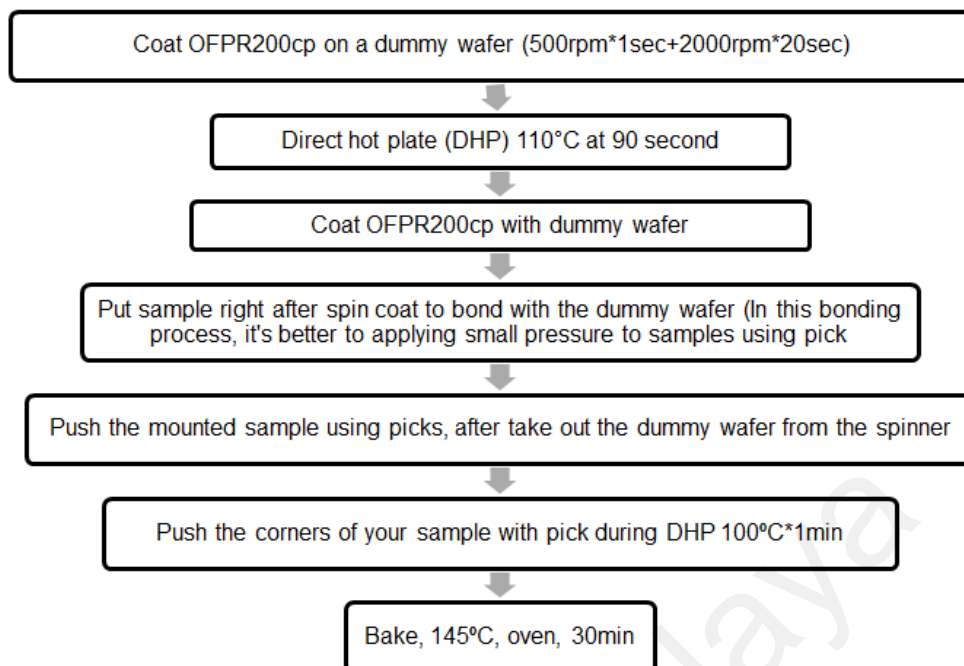


Figure 7.7. Deep RIE dummy wafer bonding process flow



Figure 7.8. SPT-SRE Deep Reactive ion etching machine

Table 7.4. Deep RIE Recipe

Recipe	Phase	Time	Gas	Flow	Coil power	Pressure	Platten Power
High rate	Passivation	6 s	C ₄ F ₈	140 sccm	800 W	5 Pa	0 W
	Etching	2.5-7.5 s	SF ₆	140 sccm	800 W	3.7-9 Pa	23-10 W

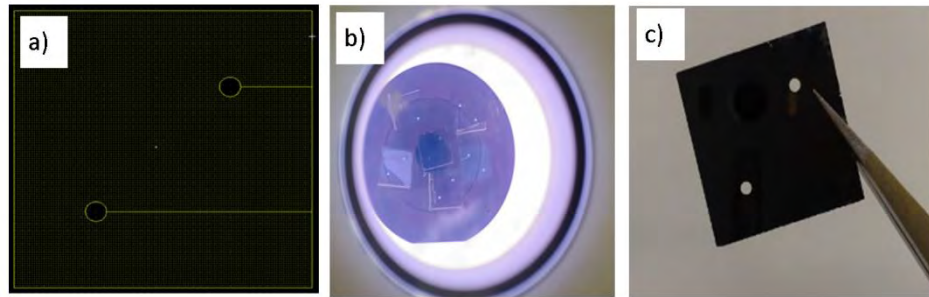


Figure 7.9. Schematic of upper electrode a) positive resist develop mask design b) Deep RIE on process c) Si wafer after deep reactive ion etching

(e) *Post residue remover process*

After deep RIE process, the substrate was separated with the dummy wafer by post residue removing process as shown in Figure 7.10.

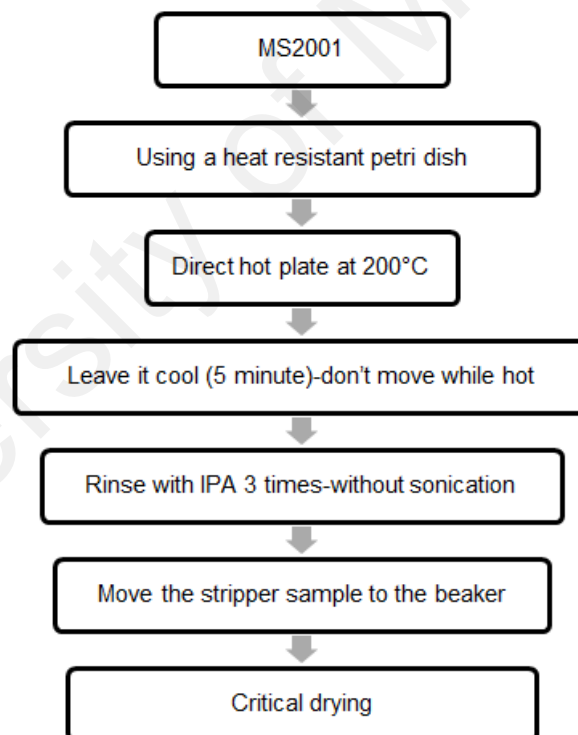


Figure 7.10. Post residue remover process flow after Deep RIE process

(f) *Pt/Ti electrode deposition*

The Si with hole as the upper electrode and Si without hole as the lower electrode was sputtered using SHIBAURA sputter machine to deposit 23.6 nm thickness of Ti layer and

to deposit 420 nm thickness of Pt layer as redox active area(refer to Figure 7.11). The recipe used as shown in Table 7.5

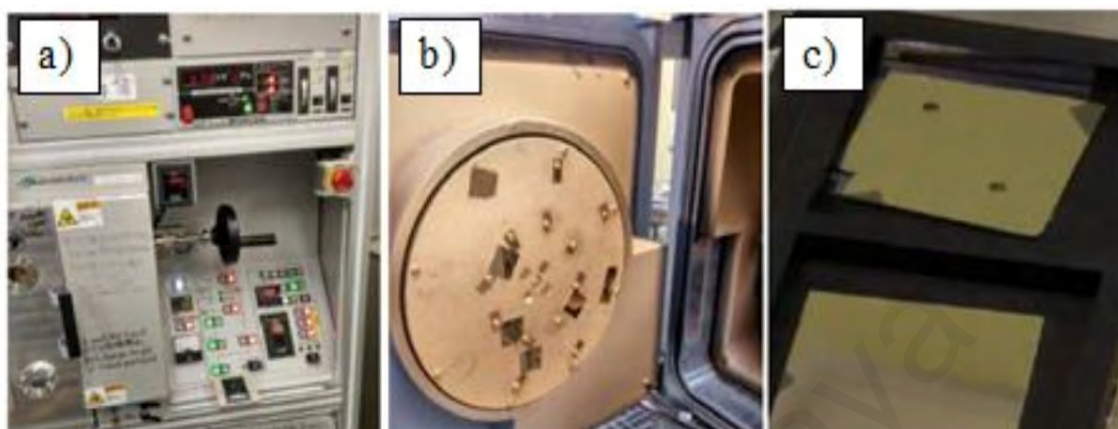


Figure 7.11. a) SHIBAURA sputter electrode deposition machine b) Si wafer mounted at sputter machine target c) Pt deposited on Si wafer

Table 7.5. Electrodeposition recipe

Target	Temperature	Power	Pressure	Stage rotation	Deposition rate
Pt	Room	300 W	0.5 Pa	20 rpm	35nm/min
Ti	Room	300 W	0.5 Pa	20rpm	13nm/min

(g) *Glass substrate patterning*

Glass was patterned using sand blasting technology. The process flow for glass patterning is as shown in Figure 7.12. The glass was laminated with thick negative dry film resist MS7050 as photo mask. Then to create cavity pattern on the dry film resist, the dry film was exposed to UV light and developed in calcium carbonate solution. 1 x 1 cm² cavity then etched by sand blasting machine as shown in Figure 7.13(a).

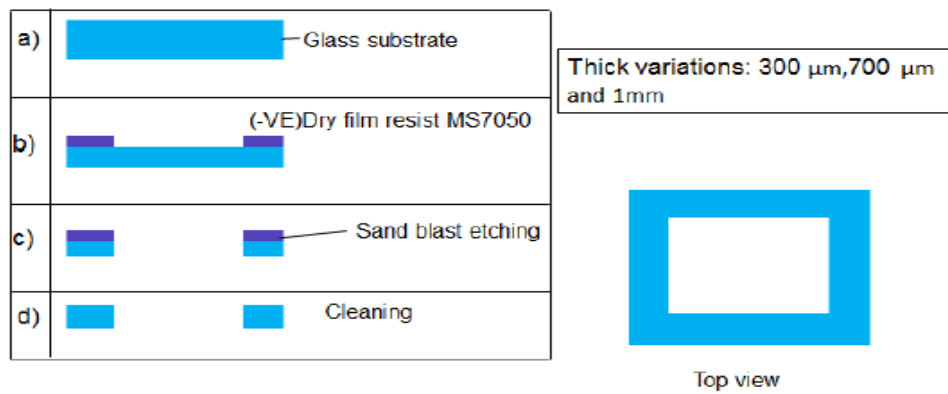


Figure 7.12. Glass substrate patterning process

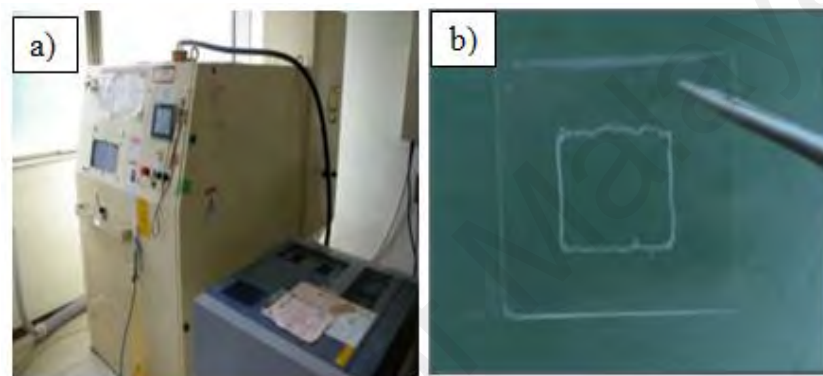


Figure 7.13. a) SHINTO Sand blast machine b) Glass with hole patterned after sand blasting process

(h) *Wafer bonding*

The upper and lower electrode was assembled using patterned SU-8 as shown in Figure 7.14. The filling process was done by injecting the electrolyte into the device through inlet and sealed using epoxy resin in the vacuum condition using glove box to avoid micro bubble inside the TEC devices. The finish prepared TEC device as shown in Figure 7.15.

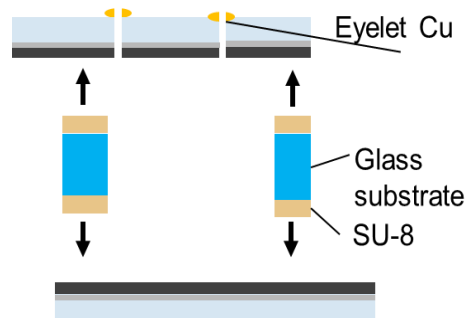


Figure 7.14. Wafer bonding of Si-Pt deposited with patterned glass substrate using SU-8 polymer



Figure 7.15. Finished single TEC device with cross section area $2 \times 2 \text{ cm}^2$ and 0.3 mm electrode separation

7.2.4 TEC performance evaluation

TEC devices performance had been measured using copper block heater and water cooler with compressor at temperature hot= $80 \text{ }^\circ\text{C}$ and temperature cold= $25 \text{ }^\circ\text{C}$. The temperature at the bottom and upper electrode were confirmed using thermocouple type K.

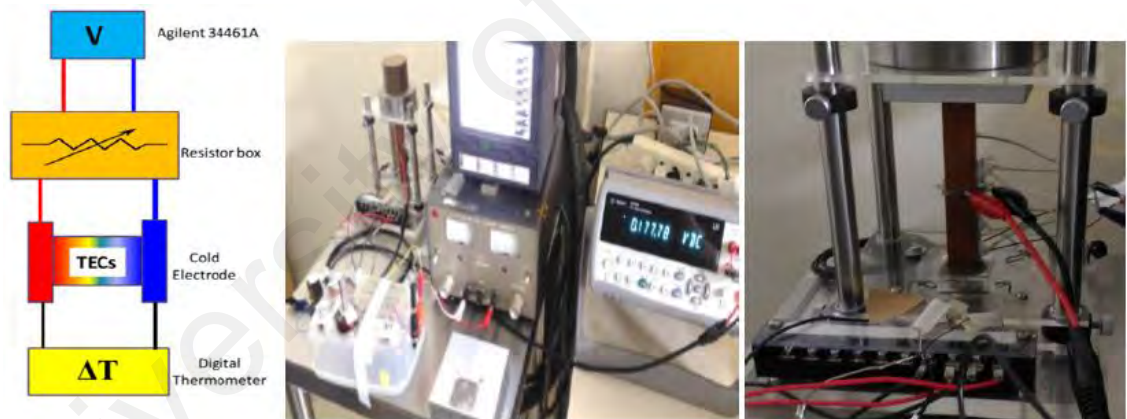


Figure 7.16 Seebeck and power measurement setup of TEC device

7.2.5 P-N single junction TEC device design and fabrication

Using the same process explained in previous section, single P-N junction of micro TEC using same area $2 \times 2 \text{ cm}^2$ also was fabricated using schematic shown in Figure 7.17.

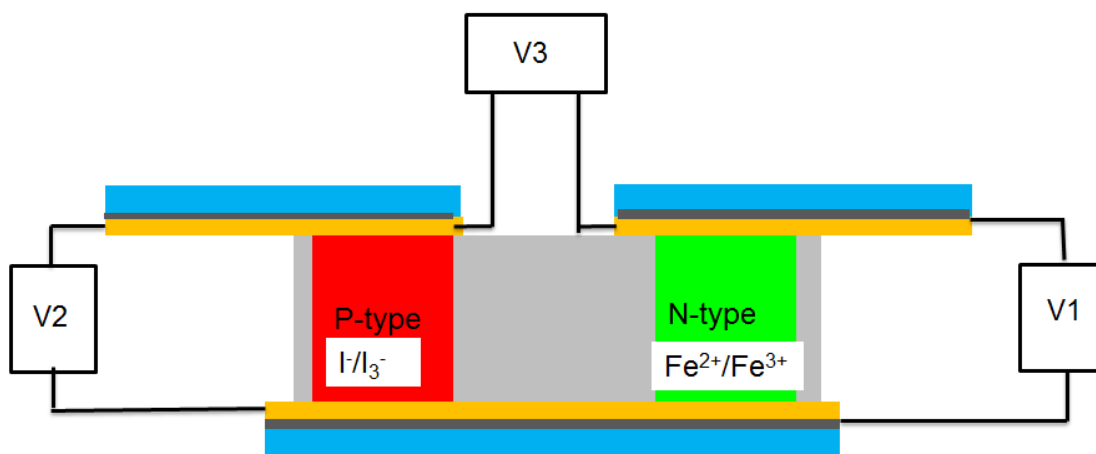


Figure 7.17. Single junction P-N TEC device

7.3 Results and discussion

7.3.1 Solution resistance

Figure 7.18 showed gel KI-KI₃ solution resistance with increasing temperature. The colour of the gel was changing from dark purple to transparent yellow with increasing temperature. The gel resistance was measured using HZ electrochemical analyzer at high frequency 100 KHz. The solution resistance was decreases with increase temperature with showing step profile at transition temperature 308-318 K. This resistance value will be compared with maximum power match load resistance to highlight the ohmic(high frequency) and non-ohmic(low frequency) limitation of the device.

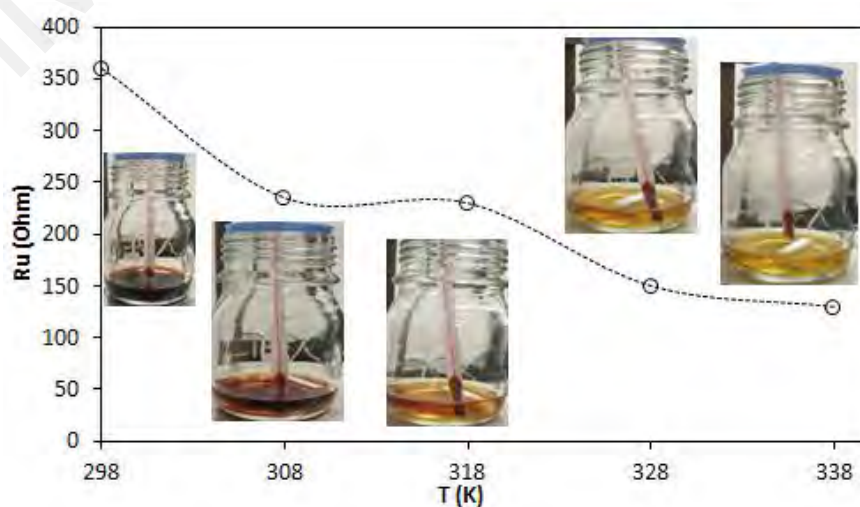


Figure 7.18. Solution resistance of iodide/triiodide gel electrolyte at dependent temperature

7.3.2 Cyclic voltammetry analysis

Figure 7.19 showed temperature dependent CV analysis of gel iodide/triiodide and $\text{Fe}^{2+/3+}$. The CV show good reversibility and redox potential of the gel electrolyte thus expected can be used for TEC energy harvesting.

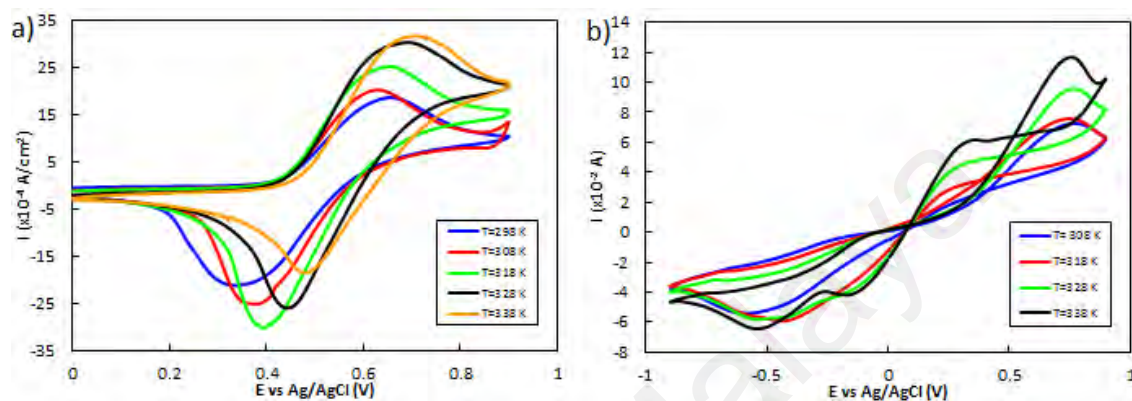


Figure 7.19. Cyclic voltammetry analysis of a) iodide/triiodide b) $\text{Fe}^{2+/3+}$ at various temperatures

7.3.2.1 Numerical study for Seebeck sign prediction based on Cyclic voltammetry experimental analysis

The P-type and N-type gel electrolytes material prepared had been shown through half cell potential and Seebeck extraction from cyclic voltammetry analysis as shown in Figure 7.22 and Figure 7.23 respectively. The iodide/triiodide had been shown having positive sign of Seebeck coefficient while the $\text{Fe}^{2+/3+}$ had been shown having opposite negative sign. The relation between the diffusion activity ratio as shown in Figure 7.21 and electrode formal potential as shown in Figure 7.20 respectively for both P-type and N-type material elucidated the sign of the Seebeck of the TEC material prepared.

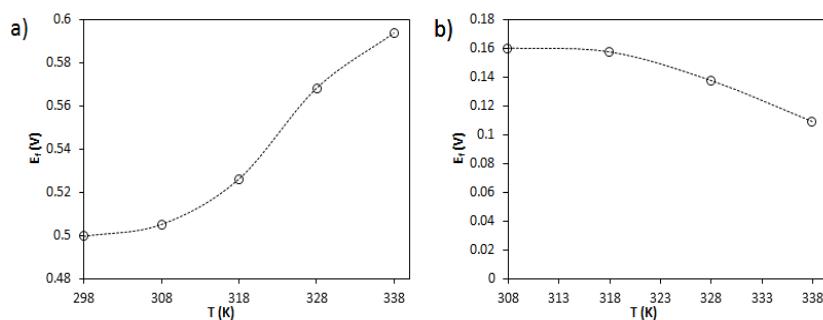


Figure 7.20. Electrode formal extraction from CV analysis of a) iodide/triiodide b) $\text{Fe}^{2+/3+}$ at various temperatures

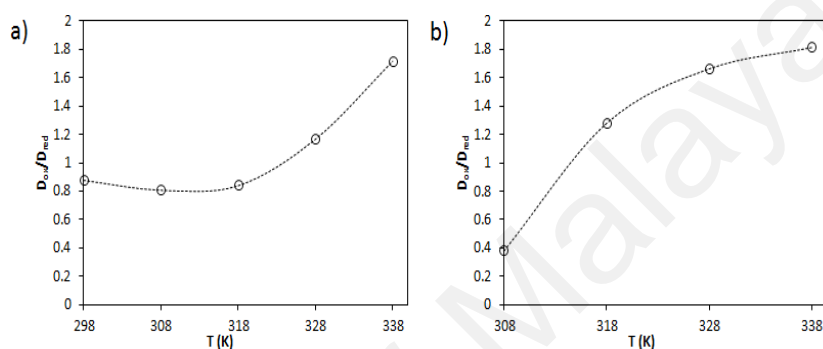


Figure 7.21. Diffusion ratio extraction from CV analysis of a) iodide/triiodide b) $\text{Fe}^{2+/3+}$ at various temperatures

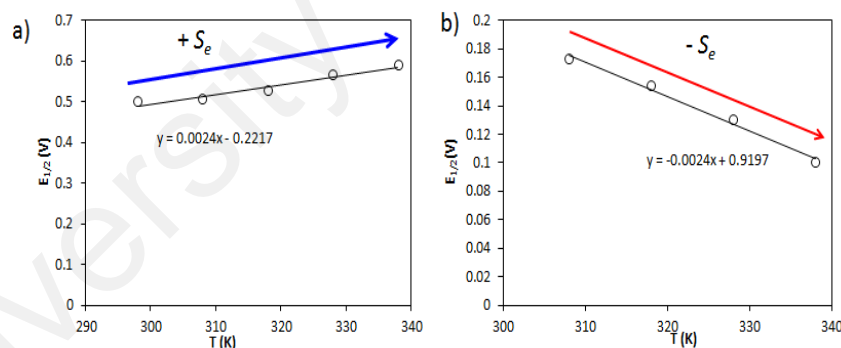


Figure 7.22. Half-cell potential extraction from CV analysis of a) iodide/triiodide b) $\text{Fe}^{2+/3+}$ at various temperatures

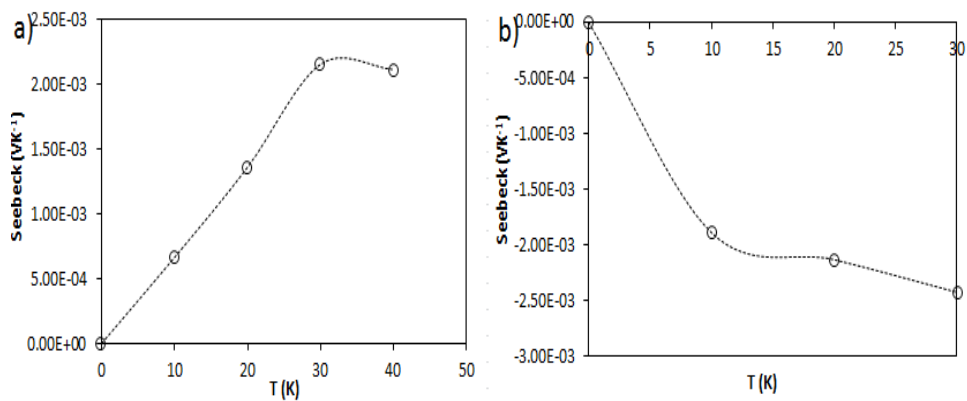


Figure 7.23. Seebeck extraction from CV analysis of a) iodide/triodide b) Fe^{2+/3+} at various temperatures differences

7.3.3 TEC performance

The Seebeck measured of isothermal TEC device with electrode separation 0.3 mm had been found +0.5 mVK⁻¹ for iodide/triodide and -0.16 mVK⁻¹ for Fe^{2+/3+} which expected with Seebeck extract from CV (refer to Figure 7.23) for iodide but slightly lower for Fe^{2+/3+} (+0.5 mVK⁻¹ for iodide/triodide and -0.5 mVK⁻¹ for Fe^{2+/3+}) at low temperature different (5 Kelvin) that can be maintain by the TEC device.

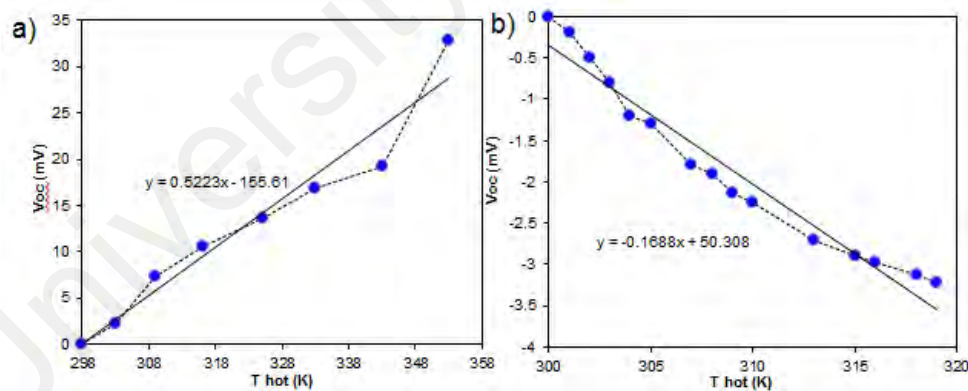


Figure 7.24. Seebeck evaluation of single TEC devices of a) iodide/triodide b) Fe^{2+/3+}

Then, several variations of electrode condition and separation had been fabricated as shown in Table 7.6 and Figure 7.25 below to investigate electrode pair, electrode separation, electrolyte molarity and gelation agent percentage effect to the Seebeck and power generation. The match load resistance at maximum power founded to be large

different in term of magnitude with the solution resistance measured at high frequency thus highlight non-ohmic limitation for the TEC device.

Table 7.6. I/I_3^- Seebeck generation with electrode separation 0.2 mm with different molarity and different PVA weight percentage

Condition	Molarity (M)	PVA percentage	S_e (mVK ⁻¹)
Conventional planar Pt-Pt	0.25	3% Wt	0.625
Conventional planar Pt-Pt	0.75	5% Wt	0.1875
Cold porous (Si deposited Ti/Pt)	0.75	5% Wt	0.325
Hot porous (Si deposited Ti/Pt)	0.75	5% Wt	0.125
Hot-Cold porous (Si deposited Ti/Pt)	0.75	5% Wt	0.2581
Au-Au	0.75	5% Wt	0.158714
Au-Pt	0.75	5% Wt	0.2581

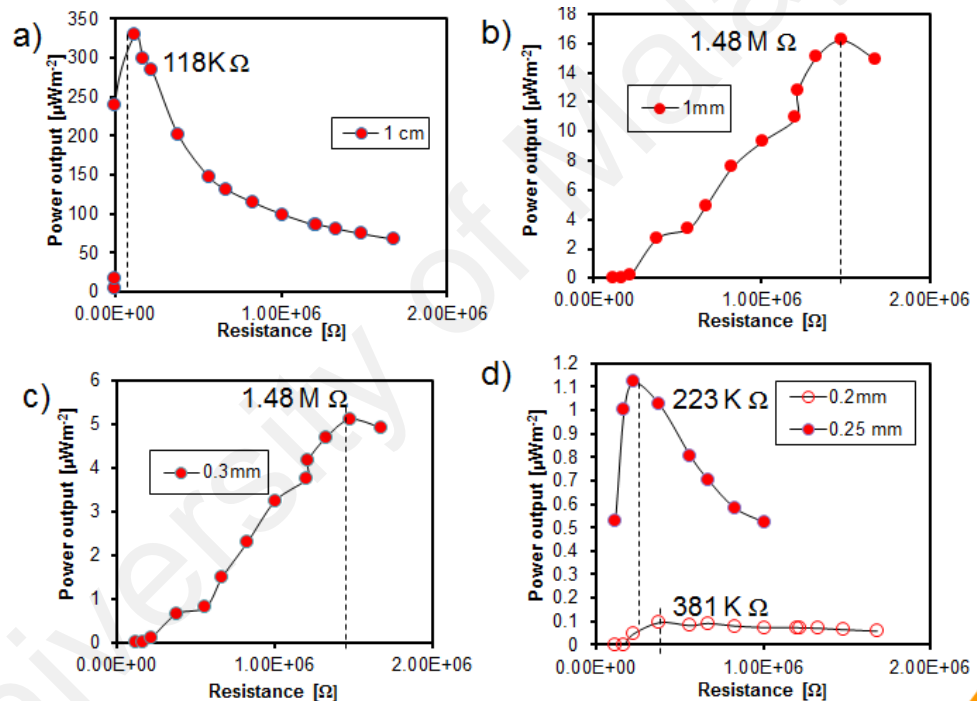


Figure 7.25. Power density evaluations of single TEC devices with various electrode separations a) 1 cm b) 1mm c) 0.3 mm and d) 0.2&0.25 mm

Single P-N junction of TEC device then fabricated with electrode separation 0.3 mm as shown in Figure 7.26 and the Seebeck had been found add up as series with 50% power enhancement (refer to Figure 7.27) compared to single P-type and single N-type devices thus proving that increase the number cell inside the TEC device can enhance the power density. However, the heats transfer mechanism when increases the cell density also

needs to be investigated in the future to find minimum size and optimum number cell density.

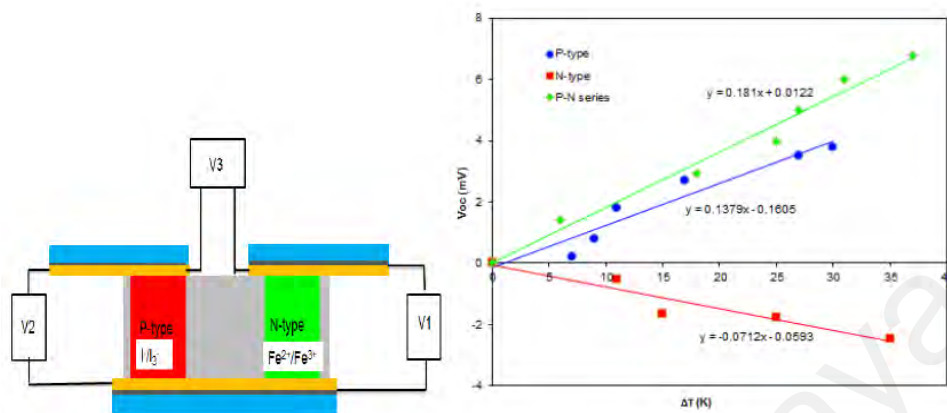


Figure 7.26. Single junction P-N TEC device and Seebeck evaluation

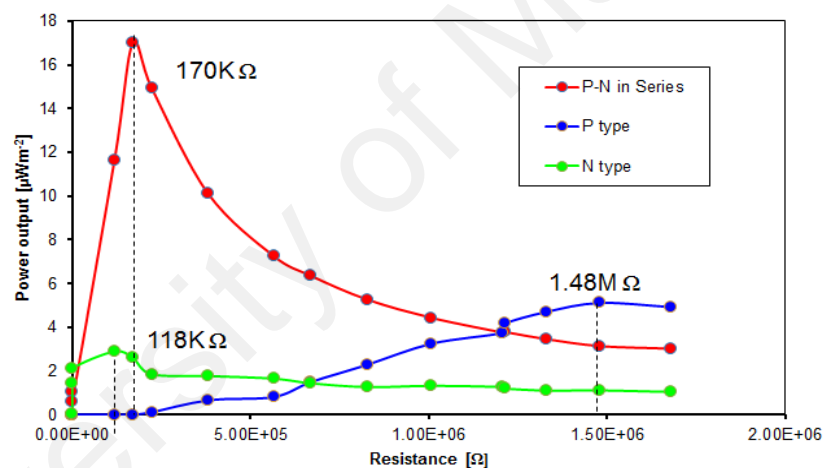


Figure 7.27. Power density evaluation

7.4 Conclusion

From this chapter, internal resistance come from non-ohmic and ohmic had been found as critical factor limit the TEC device performance. The best power output density in this study of single microTEC with low temperature different (5 K) was $18 \mu\text{Wm}^{-2}$. From this chapter, the fabrication process investigated was proven that high density of TEC cells can be done using micro fabrication technology for mass production. Thus, the high integrated micro TEC device was proposed in the future work section.

7.5 Future work

As closing to this chapter, the basic concept of high integrated microTEC device fabrication and design is proposed as shown in Figure 7.28 where all the parameter involves using the material properties in this study briefly described as below. The voltage generated estimated by coupling 2400 cell for 1x1 cm² active cross section area is 8 V at 5K temperature difference.

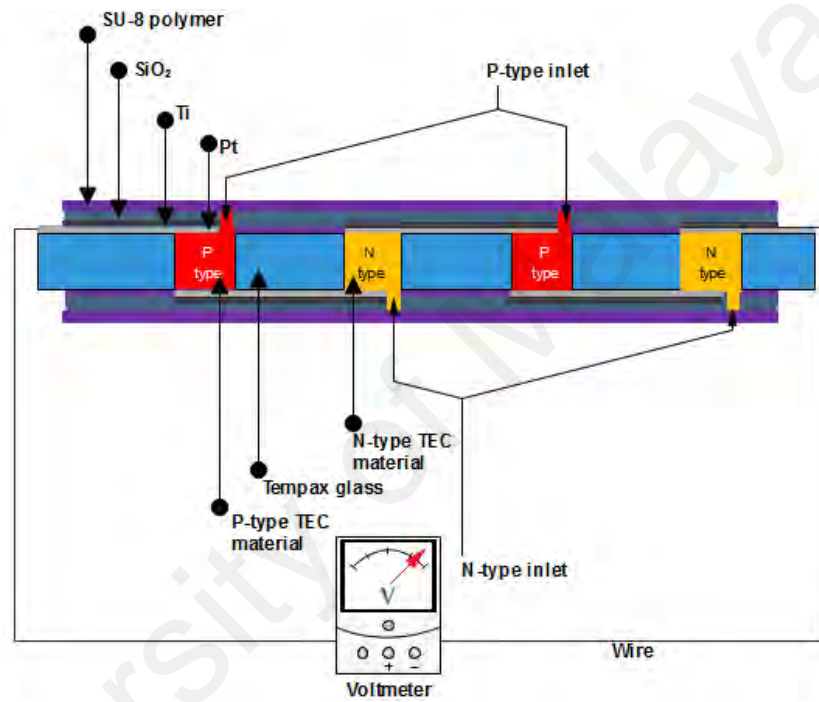


Figure 7.28. High density integrated cell microTEC device design

Cell diameter = 100 μ m; Number of cells = 2400; Cross section area = 1x1 cm²; Electrode separation = 300 μ m; $S_{e\ P\text{-type}} = +0.34\ \text{mVK}^{-1}$; $S_{e\ N\text{-type}} = -1\ \text{mVK}^{-1}$; $\Delta T = 5\ \text{K}$

$$\text{Total } S_e = N(S_{e\ P\text{-type}} - S_{e\ N\text{-type}}) = 1.608\ \text{VK}^{-1}$$

$$V_{\text{TEC}} = (\text{Total } S_e)(\Delta T) = 8\ \text{V}$$

where N is number of P-N junction, $S_{e\ P\text{-type}}$ is Seebeck coefficient for P-type, $S_{e\ N\text{-type}}$ is Seebeck coefficient for N-type, V_{TEC} is open circuit voltage generated and ΔT is temperature different.

Method of electrolyte filling is as shown in Figure 7.29 where the electrolyte is filled using capillary effect and vacuum pressure for both P-type and N-type filling.

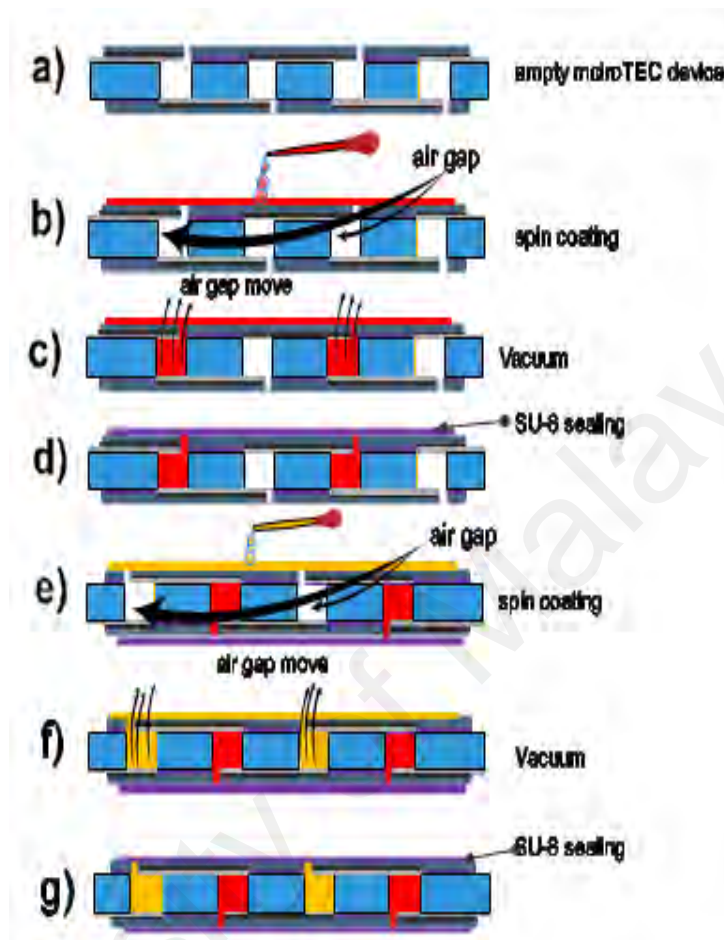


Figure 7.29. Electrolyte filling and sealing methodology of microTEC device

All mask design for the microTEC fabrication process are as shown as Figure 7.30- Figure 7.32.

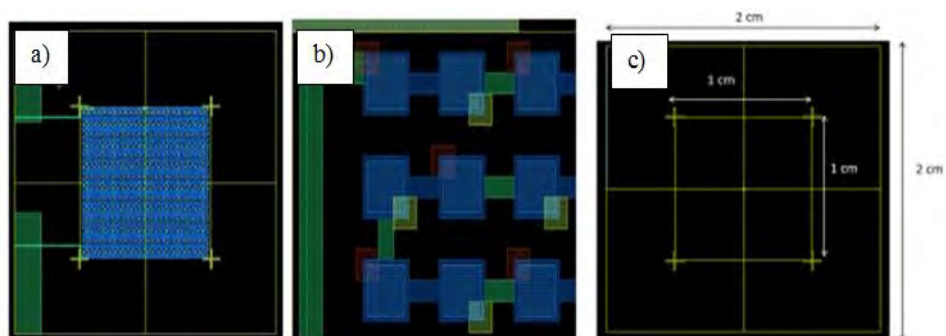


Figure 7.30. Mask design a) all layer overlap b) zoom and c) active area

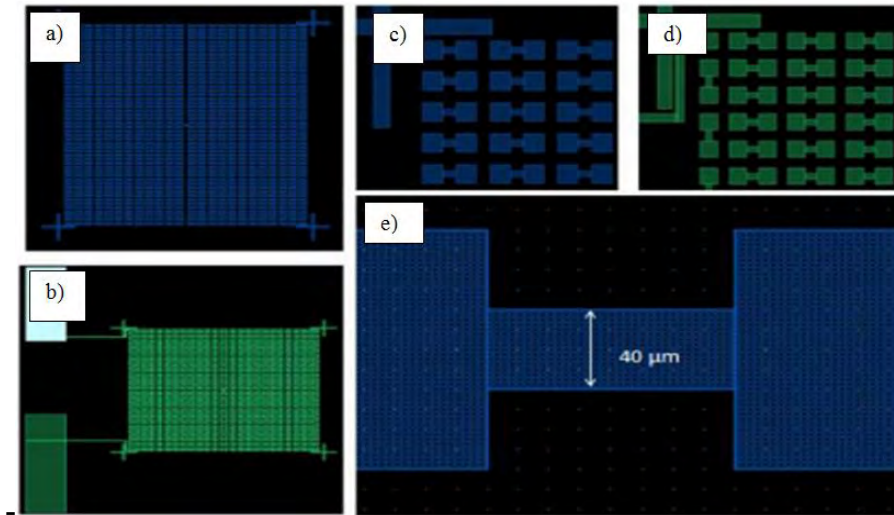


Figure 7.32. Electrode mask patterning design a) upper electrode b) bottom electrode c) zoom upper electrode d) zoom bottom electrode and e) connector between electrodes

The inlet etching process is as shown in Figure 7.33 using OFPR-200cp as photoresist mask.

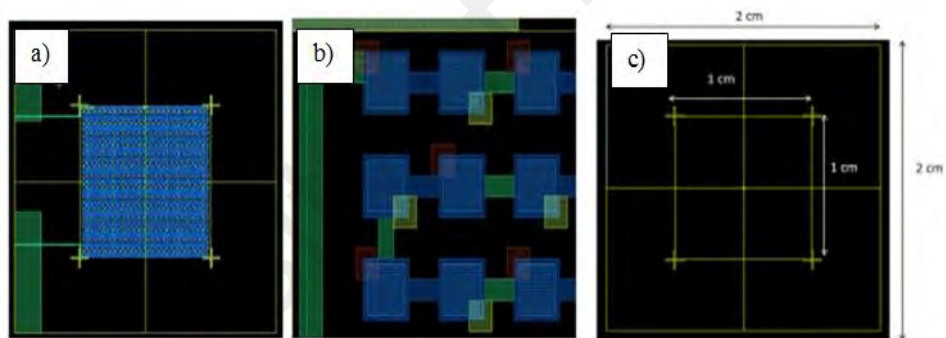


Figure 7.30. Mask design a) all layer overlap b) zoom and c) active area

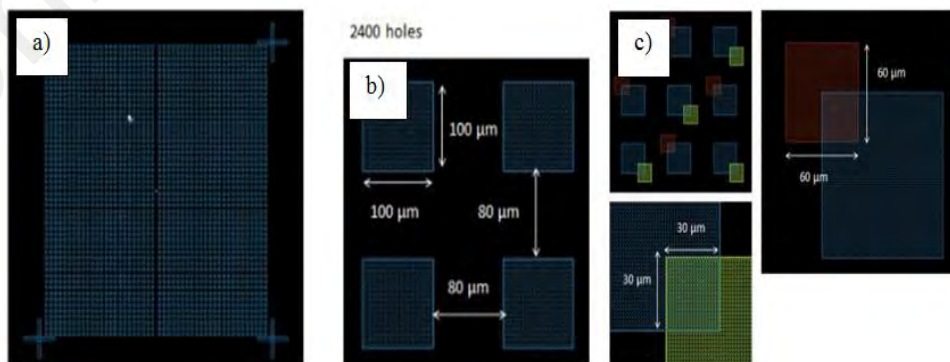


Figure 7.31. Mask design a) intermediate layer with holes b) holes size and separation and c) inlet overlap with cell holes

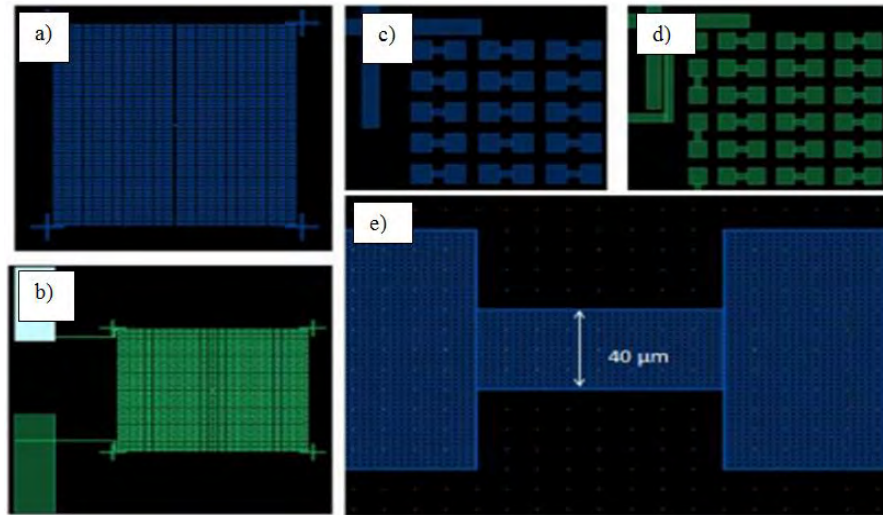


Figure 7.32. Electrode mask patterning design a) upper electrode b) bottom electrode c) zoom upper electrode d) zoom bottom electrode and e) connector between electrodes

The inlet etching process is as shown in Figure 7.33 using OFPR-200cp as photoresist mask.

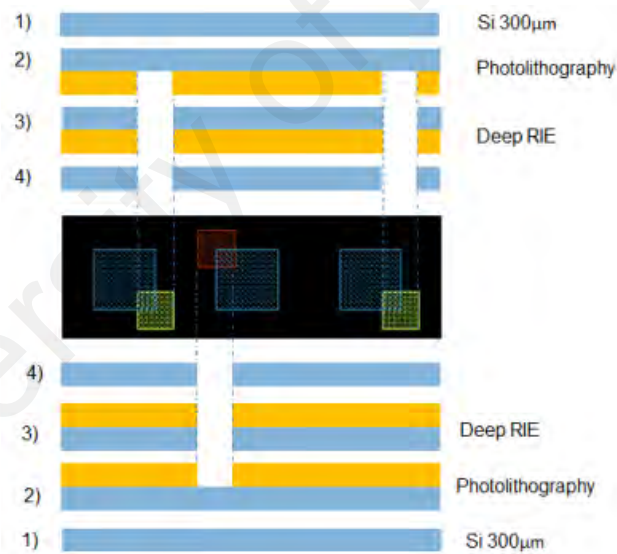


Figure 7.33. P-type and N-type inlet etching process

Figure 7.34 showed photoresist layer on Si substrate after photolithography process before etching. The finished substrate with inlet after deep RIE process under microscope is as shown in Figure 7.35.

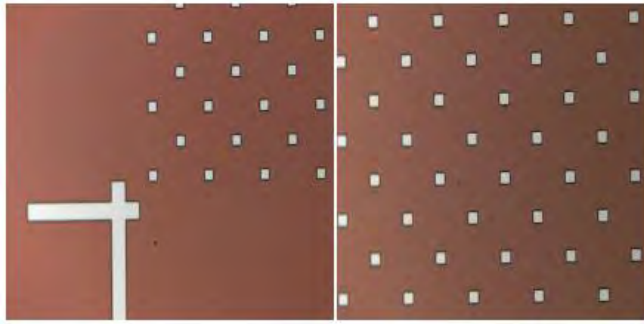


Figure 7.34. Photoresist layer on Si substrate after photolithography process

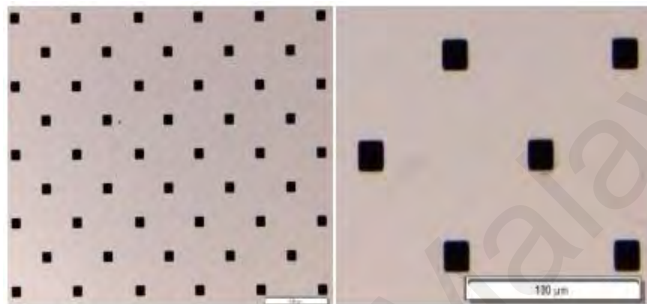


Figure 7.35. Inlet etching of Si wafer after deep RIE process

The electrode patterning process is as shown in Figure 7.36 which using focus ion beam milling to etch Ti-Pt layer using SU-8 as photoresist layer that aligned to overlap with inlet as shown in Figure 7.38.

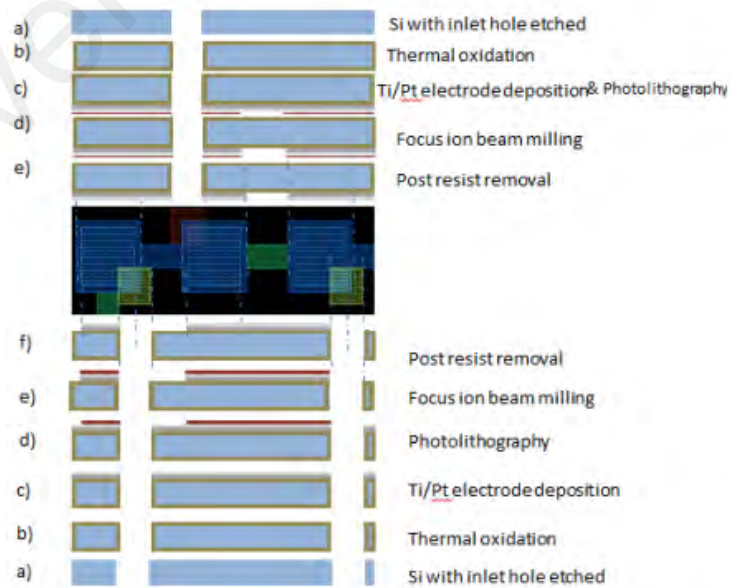


Figure 7.36. Electrode patterning process

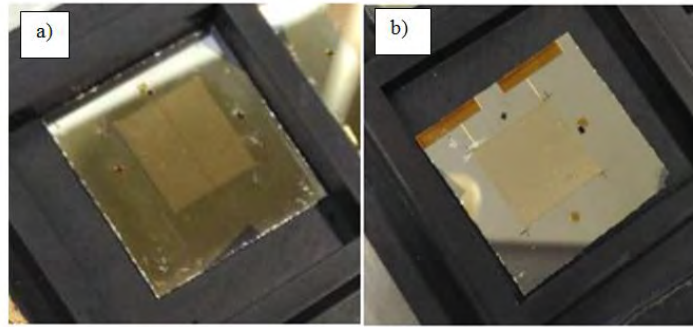


Figure 7.37. Photo resist layer patterning overlap with inlet on Si-Ti-Pt substrate after photolithography and alignment process a) upper electrode and b) lower electrode

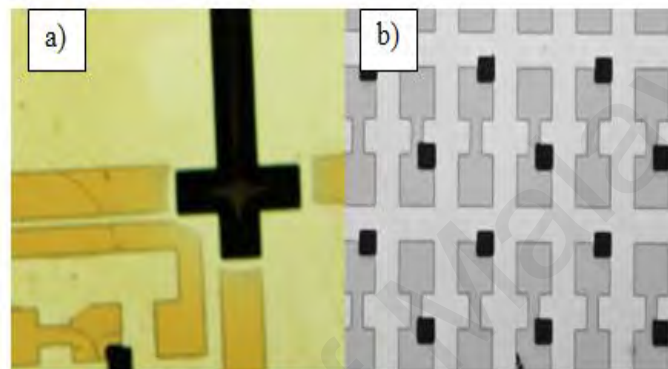


Figure 7.38. a) Photo resist layer patterning overlap with inlet after aligning b) inlet overlap with electrode pattern after photolithography and alignment process under microscope

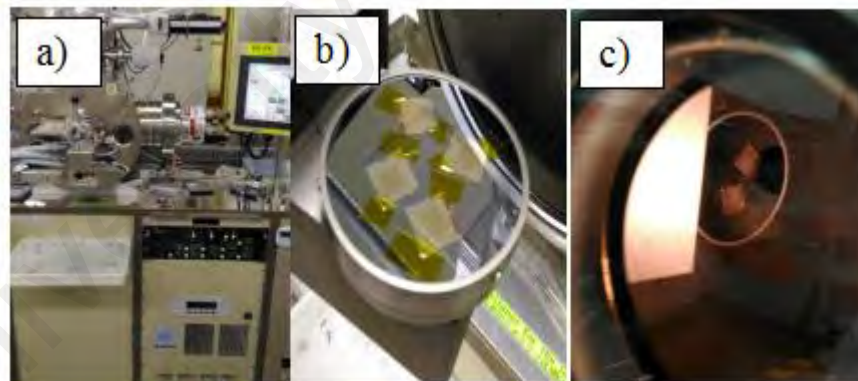


Figure 7.39. a) Focus ion beam machine b) Si-Ti-Pt substrate attached on FIB target c) ion beam milling process

The finished substrate after ion beam milling process (Figure 7.39) is as shown in Figure 7.40. The upper and electrode patterning with inlet successfully fabricated as shown in Figure 7.40.

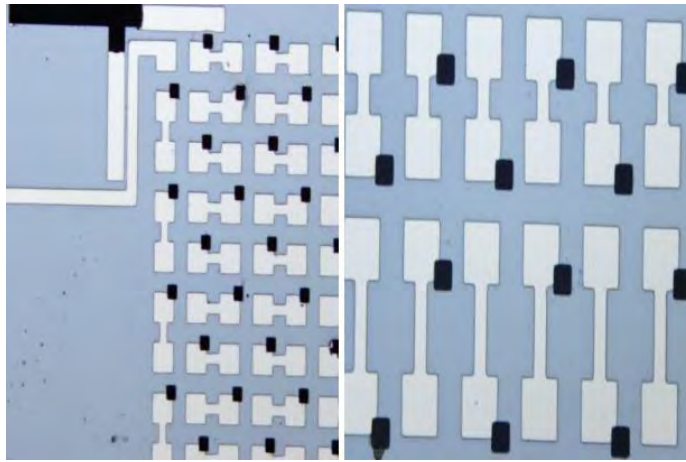


Figure 7.40. Electrode pattern under microscope after Ti-Pt etching using ion beam milling and after post residue removal process

University of Malaya

CHAPTER 8: CONCLUSION

This study proves that, the development of SCO material for TEC low grade heat waste energy harvesting is significance. The following explanation were key finding of the thesis.

From all investigation of the SCO octahedral for TEC energy harvesting presented in this dissertation, this study conclude that the molecular strategy for the best octahedral SCO condition in order to enhance SCO redox TEC performance is depends on Jahn-Teller distortion theorem. This study inferred that the best element to create high stability of both reduction state and oxidation state was using Fe as metal centre. This is due to only Fe element can have stable electronic configuration on both HS and LS state compared to other element Co and Mn. Mn and Co can have stable spin state but only for one redox state whether oxidation state only or reduction state only (if the complex having SCO effect). Based on Jahn teller distortion, the complex will suffer strong and weak distortion if electron in e_g orbitals and T_{2g} respectively unevenly occupied. The SCO or reverse SCO effect also important to create additional large entropy different due to the spin state transition in order to enhance difference reaction entropy at both cold and hot electrode through different of molecular radius which agreed with reaction entropy govern by Born's model. The stability is important to have fast electron transfer relaxation. The Fe^{2+} complex should be designed to be normal SCO (low spin to high spin) thus when LS Fe^{2+} oxidise become stable of Fe^{3+} high spin state. While for Fe^{3+} complex should be design reverse SCO thus when HS Fe^{3+} reduce become stable low spin Fe^{2+} . As shown in Figure 8.1, both LS Fe^{2+} and HS Fe^{3+} is not suffered from Jahn-Teller distortion expected due to orbitals evenly occupied for both T_g and T_{2g} orbital.

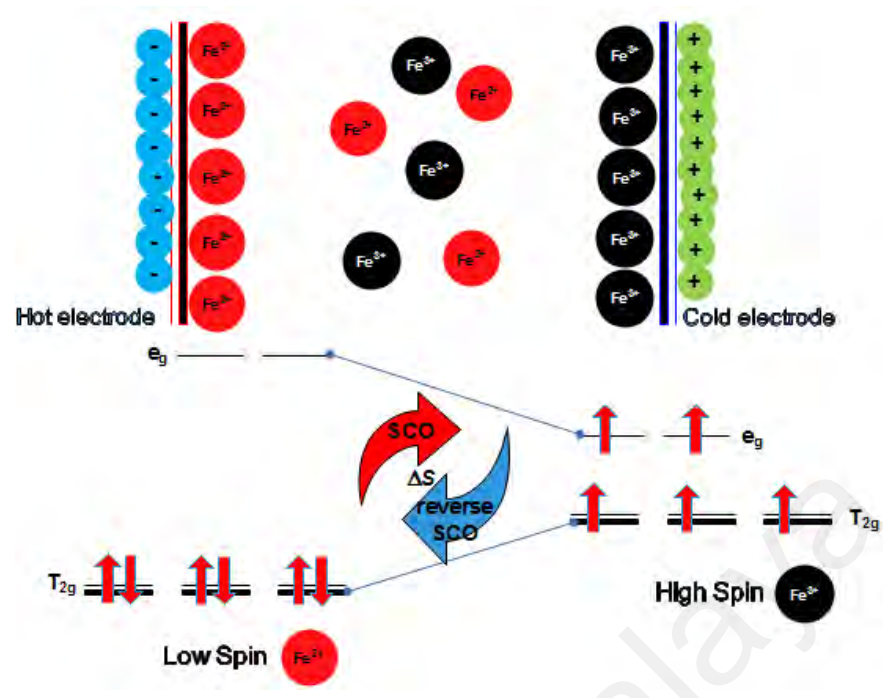


Figure 8.1. Ideal SCO model for TEC energy harvesting

From TEC device study, internal resistance come from non-ohmic and ohmic had been found as critical factor limit the TEC device performance due to different match load resistance (K to M ohm) at maximum power with solution ohmic resistance (150-350 ohm) measured at 100KHz. The best power output density in this study of single microTEC having electrode separation 1 mm (using KI-KI₃ PVA gel electrolyte with citric acid as supporting electrolyte) with low temperature different (5 K) was 18 μWm^{-2} . The fabrication methodology showed in this study highlight the large potential of fabricating high number of cell density at micro level in order to enhance the TEC power density proven by enhancement of power output of single P-N TEC junction compared to single cell TEC device.

REFERENCES

- Abdullah, N., Noor, N. L. M., Nordin, A. R., Halcrow, M. A., MacFarlane, D. R., Lazar, M. A., . . . Heinrich, B. (2015). Spin-crossover, mesomorphic and thermoelectrical properties of cobalt(II) complexes with alkylated N-3-Schiff bases. *Journal of Materials Chemistry C*, 3(11), 2491-2499. doi:10.1039/c4tc02923b
- Abraham, T. J., MacFarlane, D. R., Baughman, R. H., Jin, L. Y., Li, N., & Pringle, J. M. (2013). Towards ionic liquid-based thermoelectrochemical cells for the harvesting of thermal energy. *Electrochimica Acta*, 113, 87-93. doi:10.1016/j.electacta.2013.08.087
- Abraham, T. J., MacFarlane, D. R., & Pringle, J. M. (2011). Seebeck coefficients in ionic liquids -prospects for thermo-electrochemical cells. *Chemical Communications*, 47(22), 6260-6262. doi:10.1039/c1cc11501d
- Aldous, L., Black, J. J., Elias, M. C., Gelinas, B., & Rochefort, D. (2017). Enhancing thermoelectrochemical properties by tethering ferrocene to the anion or cation of ionic liquids: altered thermodynamics and solubility. *Physical Chemistry Chemical Physics*, 19(35), 24255-24263. doi:10.1039/c7cp04322h
- Anari, E. H. B., Romano, M., Teh, W. X., Black, J. J., Jiang, E., Chen, J., . . . Aldous, L. (2016). Substituted ferrocenes and iodine as synergistic thermoelectrochemical heat harvesting redox couples in ionic liquids. *Chemical Communications*, 52(4), 745-748. doi:10.1039/c5cc05889a
- Chani, M. T. S., Karimov, K. S., Khan, S. B., & Asiri, A. M. (2015). Fabrication and Investigation of Flexible Photo-Thermo Electrochemical Cells based on Cu/orange dye aqueous solution/Cu. *International Journal of Electrochemical Science*, 10(7), 5694-5701.
- Commission, E. (2015). *National Energy Balance* Retrieved from
- Delley, B. (2006). Ground-state enthalpies: evaluation of electronic structure approaches with emphasis on the density functional method. *The Journal of Physical Chemistry A*, 110(50), 13632-13639.
- Dupont, M. F., MacFarlane, D. R., & Pringle, J. M. (2017). Thermo-electrochemical cells for waste heat harvesting - progress and perspectives. *Chemical Communications*, 53(47), 6288-6302. doi:10.1039/c7cc02160g
- Gunawan, A., Li, H. C., Lin, C. H., Buttry, D. A., Mujica, V., Taylor, R. A., . . . Phelan, P. E. (2014). The amplifying effect of natural convection on power generation of thermogalvanic cells. *International Journal of Heat and Mass Transfer*, 78, 423-434. doi:10.1016/j.ijheatmasstransfer.2014.07.007
- Gunawan, A., Lin, C. H., Buttry, D. A., Mujica, V., Taylor, R. A., Prasher, R. S., & Phelan, P. E. (2013). Liquid Thermoelectrics: Review of Recent And Limited New Data of Thermogalvanic Cell Experiments. *Nanoscale and Microscale Thermophysical Engineering*, 17(4), 304-323. doi:10.1080/15567265.2013.776149

- Gutlich, P., Hauser, A., & Spiering, H. (1994). Thermal and Optical Switching of Iron(II) Complexes. *Angewandte Chemie-International Edition in English*, 33(20), 2024-2054. doi:DOI 10.1002/anie.199420241
- Halcrow, M. A. (2014). Spin-crossover Compounds with Wide Thermal Hysteresis. *Chemistry Letters*, 43(8), 1178-1188. doi:10.1246/cl.140464
- Hasan, S. W., Said, S. M., Sabri, M. F. M., Abu Bakar, A. S., Hashim, N. A., Hasnan, M. M. I. M., . . . MacFarlane, D. R. (2016). High Thermal Gradient in Thermo-electrochemical Cells by Insertion of a Poly(Vinylidene Fluoride) Membrane. *Scientific Reports*, 6. doi:Artn 2932810.1038/Srep29328
- Hasnan, M. M. I. M., Abdullah, N., Said, S. M., Salleh, M. F. M., Hussin, S. A. M., & Shah, N. M. (2018). Thermo-electrochemical generation capabilities of octahedral spin crossover complexes of Mn(II), Fe(II) and Co(II) with N-donor ligands and benzoate counter ion. *Electrochimica Acta*, 261, 330-339. doi:10.1016/j.electacta.2017.12.145
- Hasnan, M. M. I. M., Said, S. M., Sabri, M. F. M., Hussin, S. A. M., Abdullah, N., Ibrahim, N. M. J. N., . . . Shah, N. M. (2019). Optimised thermally driven molecular stability of an SCO metal complex for TEC Seebeck generation enhancement. *Rsc Advances*, 9(19), 10626-10634.
- Hayami, S., Gu, Z. Z., Yoshiki, H., Fujishima, A., & Sato, O. (2001). Iron(III) spin-crossover compounds with a wide apparent thermal hysteresis around room temperature. *Journal of the American Chemical Society*, 123(47), 11644-11650. doi:Doi 10.1021/Ja0017920
- Hayami, S., Komatsu, Y., Shimizu, T., Kamihata, H., & Lee, Y. N. (2011). Spin-crossover in cobalt(II) compounds containing terpyridine and its derivatives. *Coordination Chemistry Reviews*, 255(17-18), 1981-1990. doi:10.1016/j.ccr.2011.05.016
- Hayami, S., Shigeyoshi, Y., Akita, M., Inoue, K., Kato, K., Osaka, K., . . . Maeda, Y. (2005). Reverse spin transition triggered by a structural phase transition. *Angewandte Chemie-International Edition*, 44(31), 4899-4903. doi:10.1002/anie.200500316
- Hofbauer, S., Bellei, M., Sundermann, A., Pirker, K. F., Hagmuller, A., Mlynek, G., . . . Obinger, C. (2012). Redox Thermodynamics of High-Spin and Low-Spin Forms of Chlorite Dismutases with Diverse Subunit and Oligomeric Structures. *Biochemistry*, 51(47), 9501-9512. doi:10.1021/bi3013033
- Hohenberg, P., & Kohn, W. (1964). Inhomogeneous electron gas. *Physical review*, 136(3B), B864.
- Hu, R. C., Cola, B. A., Haram, N., Barisci, J. N., Lee, S., Stoughton, S., . . . Baughman, R. H. (2010). Harvesting Waste Thermal Energy Using Carbon-Nanotube-Based Thermo-Electrochemical Cell. *Nano Letters*, 10(3), 838-846. doi:10.1021/nl903267n

- Hupp, J. T., & Weaver, M. J. (1984). Solvent, Ligand, and Ionic Charge Effects on Reaction Entropies for Simple Transition-Metal Redox Couples. *Inorganic Chemistry*, 23(22), 3639-3644. doi:Doi 10.1021/Ic00190a042
- Hussin, S. A. B. M. (2016). *Magnetic, Metallomesogen and Thermoelectric Studies of Cu(II), Ni(II), Co(II), Fe(II) And Mn(II) Complexes with Benzoate, Cyclam and 4-Alkyloxyppyridines as Ligands*. (Master Science), University of Malaya, Kuala Lumpur.
- Ikeshoji, T. (1987). Thermoelectric Conversion by Thin-Layer Thermogalvanic Cells with Soluble Redox Couples. *Bulletin of the Chemical Society of Japan*, 60(4), 1505-1514. doi:Doi 10.1246/Bcsj.60.1505
- Inagaki, M., Itoh, E., & Tanaka, A. (1990). Durable Performance of a Thermocell. *Synthetic Metals*, 35(3), 383-385. doi:Doi 10.1016/0379-6779(90)90223-8
- Jamaludin, N., Mohammed, N. I., Khamidi, M. F., & Wahab, S. N. A. (2015). Thermal Comfort of Residential Building in Malaysia at Different Micro-Climates. *Asian Conference on Environment-Behaviour Studies (Ace-Bs 2014 Seoul)*, 170, 613-623. doi:10.1016/j.sbspro.2015.01.063
- Janes, R., & Moore, E. A. (2004). *Metal-ligand bonding*: Royal society of chemistry.
- Jin, L. Y., Greene, G. W., MacFarlane, D. R., & Pringle, J. M. (2016). Redox-Active Quasi-Solid-State Electrolytes for Thermal Energy Harvesting. *Acs Energy Letters*, 1(4), 654-658. doi:10.1021/acsenergylett.6b00305
- Kang, T. J., Fang, S. L., Kozlov, M. E., Haines, C. S., Li, N., Kim, Y. H., . . . Baughman, R. H. (2012). Electrical Power From Nanotube and Graphene Electrochemical Thermal Energy Harvesters. *Advanced Functional Materials*, 22(3), 477-489. doi:10.1002/adfm.201101639
- Kazim, A. H., & Cola, B. A. (2016). Electrochemical Characterization of Carbon Nanotube and Poly (3,4-ethylenedioxythiophene)-Poly(styrenesulfonate) Composite Aqueous Electrolyte for Thermo-Electrochemical Cells. *Journal of the Electrochemical Society*, 163(8), F867-F871. doi:10.1149/2.0981608jes
- Keppner, H., Uhl, S., Laux, E., Jeandupeux, L., Tschanz, J., & Journot, T. (2015). Ionic Liquid-based Thermoelectric Generator: Links between Liquid Data and Generator Characteristics. *Materials Today-Proceedings*, 2(2), 680-689. doi:10.1016/j.matpr.2015.05.086
- Kissinger, P. T., & Heineman, W. R. (1983). Cyclic voltammetry. *Journal of Chemical Education*, 60(9), 702. doi:10.1021/ed060p702
- Koerver, R., MacFarlane, D. R., & Pringle, J. M. (2015). Evaluation of Electrochemical Methods for Determination of the Seebeck Coefficient of Redox Electrolytes. *Electrochimica Acta*, 184, 186-192. doi:10.1016/j.electacta.2015.10.070
- Kugel', K. I. i., & Khomskiĭ, D. (1982). The Jahn-Teller effect and magnetism: transition metal compounds. *Physics-Usppekhi*, 25(4), 231-256.

- Laux, E., Uhl, S., Journot, T., Brossard, J., Jeandupeux, L., & Keppner, H. (2016). Aspects of Protonic Ionic Liquid as Electrolyte in Thermoelectric Generators. *Journal of Electronic Materials*, 45(7), 3383-3389. doi:10.1007/s11664-016-4526-1
- Lin, C. H., Gunawan, A., Phelan, P. E., Buttry, D. A., Mujica, V., Taylor, R. A., & Prasher, R. (2013). Optimization of Cell Configuration for Maximizing Performance of a Cu/Cu²⁺ Aqueous Thermogalvanic Cell. *International Mechanical Engineering Congress and Exposition - 2012, Vol 6, Pts a and B*, 541-547.
- Migita, T., Tachikawa, N., Katayama, Y., & Miura, T. (2009). Thermoelectromotive Force of Some Redox Couples in an Amide-type Room-temperature Ionic Liquid. *Electrochemistry*, 77(8), 639-641. doi:DOI 10.5796/electrochemistry.77.639
- Murray, K. S., Oshio, H., & Real, J. A. (2013). Spin-Crossover Complexes. *European Journal of Inorganic Chemistry*(5-6), 577-580. doi:10.1002/ejic.201300062
- Nicholson, R. S. (1965). Theory and Application of Cyclic Voltammetry for Measurement of Electrode Reaction Kinetics. *Analytical Chemistry*, 37(11), pp 1351-1355. doi:10.1021/ac60230a016
- Nugent, J. M., Santhanam, K. S. V., Rubio, A., & Ajayan, P. M. (2001). Fast electron transfer kinetics on multiwalled carbon nanotube microbundle electrodes. *Nano Letters*, 1(2), 87-91. doi:10.1021/nl005521z
- Perdew, J. P., Burke, K., & Ernzerhof, M. (1996). Generalized gradient approximation made simple. *Physical Review Letters*, 77(18), 3865.
- Quickenden, T. I., & Mua, Y. (1995a). The Power Conversion Efficiencies of a Thermogalvanic Cell Operated in 3 Different Orientations. *Journal of the Electrochemical Society*, 142(11), 3652-3659. doi:Doi 10.1149/1.2048394
- Quickenden, T. I., & Mua, Y. (1995b). A Review of Power-Generation in Aqueous Thermogalvanic Cells. *Journal of the Electrochemical Society*, 142(11), 3985-3994. doi:Doi 10.1149/1.2048446
- Rotaru, A., Gural'skiy, I. A., Molnar, G., Salmon, L., Demont, P., & Bousseksou, A. (2012). Spin state dependence of electrical conductivity of spin crossover materials. *Chemical Communications*, 48(35), 4163-4165. doi:10.1039/c2cc30528c
- Salazar, P. F., Kumar, S., & Cola, B. A. (2014). Design and optimization of thermo-electrochemical cells. *Journal of Applied Electrochemistry*, 44(2), 325-336. doi:10.1007/s10800-013-0638-y
- Salazar, P. F., Stephens, S. T., Kazim, A. H., Pringle, J. M., & Cola, B. A. (2014). Enhanced thermo-electrochemical power using carbon nanotube additives in ionic liquid redox electrolytes. *Journal of Materials Chemistry A*, 2(48), 20676-20682. doi:10.1039/c4ta04749d

- Shindo, K., Arakawa, M., & Hirai, T. (2002). Influence of electrode materials on open-circuit voltage profiles with a temperature difference for a thermocell using a Br₂/Br⁻-redox reaction. *Journal of Power Sources*, 110(1), 46-51. doi:10.1016/S0378-7753(02)00216-1
- Shongwe, M. S., Al-Barhi, K. S., Mikuriya, M., Adams, H., Morris, M. J., Bill, E., & Molloy, K. C. (2014). Tuning a Single Ligand System to Stabilize Multiple Spin States of Manganese: A First Example of a Hydrazone-Based Manganese(III) Spin-Crossover Complex. *Chemistry-a European Journal*, 20(31), 9693-9701. doi:10.1002/chem.201402634
- Siddique, T. A., Balamurugan, S., Said, S. M., Sairi, N. A., & Normazlan, W. M. D. W. (2016). Synthesis and characterization of protic ionic liquids as thermoelectrochemical materials. *Rsc Advances*, 6(22), 18266-18278. doi:10.1039/c5ra24835c
- Sun, H. Y., Pu, J. H., & Tang, G. H. (2016). High-Performance Thermogalvanic Cell Based on Organic Nanofluids. *Acta Physico-Chimica Sinica*, 32(10), 2555-2562. doi:10.3866/Pku.Whxb201606281
- Tenaga, S. (2015). *Annual Report 2015*. Retrieved from Malaysia:
- Uhl, S., Laux, E., Journot, T., Jeandupeux, L., Charmet, J., & Keppner, H. (2014). Development of flexible micro-thermo-electrochemical generators based on ionic liquids. *Journal of Electronic Materials*, 43(10), 3758-3764.
- Uhl, S., Pellet, M., Tschanz, J., Laux, E., Journot, T., Jeandupeux, L., & Keppner, H. (2015). Fabrication of highly-integrated thermoelectric generators based on Ionic Liquids. *Materials Today-Proceedings*, 2(2), 669-674. doi:10.1016/j.matpr.2015.05.084
- Vasu, B., Gorla, R. S. R., & Murthy, P. V. S. N. (2017). Thermophoresis on boundary layer heat and mass transfer flow of Walters-B fluid past a radiate plate with heat sink/source. *Heat and Mass Transfer*, 53(5), 1553-1570. doi:10.1007/s00231-016-1917-z
- Vela, S., Verot, M., Fromager, E., & Robert, V. (2017). Electron transport through a spin crossover junction. Perspectives from a wavefunction-based approach. *Journal of Chemical Physics*, 146(6). doi:Artn 064112
10.1063/1.4975327
- Vining, C. B. (2009). An inconvenient truth about thermoelectrics. *Nature Materials*, 8(2), 83-85. doi:10.1038/nmat2361
- Wang, M., & Wong, C. F. (2006). Calculation of solvation free energy from quantum mechanical charge density and continuum dielectric theory. *The Journal of Physical Chemistry A*, 110(14), 4873-4879.
- Wu, J., Black, J. J., & Aldous, L. (2017). Thermoelectrochemistry using conventional and novel gelled electrolytes in heat-to-current thermocells. *Electrochimica Acta*, 225, 482-492. doi:10.1016/j.electacta.2016.12.152

- Yamada, T., Zou, X., Liang, Y., & Kimizuka, N. (2018). A supramolecular thermocell consisting of ferrocenecarboxylate and β -cyclodextrin that has a negative Seebeck coefficient. *Polymer Journal*, 1.
- Yamato, Y., Katayama, Y., & Miura, T. (2013). Effects of the Interaction between Ionic Liquids and Redox Couples on Their Reaction Entropies. *Journal of the Electrochemical Society*, 160(6), H309-H314. doi:10.1149/2.055306jes
- Zhang, L., Kim, T., Li, N., Kang, T. J., Chen, J., Pringle, J. M., . . . Baughman, R. H. (2017). High Power Density Electrochemical Thermocells for Inexpensively Harvesting Low-Grade Thermal Energy. *Advanced Materials*, 29(12). doi:10.1002/Adma.201605652
- Zhou, H., & Liu, P. (2018). High Seebeck Coefficient Electrochemical Thermocells for Efficient Waste Heat Recovery. *ACS Applied Energy Materials*, 1(4), 1424-1428.
- Zhou, H. Y., Yamada, T., & Kimizuka, N. (2016). Supramolecular Thermo-Electrochemical Cells: Enhanced Thermoelectric Performance by Host-Guest Complexation and Salt-Induced Crystallization. *Journal of the American Chemical Society*, 138(33), 10502-10507. doi:10.1021/jacs.6b04923
- Zhou, Y., Yang, C., Lam, Y. C., & Huang, X. Y. (2016). Thermophoresis of charged colloidal particles in aqueous media - Effect of particle size. *International Journal of Heat and Mass Transfer*, 101, 1283-1291. doi:10.1016/j.ijheatmasstransfer.2016.05.109

LIST OF PUBLICATIONS

1. Hasnan, M. M. I. M., Abdullah, N., Said, S. M., Salleh, M. F. M., Hussin, S. A. M., & Shah, N. M. (2018). Thermo-electrochemical generation capabilities of octahedral spin crossover complexes of Mn(II), Fe(II) and Co(II) with N-donor ligands and benzoate counter ion. *Electrochimica Acta*, 261, 330-339. doi: 10.1016/j.electacta.2017.12.145
2. Hasnan, M. M. I. M., Said, S. M., Mohd Sabri, M. F., Hussin, S. A. M., Abdullah, N., Nik Ibrahim, N. M. J., Miyazaki, Y., Salleh, M. F. M., & Shah, N. M. (2019). Optimise Thermally Driven Molecule Stability of SCO Metal Complex for TEC Seebeck Generation Enhancement. *RSC Advances*.
3. Hasnan, M. M. I. M., Said, S. M., Mohd Sabri, M. F., Hussin, S. A. M., Abdullah, N., Nik Ibrahim, N. M. J., Salleh, M. F. M., & Shah, N. M. (2019). Electrochemical Analysis of Spin Crossover Redox Electrolyte for Thermal-Electric Energy Harvesting. *Journal of Electroanalytical Chemistry*. (under review)
4. Van Toan, N., Hasnan, M. M. I. M., Udagawa, D., Inomata, N., Toda, M., Said, S. M., Ono, T. (2019). Thermoelectric power battery using Al_2O_3 nanochannels of 10 nm diameter for energy harvesting of low-grade waste heat. *Energy Conversion and Management*.